Towards a Universal Two-Qubit Gate with Self-Assembled InAs Quantum Dot Molecules

by

Colin M. E. Chow

A dissertation submitted in partial fulfillment
of the requirements for the degree of
Doctor of Philosophy
(Electrical Engineering)
in The University of Michigan
2015

Doctoral Committee:

Professor Duncan G. Steel, Chair
Assistant Professor Hui Deng
Professor Theodore B. Norris
Associate Professor Vanessa Sih

To
Jing Huang

ACKNOWLEDGEMENTS

My first thanks goes to my thesis advisor, Prof. Duncan Steel, without whom I would have missed the fascinating subject of quantum physics. I am grateful for the opportunities he has provided, and the unusual amount of confidence he has in me, a person with little background in physics. All these years, I have been benefited by his mentoring in both professional and personal matters.

I would like to thank Prof. Ted Norris, Prof. Hui Deng and Prof. Vanessa Sih for serving on my dissertation committee. The main idea and motivation for this work largely come from Prof. Luming Duan and Prof. Lu Sham. I would also like to thank Zhexuan Gong for the theoretical groundwork he had developed for this work. Dan Gammon and his team at the Naval Research Lab had not only provided the samples, but also shared valuable information and experience in the study of quantum dot molecules. Above all, Allan Bracker and Danny Kim had assisted in tasks ranging from fixing the samples to interpreting the data.

It was a privilege to be able to learn from highly motivated and talented group members, especially Bo Sun, John Schaibley and Alex Burgers. The instrumentation John and Alex pioneered and their continual assistance in the experimental methodology have been invaluable in my graduate career. I would also like to thank Cameron Nelson, Uttam Paudel and Lu Ma for their occasional help and the inspirational conversations we had together. In the past two years, I have been honored to be able to work alongside Aaron Ross. I cannot thank him enough for his dedication to the project. This work would not have been possible without the help from him.

Finally, I would like to take the opportunity to express my deepest gratitude to my wife, Jing Huang, for her emotional support and for bearing the distance over the last few years. It was through her kindness and understanding that I managed to focus on completing graduate school.

TABLE OF CONTENTS

CHAPTER

LIST OF FIGURES

Figure

LIST OF TABLES

Table

LIST OF APPENDICES

Appendix

ABSTRACT

Towards a Universal Two-Qubit Gate with Self-Assembled InAs Quantum Dot Molecules
by
Colin M. E. Chow

Chair: Duncan G. Steel

Recent studies in self-assembled InAs quantum dots (QDs) for applications in quantum information processing have demonstrated initialization, readout and long decoherence time of an electron spin confined in a single QD. These arguably fulfill three out of the five DiVincenzo criteria[6] for the physical implementation of quantum computation. The task of tackling the two remaining criteria, however, inevitably leads to the requirement of coupling between two electron spin qubits. Based on recent developments in vertically stacked self-assembled InAs quantum dot molecules (QDMs), several advancements in the optical manipulation of two-electron spin states have been made. These include the observation of a long spin decoherence time and the demonstration of optical spin rotation of a *single* qubit defined by the singlet and the triplet states of two electrons confined in a QDM[7, 8]. As a continuation of these studies towards a full *two-qubit* system, this thesis addresses one of the remaining DiVincenzo criteria concerning a universal set of quantum gates. The physical platform for two-qubit gates is provided by two electrons confined in the QDM where the Coulomb exchange interaction gives rise to the singlet and triplet manifolds. This system was first developed and characterized, including a demonstration of entanglement, by Dan Gammon and his group at the Naval Research Laboratory[9, 10, 7]. This thesis begins by developing a unified model based on a single-band-effective-mass Hamiltonian that describes the energy level structure and optical properties, as well as charge stability regions in the presence of an applied bias. In a transverse magnetic field, an eight-level system consisting of four singlet-triplet spin states, four optical excited states and twelve dipole allowed transitions arises. Spin initialization via multi-laser optical pumping is demonstrated with near unity fidelity for three of the spin states, while the remaining one can be achieved by coherent optical pumping using four CW lasers. The effects of dynamic nuclear spin polarization (DNSP) arising from the coupling between the electrons and the surrounding nuclei is evident in the frequency pulling and pushing lineshapes in absorption profiles. This thesis shows that the optical nuclear spin locking that was demonstrated in a single QD earlier[11] is effective in QDMs, yielding a long spin decoherence time of about 1 μs. Spectroscopic evidence suggests that this is accompanied by the first evidence of a narrowing in the Overhauser field distribution. The results reveal that stabilization of nuclear spin polarization in both QDs is achieved by optical manipulations in the top QD, demonstrating the effect of non-local nuclear spin locking. Finally, it is shown theoretically that pulsed excitation results in single spin rotation and in conjunction with the Coulomb exchange interaction, provides the ingredients for a universal two-qubit gate. A feasible experimental demonstration of the two-qubit gate is proposed, along with the methodology for the population readout of individual spin states.

INTRODUCTION

Decades of progress in the study of semiconductor quantum dots (QD) has established the system's applicability in quantum information and quantum computation. In particular, recent achievements in self-assembled InAs/GaAs QDs have included robust spin initialization[12, 13, 14, 15], readout[16, 17] and coherent control[18, 19, 20, 21]. Together with the observation of a long electron spin coherence[11, 22], these conceivably satisfy three out of the five DiVincenzo criteria for the physical implementation of quantum computation[6]. With two remaining criteria to be fulfilled, i. e., scalability and a universal set of gates, the main challenge of this system lies in controlling the interactions between two QDs, which is crucial for universal quantum gate operations and in scaling up the QDs towards a full-fledged quantum processor.

The schemes for realizing a universal quantum gate using electron or hole spins in QDs can be classified into two paradigms. The first is by forging a communication link between two distant QDs through a "flying qubit", which, in most designs, is encoded in the polarization state of a single photon. In the light of these proposals, the entanglement between a photon and a QD-confined electron spin has been demonstrated[23, 24, 25]. To enhance the photon mediated interaction between two isolated QDs, some proposals call for placing the QDs inside optical cavities[26, 27, 28, 29]. Recent developments in line with this approach have included the observation of the coupling between a QD-confined electron spin and the optical field in a photonic crystal cavity[30]. Nonetheless, it remains a considerable technological challenge to couple two QD-confined electron spins via optical field. This is primarily due to the inhomogeneity in spatial positions and optical transition frequencies associated with the Stranski-Krastanov growth of self-assembled QDs.

The second paradigm is the "hard-wiring" of two or more QDs by positioning them in close proximity, forming a so-called quantum dot molecule (QDM). By virtue of tunneling, the wavefunctions of the charge carriers are delocalized and their interaction herein is governed by the Coulomb coupling. In view of recent developments in vertically coupled QDMs, several schemes for implementing two qubit operations have been proposed[31, 32, 33]. Compared to the first paradigm, the "hard-wiring" approach does not seem to possess as many engineering complications as those associated with optical cavities. Besides, fast gate speed in the order of 10 GHz[33], based on the strength of the Coulomb exchange interaction, can be achieved and is largely tunable by the design of the QDMs. Nonetheless, unlike in gate-defined QDs, implementation of a universal two-qubit gate using self-assembled InAs QDMs is not straightforward. Due to the high speed required, electrical gating of the primary coupling mechanism, i.e., Coulomb exchange interaction, becomes impractical. As a result, the implementation of two-qubit gate operations in the computational basis is usually challenging in this system. Therefore, as will be discussed later in this thesis, it is more convenient to use the eigenstates of the system consisting of spin singlet and triplet states for quantum gate operations. Fortunately, this does not degrade the importance of self-assembled InAs QDs for quantum computation since the two bases are simply related by a unitary transformation.

It is to be emphasized that the two paradigms described above are equally important. A combination of both approaches in an integrated framework has been proposed as a scalable architecture for quantum computation by Jones et al[34]. As the performance of this scheme critically depends on the capability of the QDMs to execute a universal set of gate operations, an experimental demonstration of this capability is of paramount importance. In any case, a successful realization of a universal two-qubit gate is significant in its own right because it allows self-assembled InAs QDs to satisfy yet another DiVincenzo criterion. This alone might pave the way for many other applications such as small-scale quantum simulators.

The focus of this thesis is on the “hard-wiring” approach using a vertically stacked, self-assembled InAs QDM. Ever since the seminal paper by Bayer et al.[35], optically active QDMs have been extensively studied in laser spectroscopy. While a majority of the studies are devoted to the identification of different optical transitions in photoluminescence (PL)[36, 37, 38, 39, 40, 9, 41, 42], some advancements in coherent optical manipulation have included the demonstration of a long spin decoherence time[8] and spin rotation[7] of a single qubit defined by the singlet and the triplet states of two electrons confined in a QDM. Nonetheless, the analyses and modeling of the energy level structures of QDMs have thus far been ad hoc and fragmented. One of the objectives of this thesis is to provide a holistic model for the energy level stuctures of QDMs, particularly, those of the two-electron configuration. With the goal of demonstrating a universal two-qubit gate in mind, this work is presented according to a typical engineering methodology, beginning with the design and modeling of the sample. After laying down the conceptual groundworks, more and more physical models are added during the course of this thesis, culminating in a theoretical description of a feasible demonstration of a universal two-qubit gate.

In accordance with the ideology mentioned above, Chapter 1 introduces the sample structure used in this thesis, along with some design concerns. A numerical modeling method is discussed and from its result, the bonding and anti-bonding molecular states are revealed. Chapter 2 attempts to provide a framework for the analysis of bias dependent photoluminescence spectra, where the complexity of the energy level structure is shown to be arising from the Coulomb interaction between charge carriers. This Chapter begins with an introduction to charge configurations in a QDM, followed by the incorporation of Coulomb interaction in the calculation of the energy levels, using the two-electron charge configuration as an example. Some important concepts such as the charge stability plateau and the co-tunneling regime are explained using numerically obtained energy levels of different charge configurations. Finally, the optical transitions for the two-electron configuration are shown, from which the origin of the striking "X-patterns" in photoluminescence spectra are revealed.

In Chapter 3 and beyond, the focus is on the two-electron configuration, since it will eventually serve as the basis for two-qubit operations. The reasoning behind the choice of the operating bias, henceforth known as the "sweet spot", is laid out in Chapter 3. Also given here are the derivations of the optical transition selection rules in nonzero applied magnetic fields. The most important result from Chapter 3 is the eight-level system which will serve as the physical model in subsequent chapters. With the aid of the eight-level model, initialization of the two-electron spin states is accomplished via the process of multi-laser optical pumping and the results are reported at the end of Chapter 3.

Chapter 4 strives to work around a seeming obstacle posed by the hyperfine interaction between the electrons and the nuclear ensemble, which gives rise to bizarre lineshapes in the absorption spectra. Nonetheless, it will be shown that with optical nuclear spin locking, the detrimental effects of nuclear spin fluctuations can be suppressed. Analysis of the resulting dark-state lineshapes reveals long spin coherence among all four spin states.

The eight-level model developed earlier is expanded in Chapter 5 to include pulsed excitation, of which the result gives rise to single spin rotations. This and the Coulomb exchange interaction become the ingredients for a universal two-qubit gate. The issue of spin readout is also discussed here. Finally, a proposed experimental protocol for the demonstration of a universal two-qubit gate is outlined. This thesis concludes with Chapter 6 in which a brief summary and some future directions are given.

CHAPTER I

Modeling Vertically Stacked Self-Assembled Double-Quantum Dots: Sample Structure and Molecular Wavefunctions

Vertically stacked quantum dots (QDs) in III-V semiconductors were first reported by Goldstein et al.[43] in 1985. It is interesting to note that much efforts had been paid back then to the removal of these unwanted “crystallographic defects” in the studies of strained-layer-superlattices. To date, the optical properties of these vertically stacked QDs have been extensively examined for potential applications in quantum information and quantum computation. Although more than two stacked QD layers have been fabricated, most theoretical and experimental studies to date are limited to two QDs. Earlier optical studies of coupled double QDs, however, are performed not on self-assembled stacked QDs, but on QDs fabricated by cleaved edge overgrowth[44], where molecular behavior is first reported. The double-QDs are often regarded as analogous to bound hydrogen atoms in a hydrogen molecule[45, 44]. For this reason, the double-QDs are also known as quantum dot molecules (QDMs). However, one should not take this analogy seriously because molecular behaviors of double-QDs arise only under certain conditions. Due to the tunability of the engineering parameters of double-QDs, their behaviors range from atomic to molecular. Nonetheless, following the popularity of the term, QDM in the following text refers to vertically stacked double-QDs, regardless of the presence or absence of molecular-like states.

In most theoretical models[46, 45, 47] of the QDMs, “molecular” wavefunctions are generated from wavefunctions of individual QDs. The overlap of these single-QD wavefunctions in the barrier between the two QDs forms bonding or anti-bonding molecular states, analogous to the standard molecular orbital theory (MOT), also known as the linear-combination-of-atomic-orbitals (LCAO) method. One can also obtain molecular wavefunctions outside the framework of MOT by solving the Schrödinger equation corresponding to the double potential well of the QDM directly. A comparison between the calculation results from these two models is given in Appendix A where a brief introduction to the MOT in the context of QDMs is also provided. The choice of method is arbitrary but in the face of constraint in computing resources, one method may be preferable to the other depending on the distance between the QDs, also discussed in Appendix A.

Experimentally, molecular characteristics have been observed in photoluminescence (PL) spectra of QDMs[48, 38, 39, 40, 9, 42, 10, 49]. Despite the availability of theoretical models described above, the models presented in the analyses of these spectra are mostly phenomenological and to some extent based on the simplest form of the MOT. Simple matrices are used to represent the Hamiltonian for the behavior of a charge carrier confined in the QDM. Single-QD energies and interaction matrix elements for inter-QD couplings are numerically fitted in ways such that the models approximate the observed energy level structure. While mathematically convenient, these models lack intuitive physical pictures of the interactions between QDs. Besides, if one were to design a QDM system suited for a particular application, one needs to estimate the eigen-energies and interaction matrix elements beforehand. This is where phenomenological models have limited use. As an attempt to paint a more physically accurate picture and to establish a simple QDM design methodology, this chapter presents an alternative modeling technique based on calculated single charge wavefunctions obtained from numerically solving the Schrödinger equation concerning the QDM. To set the stage for this endeavor, let us first review some basic principles of the sample structure in which the QDMs are embeded.

1.1 Sample Structure

The QDM sample structure used in this work is shown in Fig. 1.1. Fabrication of the sample begins with the epitaxial growth of an n-doped ($\sim 10^{15}$ cm^{-3} Si) gallium arsenide (GaAs) buffer layer on an n-type GaAs substrate, serving as the electron reservoir, followed by a 40-nm-thick intrinsic GaAs. Due to lattice mismatch, the growth of subsequent indium arsenide (InAs) on the intrinsic GaAs layer is characterized by Stranski-Krastanov process where nano-scaled islands spontaneously form on a thin wetting layer of InAs. The hemispherical tops of the InAs islands are truncated by using indium-flush technique to create QDs of desired thickness. A tunneling

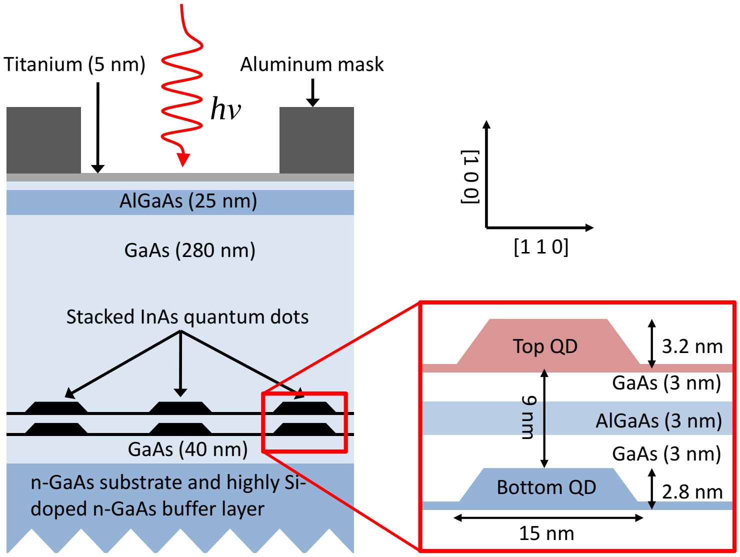

Figure 1.1: Detailed sample structure containing QDM's used in the modeling. The sample is fabricated at the US Naval Research Lab. Inset: Dimensions of constituent QD's and the tunneling barrier.

barrier comprised of GaAs and $Al_{0.3}Ga_{0.7}As$ is then epitaxially grown on the first QD layer. By varying the thickness of the $Al_{0.3}Ga_{0.7}As$ layer and the relative abundance of Al atoms, one can adjust the inter-QD tunneling strength and the quantum-confined Stark shift.

Due to lattice deformation caused by the first QD layer, one would expect a strong correlation in the lateral positions of the QDs in the second layer with that of the first. In fact, the strain field created by the first-layer QDs (stressor) forms nucleation sites for the second-layer QDs[50] and results in self-aligned vertically-stacked double-QDs. These QD complexes are capped by 280-nm-thick intrinsic GaAs. A 25-nm-thick layer of $Al_{0.3}Ga_{0.7}As$ is then grown as a current blocker to reduce the flow of charge carriers. This is then followed by a 5-nm-thick titanium layer that forms the metal gate of a Schottky diode. The aluminum mask with lithographically patterned apertures ($\backsim$1 to 10 μm in diameter) provides isolation of single QDM for laser excitation.

For the QDM considered in this work, the top QD is made thicker than the bottom QD. This causes electron and hole confinement energies of the top QD lower than that of the bottom QD. As a result, the optical transition frequency associated with the top QD (hence the red-QD) is red-shifted from that of the bottom QD (hence the blue-QD). With this arrangement, it is possible to tune the electron energy levels of the two QDs into resonance by applying a moderate gate bias. This is known as the electron-tunneling configuration. The opposite, i. e. the hole-tunneling configuration can be achieved by making the bottom QD thicker than the top QD or by using a p-type substrate[37, 9, 10].

1.2 Metal-Semiconductor Junction

An important feature of the sample structure is the Schottky contact formed between the titanium and GaAs layers which allows us to control the electric field across the sample. As will be seen later in this chapter, the Schottky contact provides the means to tune the quantum confinement energies of the QDs relative to the Fermi level and to each other. The theory of metal-semiconductor junction had been discussed in most solid-state electronics textbooks in the framework of Schottky-Mott relationship (for examples, see [51, 52, 53]). However, the picture is a little more complicated here due to the intrinsic GaAs and $\mathrm{Al_{0.3}Ga_{0.7}As}$ layers. Fortunately, for most quantum related studies of these self-assembled QDMs, the device is normally placed in an optical cryostat with the operating temperature set to around 5 K. Under this condition, the intrinsic layers can be assumed to behave like insulators. The resulting metal-insulator-semiconductor (MIS) structure is also widely discussed in the textbooks.

For intrinsic GaAs at 5 K, the Fermi energy lies close to the mid-gap level. Therefore, in thermal equilibrium, with the assumption of the absence of surface states at the metal-GaAs interface, the Fermi level of the metal is pinned to the mid-gap of the intrinsic GaAs. This gives rise to the “modified” work-function of the metal, φ_i, which is the energy required to excite an electron from the metal to the conduction band of the insulator, in this case the intrinsic GaAs. For the highly doped GaAs layer, however, the Joyce-Dixon approximation[54] can be used to estimate the position of the Fermi level. With a dopant concentration of 10^{15} cm^{-3}, the Fermi level lies in between the donor level and the conduction band edge at 5 K. Since the ionization energy of the dopant is only about 6 meV, the Fermi level in the n-GaAs layer can then be assumed to lie close to the conduction band edge. The resulting energy band diagram is given in Fig. 1.2. Also shown in the figure is the built-in potential, V_{bi}, of the Schottky diode, which is estimated to be $\frac{1}{e}\left(\frac{E_g}{2} + \Delta E_C\right) = 1.04\,\mathrm{V}$, where E_g is the GaAs bandgap and ΔE_C is the GaAs$-\mathrm{Al_{0.3}Ga_{0.7}As}$ conduction band offset. The validity of this estimate is corroborated by the measured I-V curve of the sample and the onset of dense, high-intensity emission lines in bias-dependent PL.

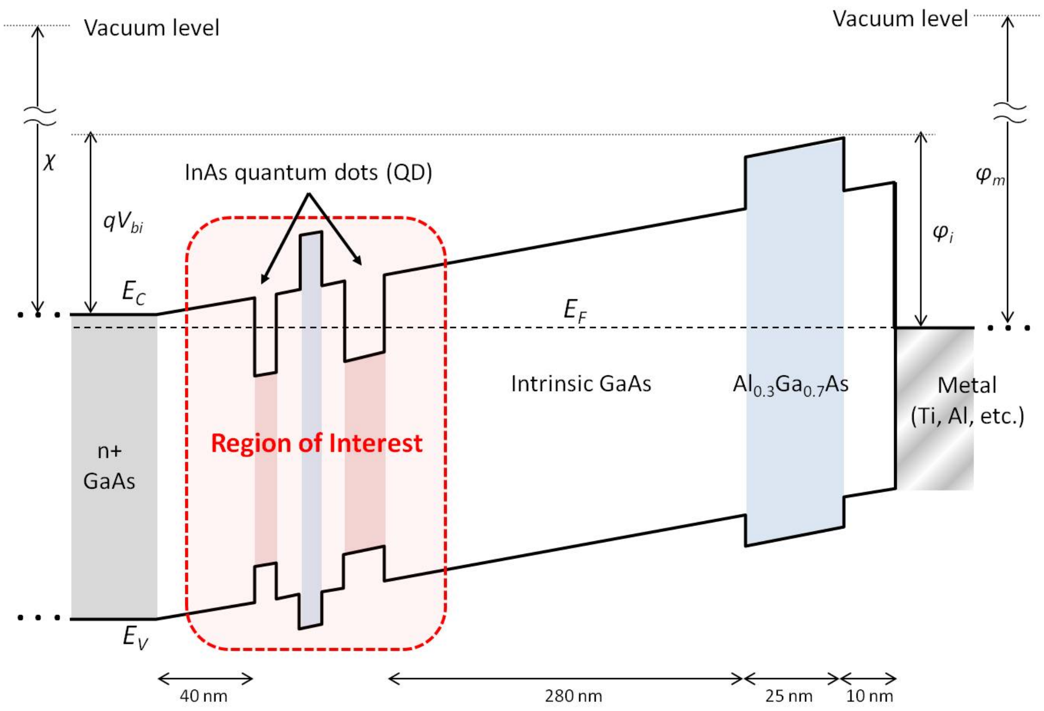

Figure 1.2: Energy band diagram for the QDM sample in n-type, electron-tunneling configuration. E_C, E_V, and E_F denote conduction band-edge, valance band-edge and Fermi energy levels respectively. Other energies labeled above are GaAs electron affinity (χ), metallic work-function (φ_m), and modified work-function (φ_i)

1.3 Confinement of charge carriers in QDs

By applying a bias voltage across the sample, the positions of the potential energies of InAs QDs relative to the Fermi level can be controlled. Confined states for conduction band electrons in the QDs can exist as long as these potentials lie below the Fermi level. However, the existence of confined states for holes is ambiguous from the valence band structure shown in Fig. 1.2. For the n-type-electron-tunneling configuration as shown above, a hole can only be created in the QDs by photo-excitation of an electron-hole pair. One would then expect the hole to tunnel through the intrinsic GaAs barrier towards the metal contact, leaving behind the electron. This scenario contradicts the photoluminescence (PL) results in which quantum confined electron-hole recombination is measured.

Solution to this dilemma lies in the tunneling rate of the hole. To estimate the tunneling rate, consider a hypothetical potential well as shown in Fig. 1.3. E_0 is the ground state energy level for a charged particle confined in the square potential

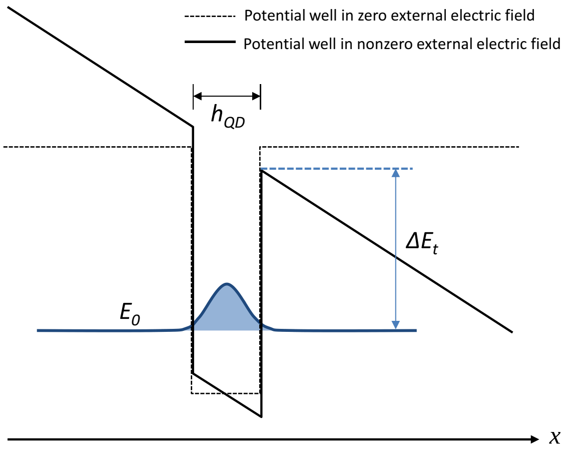

Figure 1.3: A particle in a hypothetical potential well in zero (dashed line) and nonzero (solid line) electric field in x-direction

well represented by the dashed line. When subjected to an electric field, F, in x-direction, the potential well is tilted as shown by the solid line. At the operating temperature of 5 K, thermally activated escape of carrier can be ignored and the lost of carrier is largely due to tunneling[55]. An order-of-magnitude estimate of the tunneling rate, r_t, can be found using one dimensional Wentzel–Kramers–Brillouin (WKB) approximation, which gives[56]

$$r_t = \frac{\pi\hbar}{2m_h^* h_{QD}^2} \exp\left(-\frac{4}{3}\frac{\sqrt{2m_h^*}\Delta E_t^{3/2}}{e\hbar F}\right) \tag{1.1}$$

where h_{QD} is the QD height, m_h^* the hole effective mass and ΔE_t the potential barrier height as labeled in Fig. 1.3. Using Finite-Difference-Time-Domain method (see Appendix B) to solve the Schrödinger equation for a 3-nm thick QD, it is found that $\Delta E_t = 0.095$ eV. The built-in electric field at 0 V gate bias can be estimated from Fig. 1.2 to be 2.1×10^6 V/m. After substituting the appropriate values for other parameters, we have $r_t = 1.5 \times 10^{-15}\ \mathrm{s}^{-1} \approx 0$. Hence the hole remains confined to the QD until recombination occurs. Another commonly used expression for estimating r_t is derived from the analysis concerning the ionization of impurity states by an electric field in semiconductors, and is given by [57, 55, 58, 59]

$$r_t = \frac{eF}{4\sqrt{2m_h^*\Delta E}} \exp\left(-\frac{4}{3}\frac{\sqrt{2m_h^*}\Delta E_t^{3/2}}{e\hbar F}\right)$$

This expression, however, gives an estimate of two orders of magnitude less than that of the first, and therefore have little use here. It is also worth mentioning that for the case of an electron, Eq. 1.1 gives $r_t = 2 \times 10^8\ \mathrm{s}^{-1}$, which is comparable to the electron-hole recombination rate of $10^9\ \mathrm{s}^{-1}$.

1.4 Calculating electron envelope wavefunctions using Finite-Difference-Time-Domain (FDTD) method

Having explained the working principles of the device structure encasing the QDMs, we are in position to calculate the wavefunctions of an electron confined in a QDM. In this chapter, we will confine our discussion to the calculation of single electron wavefunctions while leaving most of the essential electronic and optical properties of QDMs to the next chapter. Nonetheless, one of the most important features of QDMs—inter-QD tunneling, is being discussed here in the context of delocalized or molecular eigenstates.

The geometry of the QDM considered here is based on the XSTM images[41, 9] and is shown in Fig. 1.4. By neglecting the escape of charge carriers via tunneling, one can calculate the wavefunctions of a confined electron by solving the Schrödinger equation in a small volume enclosing the QDM, as indicated by the red-shaded box in Fig. 1.2, instead of considering the entire sample structure. This greatly lessens the demand on computational resources. Care should be taken in defining this region of interest so that the wavefunctions can be assumed to vanish at the boundary. Using the single-band-effective-mass (SBEM) method, the task reduces to the particle-in-a-box problem encountered in introductory quantum mechanics. The choice of SBEM over more rigorous methods like the eight-band $k{\cdot}p$ model is motivated by pragmatism befitting the purpose of the calculation. Due to the inhomogeneity of QDs formed by the Stranski-Krastanov process, the accuracy provided by the latter does not pose an advantage when it comes to experiments. Although the eight-band $k \cdot p$ model may reveal more physical details, e.g. inter-band optical transitions in the presence of strain [60], they are out of the scope of this thesis.

In SBEM, a conduction band electron assumes an effective mass, $m_e^* = m_{r,e}\left(\mathbf{r}\right)\ m_0$, where m_0 is the electron rest mass. The dimensionless quantity $m_{r,e}\left(\mathbf{r}\right)$ is determined by the material at point $\mathbf{r}$. The confinement of an electron in the QDM is due to the conduction band offset between InAs and GaAs which is estimated to be 0.89 eV for bulk materials. This value, however, does not take into account the strain due to lattice mismatch, which may cause a sizable shift in the conduction band offset. Following Ref. [4], corrections to the band offsets due to strain are given by

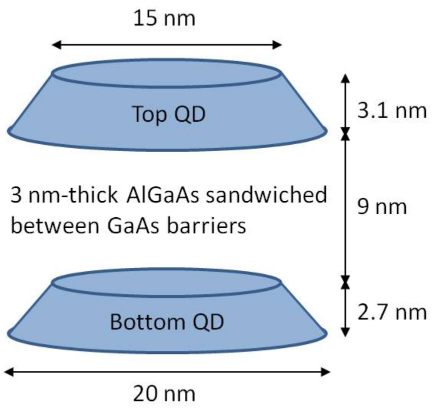

Figure 1.4: Physical dimensions of the QDM used in the calculation of wavefunctions in this chapter.

$-a_c\varepsilon$ and $-a_v\varepsilon$ for conduction band electron and valence band hole respectively, by assuming an in-plane strain orthogonal to growth axis. a_c and a_v are the deformation potentials while ε is the lattice mismatch defined as $\varepsilon = (a_{0,\mathrm{GaAs}} - a_{0,\mathrm{InAs}})/a_{0,\mathrm{InAs}}$, where $a_{0,x}$ denotes the lattice constant of material x. Tables 1.1 and 1.2 summarize the *strain accounted* band parameters and effective masses used in the calculations of wavefunctions for the QDM structure studied in this thesis. Notice that only the heavy-hole is considered here. This is justified from the fact that due to strain, heavy-hole and light-hole energy levels are no longer degenerate at Γ-point. Consequentially, we can ignore the mixing between heavy-hole and light hole and take into account only the heavy-hole in the modeling. This assumption is also corroborated by the lack of indication of heavy-hole-light-hole mixing in experiments.

Bandgap (eV)			Conduction band offset (eV)	
InAs	GaAs	$Al_{0.3}Ga_{0.7}As$	InAs/GaAs	$GaAs/Al_{0.3}Ga_{0.7}As$
0.8724	1.5189	1.9418	0.5491	0.2810

Table 1.1: Band parameters inferred from Ref. [4].

Electron effective mass, m_e^* (m_0)			Heavy-hole effective mass, m_{hh}^* (m_0)		
InAs	GaAs	$Al_{0.3}Ga_{0.7}As$	InAs	GaAs	$Al_{0.3}Ga_{0.7}As$
0.026	0.067	0.092	0.463	0.551	0.609

Table 1.2: Effective masses for electron and heavy-hole from Ref. [4] and [5].

The FDTD procedure explained in Appendix B provides a convenient way to numerically determine the ground state wavefunction of an electron confined in a QDM. With a simple modification discussed in the appendix, the wavefunctions of other low-lying energy eigenstates can also be estimated. As mentioned in the beginning of this chapter, the FDTD method can be implemented in two ways. The first is to solve the Schrödinger equation of the double potential directly while the second is to calculate the wavefunctions of individual QDs, then construct the "molecular wavefunctions" using molecular orbital theory (MOT). While the former approach is straightforward, in FDTD the convergence rate of the calculation procedure is proportional to the energy difference between the ground and first excited states. In general, the larger the inter-QD distance, the smaller the energy splitting between the bonding and anti-bonding states. Therefore, for QDMs with large inter-QD distances, it can be time-consuming to determine the ground state wavefunctions using this direct "brute-force" approach. (See Appendix B) The second way requires more intermediate steps because separate sets of calculations are needed to find the wavefunctions in individual QDs and their wavefunction overlaps. However, for cases with large inter-QD distances and strong quantum confinements, it might be time-saving to follow this approach. In practice, from the point of view of computational resources, the MOT method is more advantageous when $s_t \ll \Delta E_{1,2}$, where s_t is the tunneling coefficient (see Appendix A) and $\Delta E_{1,2}$ is the energy splitting between adjacent energy levels in separate QDs 1 and 2.

1.5 Bonding and anti-bonding states of a single electron confined in a QDM

From preceding section and Appendix A, we learn that the molecular wavefunctions can be obtained in two ways, both using the FDTD method. One by simply solving the Schrödinger equation of the double-QD potential, and the other by employing the MOT to construct delocalized wavefunctions. For the QDM considered here, the result obtained from the MOT is very close to that from the direct solution of the double-QD potential, although only the ground state wavefunctions of individual QDs are taken into account. This arises from the fact that the energy splitting between the ground and first excited states in a single QD ($\geq$ 100 meV) is much larger than the inter-QD tunneling constant, s_t, ($\leq$ 1 meV) for the sample considered here. In this case, however, the time required for directly solving the double-QD Schrödinger equation is longer due to the small energy splitting of the molecular states. Since both results differ only insignificantly, the MOT approach is more advantegeous and is therefore used in the following.

Following Appendix A, the molecular wavefunctions for the ground (bonding)

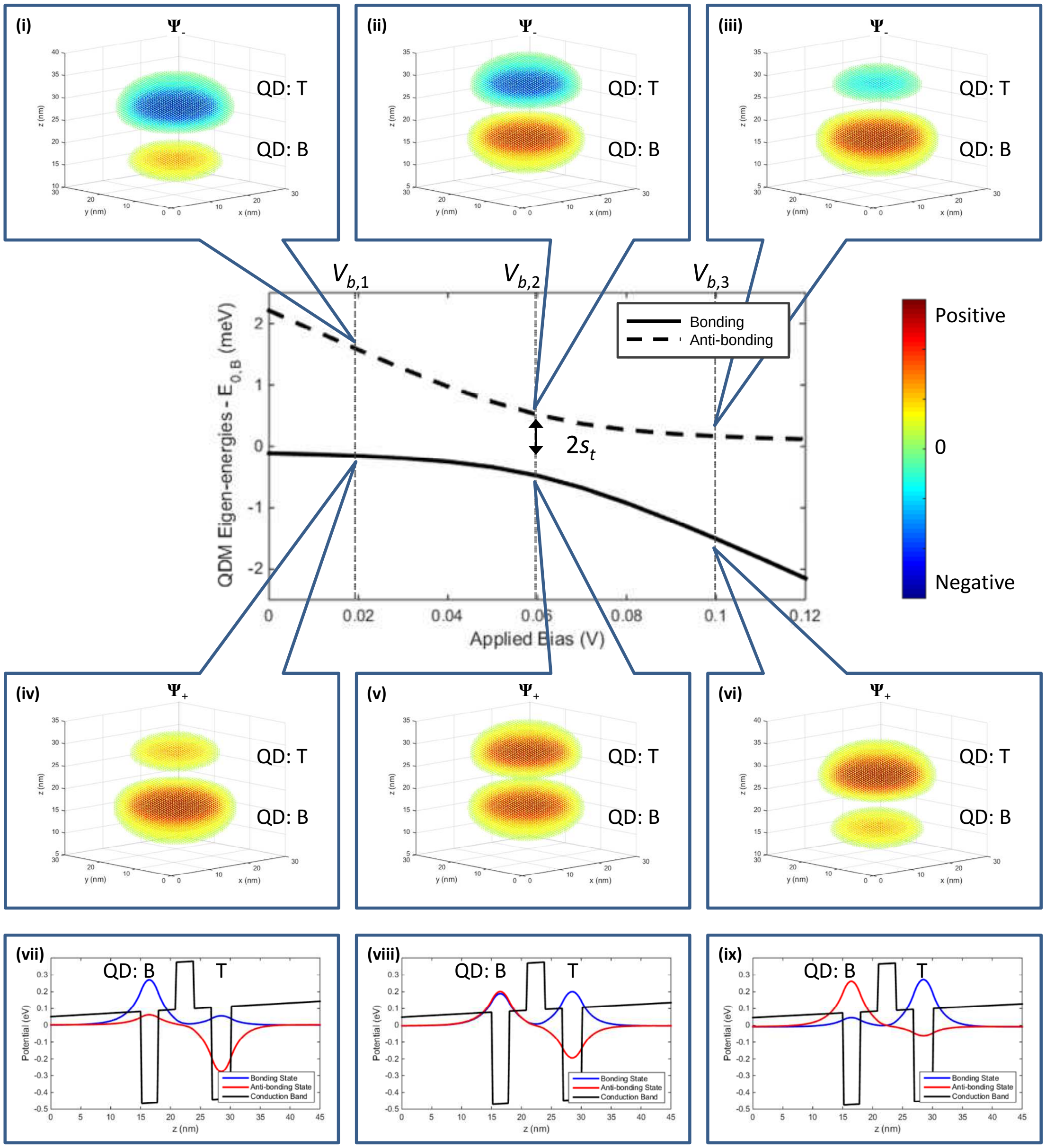

Figure 1.5: Bonding and anti-bonding energy levels as a function of applied bias for the QDM sample described in §1.1. The energies are plotted with respect to the *single-QD* ground state energy level of the bottom QD, $E_{0,\mathrm{B}}$. s_t denotes tunneling constant with a value of around 0.4 meV taken from the anti-crossing at $V_{b,2}$. Inset (i)-(iii): Probability amplitudes of the anti-bonding states, Ψ_-, at bias $V_{b,1}$, $V_{b,2}$ and $V_{b,3}$. B and T denote bottom and top QDs respectively. Inset (iv)-(vi): Probability amplitudes for the bonding states, Ψ_+. Inset (vii)-(ix): Corresponding probability amplitudes along z-direction cutting through the center of the QDM. Solid blue line: ground (bonding) state; solid red line: first excited (anti-bonding) state; and solid black line: conduction band potential.

state, Ψ_+, and the first excited (anti-bonding) state, Ψ_-, are given by

$$\Psi_\pm = \frac{\Psi_{0,\mathrm{B}} - c_\pm \Psi_{0,\mathrm{T}}}{\sqrt{1 + |c_\pm|^2}}$$

where

$$c_\pm = \frac{\alpha_{11} + \beta_{21} - E_\pm (1 + S^*)}{\alpha_{22} + \beta_{12} - E_\pm (1 + S)}$$

Here $\Psi_{0,\mathrm{B}}$ and $\Psi_{0,\mathrm{T}}$ are the ground state wavefunctions of *individual* bottom and top QDs while $E_\pm$ is the eigen-energy of $\Psi_\pm$. This, along with α_{11}, α_{22}, β_{12}, β_{21} and the wavefunction overlap, S, are defined in Appendix A. The eigen-energy as a function of applied bias for the bonding and anti-bonding states are plotted in Fig. 1.5. The emergence of molecular states is characterized by the avoided crossing (anti-crossing) of the energy levels at applied bias $V_{b,2}$, where the ground state energy levels of the individual QDs are on resonance. The smallest energy splitting between the two levels is defined as twice the tunneling constant, s_t, which is roughly 0.4 meV as shown in Fig. 1.5. In the vicinity of $V_{b,2}$, the wavefunctions of the electron are delocalized, given by the symmetric (bonding) and anti-symmetric (anti-bonding) linear combinations of $\Psi_{0,\mathrm{B}}$ and $\Psi_{0,\mathrm{T}}$ (Insets (ii) and (v) of Fig. 1.5). Away from this tunneling resonance, the wavefunctions become localized at individual QDs. As the bias is increased, the energy level for an electron confined in the top QD is shifted (dc Stark shift) roughly by an amount $-\frac{d'}{D} e\Delta V_b \approx -0.033 e\Delta V_b$ relative to that of the bottom QD. Here d' denotes the inter-QD separation, D the distance between the Schottky contact and the substrate and ΔV_b the change in bias. For $V_b < V_{b,2}$, an electron confined in the bottom QD has lower energy than that in the top QD, while for $V_b > V_{b,2}$, the order is reversed. This bias dependent behavior is illustrated in the insets (vii)-(ix) of Fig. 1.5.

1.6 Remark on heavy-hole energy states and conclusion

In §1.1, it is mentioned that the sample is constructed in such a way that the electron energy levels in the two QDs can be brought into tunneling resonance by applying a moderate voltage bias. This sample geometry also dictates that the ground state heavy-hole levels *cannot* be tuned into tunneling resonance with a reasonable voltage bias. Tunnel coupling, however, can still exist between the heavy-hole ground state in the bottom QD and one of the excited states in the top QD[41]. Based on photoluminescence (PL) spectroscopy, the tunneling constant for heavy-hole is measured to be an order of magnitude smaller than that for electron[10, 41, 9, 37]. This is mainly due to the heavier effective mass of a heavy-hole in InAs compared to that of an electron. For the sample structure considered here, the lowest energy heavy-hole state is localized in the top QD, and can be accessed only through photo-excitation. In the bulk of this thesis, only this single QD hole state is considered.

In conclusion, the molecular characteristic of a QDM is signified by the anti-crossing of the ground and excited states as a function of applied bias. Using the FDTD method to solve for electron wavefunctions in individual QDs and followed by the MOT approach, the delocalized bonding and anti-bonding wavefunctions are obtained. The calculated tunneling constant, s_t, agrees with the experimentally measured value of 0.35 meV from PL spectroscopy of a similarly structured sample[7]. As derived in Appendix A, for QDMs with large inter-QD separations, the anti-crossing can be modeled using a simple matrix Hamiltonian[40, 10, 9, 38, 42]

$$\hat{H} = \begin{bmatrix} \alpha_{11} & s_t \\ s_t^* & \alpha_{22} + ed'F \end{bmatrix}$$

This model considers a *single* particle with two energy levels. A QDM, however, can be charged with multiple electrons or holes in various spatial configurations. The Coulomb interaction between these particles gives rise to few-body systems, where each of them posseses unique characteristics. Therefore, many important properties QDMs are only revealed through the interactions between multiple charge carriers, which will be the focus of the next chapter. Nevertheless, the modeling method developed here plays a very important role since its results, i. e., the molecular wavefunctions, will serve as the basis for further studies presented in subsequent chapters.

CHAPTER II

Electronic and Optical Properties of a QDM: Charge Configurations and Optical Resonance Spectra

In the previous chapter, it is shown how the wavefunctions of a confined electron in QDM shifted from atomic-like to molecular-like as the sample bias voltage is changed. In experiments involving optically active QDMs, however, these single particle states are seldom probed just as they are; rather they are always probed jointly with optically excited states where an electron-hole pair is added via optical excitation. With every addition of a charge carrier, a different phenomenon arises. This chapter explores some of these phenomena by constructing their corresponding energy levels using the wavefunctions numerically obtained in the previous chapter. Using the examples of two-electron and doubly-charged exciton configurations, methods for the evaluation of Coulomb interaction matrix elements and the assessment of dipole-allowed optical transitions are also discussed. Towards the end of this chapter, it is shown how the the numerical model reproduces striking 'X-patterns[10, 36, 41, 39, 40, 9]' observed in bias-dependent photoluminescence (PL) spectra of a QDM. The results and concepts developed here serve as the starting point for experimental studies reported in later chapters.

2.1 Basis states and symbols for charge configurations

Due to the difference in the basis states used in this thesis and in some literature[10, 36, 41, 39, 40, 9], a few cautionary notes are necessary before proceeding to the discussions involving multiple charge carriers. In the picture provided by the latter, the presence of two QD sites in a QDM enables spatial arrangements of charge carriers.

For example, an electron can reside in either the top or the bottom QD, while two electrons can be arranged such that each resides in a separate QD, both reside in the top QD or both in the bottom QD. This means the wavefunctions are constructed from basis states specified by the spatial confinement a single electron in either the top or bottom QD, henceforth known as the 'spatial basis'. The use of this basis originated from an intuitive way to visualize the charge configurations, which are represented graphically with 'window diagrams' as shown in Fig. 2.1(a). Although the spatial basis is not used in this thesis for calculations, the window diagrams are used for the purpose of labeling energy levels when convenient, i. e., in regions far away from tunneling resonance. Hence, a brief discussion on them is worthwhile.

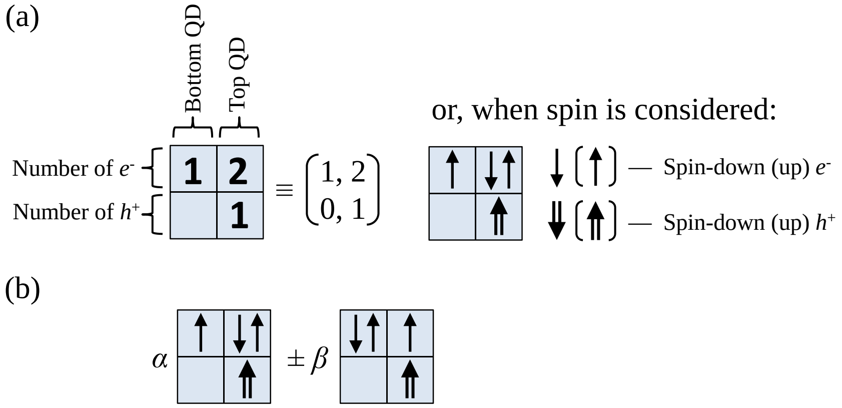

Figure 2.1: Window diagrams for the representations of charge configurations. (a) Without considering the spins, numerals in the upper row represent the number of electrons occupying the bottom QD (left box) and the top QD (right box), while the corresponding numbers in the lower row represent heavy-holes. When spins are taken into account, the numbers are replaced by arrows indicating spin projections. (b) Symbolic representation for a tunnel-coupled state where the +(-) sign denotes bonding (anti-bonding) state.

In a 'window diagram', boxes in the upper row represent the potential wells in the conduction band while the lower row the valance band. The left and right columns indicate the top and bottom QDs, respectively. Charge occupancies are denoted by the numbers in the upper row for electrons (e^-) and the lower row for heavy-holes (h^+). When spins are included, the numbers are replaced by arrows pointing in the directions of spin projections. In some other works, bracketed matrices are used instead of boxes. To illustrate tunnel coupling, symmetric and anti-symmetric linear combinations of charge configurations are symbolically constructed, as shown in Fig. 2.1(b). Although cumbersome in depicting tunnel coupled states, the spatial basis provides a convenient description of the relationship between the energy levels and spatial charge configurations as a function of sample voltage bias. A small drawback of the spatial basis is its potential to mislead due to the fact that the basis states are not orthogonal to each other, i.e., the basis is over-complete. Therefore, extra care must be taken in calculations when using this basis. (See Appendix A)

In this thesis, the basis states are chosen to be the single particle energy eigenstates calculated using the procedure outlined in Chapter 1. In the vicinity of tunneling resonance, this basis is formed by molecular states, while far from tunneling resonance, it is identical to the spatial basis. Here the orthogonality of the basis states makes calculating Coulomb interaction matrix elements convenient. As will be discussed in the next section, multi-particle wavefunctions are constructed from the product states of these single electron or heavy-hole eigenstates. The following notation used to represent a product state in this thesis:

$$|1\uparrow\rangle\,|2\downarrow\rangle\,|2\uparrow\rangle\,|1\Uparrow\rangle \equiv \left(|\Psi_1^e\rangle_1 \otimes |\uparrow\rangle_1\right)\otimes\left(|\Psi_2^e\rangle_2 \otimes |\downarrow\rangle_2\right)\otimes\left(|\Psi_2^e\rangle_3 \otimes |\uparrow\rangle_3\right)\otimes\left(\left|\Psi_1^h\right\rangle_1 \otimes |\Uparrow\rangle_1\right)$$

describes the case where the first electron occupies energy level 1 with a spin-up state, the second and the third level 2, with spin-down and spin-up states, respectively, while the heavy-hole assumes a spin-up state 1 in the valance band. For now, let us ignore the anti-symmetrization for fermionic particles since they will be discussed in the following section. Here Ψ_i^e and Ψ_i^h are i-th eigenstates for electron and heavy-hole, respectively, in the conduction and the valance band. Spin states are denoted by a simple arrow for the electron and a double-line arrow for the heavy-hole. In the simplified notation on the left hand side of the equation above, numerical indices identifying the particles are dropped as the identification is implied in the ordering of the basis states.

2.2 Two-electron states: The $\mathcal{H}_2$ block of fermionic Fock space and Coulomb interaction

When two or more particles are confined in a QDM, interaction between particles arises, along with additional charge and spin configurations. The formalism of fermionic operators and Fock space provides a systematic way for the evaluation of the interaction matrix elements involving multiple particles, as will be demonstrated in this section for two electrons. If we assume that an electron confined in a QDM can occupy one of the states $|1\downarrow\rangle$, $|1\uparrow\rangle$, $|2\downarrow\rangle$ and $|2\uparrow\rangle$, then for two-electrons, there are six possible combinations, namely, $|1\downarrow, 1\uparrow\rangle$, $|1\downarrow, 2\downarrow\rangle$, $|1\downarrow, 2\uparrow\rangle$, $|1\uparrow, 2\downarrow\rangle$, $|1\uparrow, 2\uparrow\rangle$ and $|2\downarrow, 2\uparrow\rangle$. The notation here follows that of Appendix C, e. g., $|1\downarrow, 1\uparrow\rangle = \hat{a}^{\dagger}(1\uparrow)\,\hat{a}^{\dagger}(1\downarrow)\,|\varnothing\rangle \equiv \frac{1}{\sqrt{2}}\left(|1\downarrow\rangle\,|1\uparrow\rangle - |1\uparrow\rangle\,|1\downarrow\rangle\right)$, where $\hat{a}^{\dagger}(1\uparrow)$ denotes the fermionic creation operator for the quantum state $|\Psi_1^e\rangle \otimes |\uparrow\rangle$ and $|\varnothing\rangle$ represents the vacuum state. In this particular case, the six quantum states above span the two-electron Hilbert space in our QDM, also known as the $\mathcal{H}_2$ block of the fermionic Fock space, $\mathcal{F}$. Note that due to Pauli exclusion principle, double occupancy of the same state is not allowed. As shown in Appendix C, this can be viewed as the consequence of the anti-commutation relations for fermionic operators.

Using the formalism of fermionic operators, the interaction Hamiltonian for a single particle, $H^{(1)}$, is given by

$$H^{(1)} = \sum_{\alpha,\beta} \langle\alpha|\, V^{(1)}\, |\beta\rangle\, \hat{a}^{\dagger}(\alpha)\, \hat{a}(\beta) \tag{2.1}$$

where $\langle\alpha|\, V^{(1)}\, |\beta\rangle$ is the interaction matrix element for quantum states $|\alpha\rangle$ and $|\beta\rangle$, which, in coordinate representation, takes the form

$$\langle\alpha|\, V^{(1)}\, |\beta\rangle = \int d\mathbf{r}\Psi_{\alpha}^{*}(\mathbf{r})\, V^{(1)}(\mathbf{r})\, \Psi_{\beta}(\mathbf{r})$$

For interactions involving two particles, e. g. Coulomb interaction, the Hamiltonian is

$$H^{(2)} = \frac{1}{2} \sum_{\alpha,\beta,\gamma,\delta} V^{(2)}_{\alpha\beta,\gamma\delta}\hat{a}^{\dagger}(\alpha)\, \hat{a}^{\dagger}(\beta)\, \hat{a}(\gamma)\, \hat{a}(\delta) \tag{2.2}$$

where

$$\begin{aligned} V^{(2)}_{\alpha\beta,\gamma\delta} &= \left(\langle\alpha| \otimes \langle\beta|\right) V^{(2)} \left(|\gamma\rangle \otimes |\delta\rangle\right) \\ &= \iint d\mathbf{r}_1 d\mathbf{r}_2 \Psi_{\alpha}^{*}(\mathbf{r}_1)\, \Psi_{\beta}^{*}(\mathbf{r}_2)\, V^{(2)}(\mathbf{r}_1, \mathbf{r}_2)\, \Psi_{\gamma}(\mathbf{r}_2)\, \Psi_{\delta}(\mathbf{r}_1) \end{aligned} \tag{2.3}$$

in coordinate representation. It is important to note that the basis states for both Eq. (2.1) and (2.2) are those of two-particle states, $|\alpha, \beta\rangle$. The factor $\frac{1}{2}$ in Eq. (2.2) arises from double counting because $|\beta, \alpha\rangle = -\,|\alpha, \beta\rangle$, as shown in Appendix C.

In the case of two electrons confined in a QDM, the Hamiltonian consists of confinement potential for individual electron, H_0, and Coulomb interaction, V^{Cou}. Since the single particle basis states are chosen to be the molecular eigenstates of H_0 from Chapter 1, the nonzero terms in the Hamiltonian for particle confinement,

H^{Con}, in Eq. (2.1) are

$$\begin{aligned}
H^{\text{Con}} &= \langle 1\downarrow| H_0 |1\downarrow\rangle \hat{a}^\dagger(1\downarrow)\hat{a}(1\downarrow) + \langle 1\uparrow| H_0 |1\uparrow\rangle \hat{a}^\dagger(1\uparrow)\hat{a}(1\uparrow) \\
&\quad + \langle 2\downarrow| H_0 |2\downarrow\rangle \hat{a}^\dagger(2\downarrow)\hat{a}(2\downarrow) + \langle 2\uparrow| H_0 |2\uparrow\rangle \hat{a}^\dagger(2\uparrow)\hat{a}(2\uparrow) \\
&= E_1\hat{a}^\dagger(1\downarrow)\hat{a}(1\downarrow) + E_1\hat{a}^\dagger(1\uparrow)\hat{a}(1\uparrow) + E_2\hat{a}^\dagger(2\downarrow)\hat{a}(2\downarrow) + E_2\hat{a}^\dagger(2\uparrow)\hat{a}(2\uparrow)
\end{aligned}$$

Here $E_{1(2)} = E_{+(-)}$ is the eigen-energy from Chapter 1. The matrix representation of H^{Con} is therefore diagonal:

$$H^{\text{Con}} = \begin{bmatrix} 2E_1 & 0 & 0 & 0 & 0 & 0 \\ 0 & E_1+E_2 & 0 & 0 & 0 & 0 \\ 0 & 0 & E_1+E_2 & 0 & 0 & 0 \\ 0 & 0 & 0 & E_1+E_2 & 0 & 0 \\ 0 & 0 & 0 & 0 & E_1+E_2 & 0 \\ 0 & 0 & 0 & 0 & 0 & 2E_2 \end{bmatrix} \tag{2.4}$$

in the basis $\{|1\downarrow,1\uparrow\rangle,\ |1\downarrow,2\downarrow\rangle,\ |1\downarrow,2\uparrow\rangle,\ |1\uparrow,2\downarrow\rangle,\ |1\uparrow,2\uparrow\rangle,\ |2\downarrow,2\uparrow\rangle\}$.

For the Coulomb interaction term, $H^{(2)} = H^{\text{Cou}}$, we have

$$V^{(2)} = V^{\text{Cou}} = \frac{e^2}{4\pi\varepsilon}\frac{1}{|\mathbf{r}_1 - \mathbf{r}_2|}$$

where ε is the permittivity of the underlying semiconductor material. Substituting the expression for Coulomb interaction above into Eq. (2.3), it is easy to show that

$$V^{\text{Cou}}_{\alpha\beta,\gamma\delta} = V^{\text{Cou}}_{\beta\alpha,\delta\gamma} = \left(V^{\text{Cou}}_{\gamma\delta,\alpha\beta}\right)^*$$

The matrix elements for Coulomb interaction can be written in terms of $V^{\text{Cou}}_{\alpha\beta,\gamma\delta}$ using Eq. (2.2). For example, to evaluate the matrix element below:

$$\langle 1\downarrow,1\uparrow| H^{\text{Cou}} |1\downarrow,1\uparrow\rangle = \langle 1\downarrow,1\uparrow| \frac{1}{2}\sum_{\alpha,\beta,\gamma,\delta} V^{\text{Cou}}_{\alpha\beta,\gamma\delta}\hat{a}^\dagger(\alpha)\hat{a}^\dagger(\beta)\hat{a}(\gamma)\hat{a}(\delta)|1\downarrow,1\uparrow\rangle$$

first note that $\langle 1\downarrow,1\uparrow| \hat{a}^\dagger(\alpha)\hat{a}^\dagger(\beta)\hat{a}(\gamma)\hat{a}(\delta)|1\downarrow,1\uparrow\rangle$ is nonzero if (α,β), $(\gamma,\delta) = (1\downarrow,1\uparrow)$ or $(1\uparrow,1\downarrow)$. But $V^{\text{Cou}}_{\alpha\beta,\gamma\delta} = (\langle\alpha|\otimes\langle\beta|)\,V^{\text{Cou}}\,(|\gamma\rangle\otimes|\delta\rangle)$ is nonzero only if the spin projection of α equals that of δ, and similarly for the pair β and γ. Hence, the two sets of values $(\alpha,\beta,\gamma,\delta)$ which contribute to the matrix element above are

$(1\downarrow, 1\uparrow, 1\uparrow, 1\downarrow)$ and $(1\uparrow, 1\downarrow, 1\downarrow, 1\uparrow)$, and we have

$$\begin{aligned}
\langle 1\downarrow, 1\uparrow| H^{\text{Cou}} |1\downarrow, 1\uparrow\rangle &= \langle 1\downarrow, 1\uparrow| \frac{1}{2} V^{\text{Cou}}_{11,11} \hat{a}^{\dagger}(1\downarrow)\hat{a}^{\dagger}(1\uparrow)\hat{a}(1\uparrow)\hat{a}(1\downarrow)|1\downarrow, 1\uparrow\rangle \\
&\quad + \langle 1\downarrow, 1\uparrow| \frac{1}{2} V^{\text{Cou}}_{11,11} \hat{a}^{\dagger}(1\uparrow)\hat{a}^{\dagger}(1\downarrow)\hat{a}(1\downarrow)\hat{a}(1\uparrow)|1\downarrow, 1\uparrow\rangle \\
&= V^{\text{Cou}}_{11,11}
\end{aligned}$$

Here the electron spin is dropped in the notation $V^{\text{Cou}}_{\alpha\beta,\gamma\delta}$ since it is understood that Coulomb interaction is spin conserving.

In similar fashion to the example above, all matrix elements of Coulomb interaction can be found and are given below in the same basis as Eq. (2.4):

$$H^{\text{Cou}} = \begin{bmatrix}
V^{\text{Cou}}_{11,11} & 0 & V^{\text{Cou}}_{11,12} & -V^{\text{Cou}}_{11,12} & 0 & V^{\text{Cou}}_{11,22} \\
0 & V^{\text{Cou}}_{12,21} - V^{\text{Cou}}_{12,12} & 0 & 0 & 0 & 0 \\
\left(V^{\text{Cou}}_{11,12}\right)^{*} & 0 & V^{\text{Cou}}_{12,21} & -V^{\text{Cou}}_{12,12} & 0 & V^{\text{Cou}}_{12,22} \\
-\left(V^{\text{Cou}}_{11,12}\right)^{*} & 0 & -V^{\text{Cou}}_{12,12} & V^{\text{Cou}}_{12,21} & 0 & -V^{\text{Cou}}_{12,22} \\
0 & 0 & 0 & 0 & V^{\text{Cou}}_{12,21} - V^{\text{Cou}}_{12,12} & 0 \\
\left(V^{\text{Cou}}_{11,22}\right)^{*} & 0 & \left(V^{\text{Cou}}_{12,22}\right)^{*} & -\left(V^{\text{Cou}}_{12,22}\right)^{*} & 0 & V^{\text{Cou}}_{22,22}
\end{bmatrix}$$

Away from "tunneling resonance", i. e., $|E_2 - E_1| \gg \left|V^{\text{Cou}}_{11,11} - V^{\text{Cou}}_{12,21}\right|, \left|V^{\text{Cou}}_{22,22} - V^{\text{Cou}}_{12,21}\right|$, the off-diagonal Coulomb terms $V^{\text{Cou}}_{11,12}$, $V^{\text{Cou}}_{12,22}$ and $V^{\text{Cou}}_{11,22}$ are negligible. Setting these terms to zero, the eigen-energies and eigenstates of the Hamiltonian $H^{\text{Con}} + H^{\text{Cou}}$ are given by:

$$\begin{array}{llclcl}
\text{Eigen-energies:} & \text{Eigenstates:} & & & & \\
2E_1 + V^{\text{Cou}}_{11,11} & |1\downarrow, 1\uparrow\rangle & = & |1\rangle|1\rangle \otimes \frac{|\downarrow\rangle|\uparrow\rangle - |\uparrow\rangle|\downarrow\rangle}{\sqrt{2}} & = & |S^{1,1}\rangle \\
2E_2 + V^{\text{Cou}}_{22,22} & |2\downarrow, 2\uparrow\rangle & = & |2\rangle|2\rangle \otimes \frac{|\downarrow\rangle|\uparrow\rangle - |\uparrow\rangle|\downarrow\rangle}{\sqrt{2}} & = & |S^{2,2}\rangle \\
E_1 + E_2 + V^{\text{Cou}}_{12,21} + V^{\text{Cou}}_{12,12} & \frac{|1\downarrow,2\uparrow\rangle - |1\uparrow,2\downarrow\rangle}{\sqrt{2}} & = & \frac{|1\rangle|2\rangle + |2\rangle|1\rangle}{\sqrt{2}} \otimes \frac{|\downarrow\rangle|\uparrow\rangle - |\uparrow\rangle|\downarrow\rangle}{\sqrt{2}} & = & |S^{1,2}\rangle \\
E_1 + E_2 + V^{\text{Cou}}_{12,21} - V^{\text{Cou}}_{12,12} & |1\downarrow, 2\downarrow\rangle & = & \frac{|1\rangle|2\rangle - |2\rangle|1\rangle}{\sqrt{2}} \otimes |\downarrow\rangle|\downarrow\rangle & = & |T^{1,2}_{-}\rangle \\
E_1 + E_2 + V^{\text{Cou}}_{12,21} - V^{\text{Cou}}_{12,12} & \frac{|1\downarrow,2\uparrow\rangle + |1\uparrow,2\downarrow\rangle}{\sqrt{2}} & = & \frac{|1\rangle|2\rangle - |2\rangle|1\rangle}{\sqrt{2}} \otimes \frac{|\downarrow\rangle|\uparrow\rangle + |\uparrow\rangle|\downarrow\rangle}{\sqrt{2}} & = & |T^{1,2}_{0}\rangle \\
E_1 + E_2 + V^{\text{Cou}}_{12,21} - V^{\text{Cou}}_{12,12} & |1\uparrow, 2\uparrow\rangle & = & \frac{|1\rangle|2\rangle - |2\rangle|1\rangle}{\sqrt{2}} \otimes |\uparrow\rangle|\uparrow\rangle & = & |T^{1,2}_{+}\rangle
\end{array} \tag{2.5}$$

The eigenstates consist of spin-zero singlet states, represented by S, and spin-1 triplet states, by T. Subscripts denote spin projections, while charge configurations are given in superscripts. Note that the triplet states are degenerate. The energy splitting between $|S^{1,2}\rangle$ and the triplet states is given by $2V^{\text{Cou}}_{12,12}$, in which $V^{\text{Cou}}_{12,12}$ is known as the exchange integral, sometimes written as J_{ex}. Following the order of the eigenstates above, we can rewrite the Hamiltonian $H^{\text{Con}} + H^{\text{Cou}}$ in singlet-triplet basis as:

$$H^{\text{Con}}+H^{\text{Cou}} = \begin{bmatrix} 2E_1 + V^{\text{Cou}}_{11,11} & V^{\text{Cou}}_{11,22} & \sqrt{2}V^{\text{Cou}}_{11,12} & 0 & 0 & 0 \\ \left(V^{\text{Cou}}_{11,22}\right)^* & 2E_2 + V^{\text{Cou}}_{22,22} & \sqrt{2}\left(V^{\text{Cou}}_{12,22}\right)^* & 0 & 0 & 0 \\ \sqrt{2}\left(V^{\text{Cou}}_{11,12}\right)^* & \sqrt{2}V^{\text{Cou}}_{12,22} & E^{1,2}_S & 0 & 0 & 0 \\ 0 & 0 & 0 & E^{1,2}_T & 0 & 0 \\ 0 & 0 & 0 & 0 & E^{1,2}_T & 0 \\ 0 & 0 & 0 & 0 & 0 & E^{1,2}_T \end{bmatrix} \tag{2.6}$$

Here the off-diagonal Coulomb terms $V^{\text{Cou}}_{11,12}$, $V^{\text{Cou}}_{12,22}$ and $V^{\text{Cou}}_{11,22}$ are restored. The terms $E^{1,2}_S = E_1 + E_2 + V^{\text{Cou}}_{12,21} + V^{\text{Cou}}_{12,12}$ and $E^{1,2}_T = E_1 + E_2 + V^{\text{Cou}}_{12,21} - V^{\text{Cou}}_{12,12}$ are the energy levels of the singlet and triplet states, respectively, in the absence of off-diagonal Coulomb coupling, for the charge configuration where levels 1 and 2 are each occupied by an electron. Eq. (2.6) above shows that the singlet state $|S^{1,2}\rangle$ is coupled to states $|S^{1,1}\rangle$ and $|S^{2,2}\rangle$ with coupling constants given by $\sqrt{2}V^{\text{Cou}}_{11,12}$ and $\sqrt{2}V^{\text{Cou}}_{12,22}$ respectively, whereas the triplet states are isolated. This is due to the fact that Coulomb interaction is spin conserving, i. e., it does not affect the spin states of the electrons.

Using the Coulomb matrix elements calculated from the wavefunctions obtained in Chapter 1, the eigen-energies for the Hamiltonian in Eq. (2.6) are plotted in Fig. 2.2. For a better display of the anti-crossing, the energy level of the triplets, $E^{1,2}_T$, is used as the reference in the main plot, while the original energy levels are given in the inset. As one expects from Eq. (2.6), the coupling between $|S^{1,1}\rangle$ and $|S^{1,2}\rangle$ gives rise to an anti-crossing (solid lines), while the three-fold degenerate triplet states (dashed line) remain uncoupled. Away from the anti-crossing, the wavefunctions of the electrons become localized in individual QDs, and it is convenient to label the energy levels with the window diagrams representing charge configurations. Here the anti-crossing between $|S^{1,2}\rangle$ and $|S^{2,2}\rangle$ occurs at a very high bias around 1.6 V, outside of the plot range. The energy splitting between $|S^{1,1}\rangle$ and $|S^{1,2}\rangle$ at the anti-crossing is given by

$$\Delta_{2e^-} = \sqrt{\left(E_2 - E_1 + V^{\text{Cou}}_{12,21} + V^{\text{Cou}}_{12,12} - V^{\text{Cou}}_{11,11}\right)^2 + 8\left|V^{\text{Cou}}_{11,12}\right|^2}$$

For the sample considered here, Δ_{2e^-} is typically around $3s_t$, where s_t is the tunneling constant from Chapter 1.

Although somewhat extraneous to the discussion here, it is interesting to note the relation between Eq. (2.6) and the Hund-Mulliken model[9, 7], often used as the toy model to describe the energy level structure for two-electron states in QDMs. If we

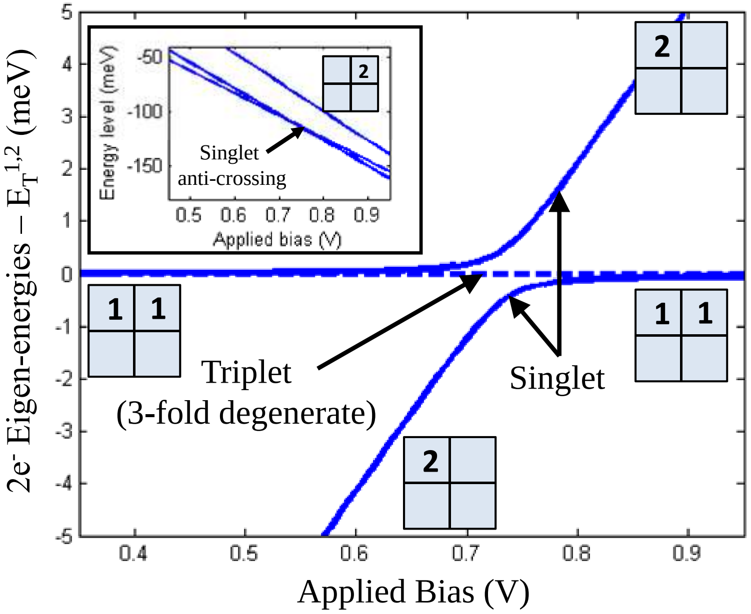

Figure 2.2: Calculated eigen-energies for two electrons confined in a QDM as a function of applied bias. The energy levels are plotted with $E_T^{1,2}$ as the reference. In the main plot, only eigen-energies for states $|S^{1,1}\rangle$, $|S^{1,2}\rangle$, and the triplets are shown. The original energy levels are included in the inset where the eigen-energy for state $|S^{2,2}\rangle$ can also be found. Charge configurations in regions away from the anti-crossing are labeled by window diagrams.

replace the eigenstates $|1\rangle$ and $|2\rangle$ in Eq. (2.6) by $|B\rangle$ and $|T\rangle$ to indicate the occupation of an electron in the bottom and top QD, respectively, and also change $2E_1$, $2E_2$, $V^{\text{Cou}}_{11,12}$, $V^{\text{Cou}}_{12,22}$, and $V^{\text{Cou}}_{11,22}$ to $2E_1' - ed'F$, $2E_2' + ed'F$, $-s_t$, $-s_t$ and 0, respectively, we arrive at

$$H^{\text{HM}} = \begin{bmatrix} 2E_1' + V^{\text{Cou}}_{11,11} - ed'F & 0 & -\sqrt{2}s_t & 0 & 0 & 0 \\ 0 & 2E_2' + V^{\text{Cou}}_{22,22} + ed'F & -\sqrt{2}s_t^* & 0 & 0 & 0 \\ -\sqrt{2}s_t^* & -\sqrt{2}s_t & E_S' & 0 & 0 & 0 \\ 0 & 0 & 0 & E_T' & 0 & 0 \\ 0 & 0 & 0 & 0 & E_T' & 0 \\ 0 & 0 & 0 & 0 & 0 & E_T' \end{bmatrix} \tag{2.7}$$

Here $E_S' = E_1' + E_2' + V^{\text{Cou}}_{12,21} + V^{\text{Cou}}_{12,12}$ and $E_T' = E_1' + E_2' + V^{\text{Cou}}_{12,21} - V^{\text{Cou}}_{12,12}$, while s_t, d' and F are similarly defined as in Chapter 1. The Hund-Mulliken model given in Eq. (2.7) above provides a phenomenological description of the bias-dependent energy levels in singlet-triplet basis analogous to Eq. (2.6). However, here the single electron states are localized, i. e., in spatial basis. The coupling between the singlet states are given in terms of the tunnling constant as $-\sqrt{2}s_t$. This can be derived if one assumes that the "tunneling interaction" takes the form $V^{\mathrm{Tun}} = -\sum_{\alpha,\beta}\left(1-\delta_{\alpha,\beta}\right)s_t\hat{a}^\dagger\left(\alpha\right)\hat{a}\left(\beta\right)$, where $\alpha,\beta=\{B,T\}$ and $\delta_{\alpha,\beta}$ is the Kronecker delta. Here $\hat{a}^\dagger$ and $\hat{a}$ operate only on the non-spin portion of the wavefunctions. It can be shown that $\langle B\downarrow, B\uparrow|\, V^{\mathrm{Tun}}\frac{1}{\sqrt{2}}\left(|B\downarrow,T\uparrow\rangle-|B\uparrow,T\downarrow\rangle\right)=-\sqrt{2}s_t$.

2.3 Other examples of charge configurations: Neutral and charged excitons

Both single- and two-electron charge configurations discussed in Chapter 1 and in previous section constitute part of the *optical ground states* of the system. From Chapter 1, for the sample structure under consideration, a hole can only exist due to optical excitation. Therefore, whenever a charge configuration contains a hole, it is known to be part of the *optical excited states*. Using the same method presented in previous section, the Coulomb matrix elements for the optical excited states, and subsequently the eigen-energies, can be calculated. However, while the electrons in the optical ground states are indistinguishable, in this thesis, the hole in the optical excited states is assumed to be distinguishable from the electrons. Consequentially, certain aspects of the exciton such as the electron-hole exchange interaction, which arises from the symmetry breaking of underlying materials, are not accounted for. Nonetheless, as shown in other works[40, 39, 9, 10], these effects can be "artificially" included in the Coulomb matrix elements *a posteriori*. For more rigorous treatments of the exciton, interested readers are encouraged to consult works on group theoretical methods[61, 62, 63].

As mentioned in Chapter 1, only the two lowest-lying heavy-hole states are considered in this thesis. The sample structure used here dictates that tunneling between the two QDs cannot occur for the heavy-hole within reasonable range of applied bias, i. e., the heavy-hole wavefunctions are localized within the bias of interest. Furthermore, for this sample, the energy separation between the two heavy-hole states is larger than the energy shift due to Coulomb interaction. For this reason, the heavy-hole states remain localized in the presence of Coulomb interaction. Consequentially, we can ignore the off-diagonal Coulomb matrix elements that involve different hole states. This reduces the matrix representations of Coulomb interaction to block-diagonal matrices. We can therefore solve for the eigenstates separately for configurations containing different hole energy levels. The simplest example of an optical excited state is the neutral exciton, denoted by $\mathcal{X}^0$, to be discussed in the following. In addition, since the subsequent chapters focus on the two-electron system, its corresponding optical excited state, the doubly-charged exciton, $\mathcal{X}^{2-}$, is also presented in this section. In the notation used here, $\mathcal{X}$ represents an exciton while the superscript indicates the number of additional charges present in the QDM. For example, an $\mathcal{X}^{2-}$ state contains three electrons and a heavy-hole. Since there are two possible ways for three electrons to occupy two energy levels, the $\mathcal{X}^{2-}$manifold contains four charge configurations, assuming that the heavy-hole can occupy one of its two energy levels. Although the $\mathcal{X}^{1-}$(trion) and $\mathcal{X}^{3-}$ configurations are not discussed here, the procedure given below can be easily used to calculate their energy levels.

For the case of a neutral exciton consisting of an electron-hole pair, the basis states are:

$$\begin{gathered}\{|1\downarrow\rangle\,|h\Downarrow\rangle\,,\ |2\downarrow\rangle\,|h\Downarrow\rangle\,,\ |1\downarrow\rangle\,|h\Uparrow\rangle\,,\ |2\downarrow\rangle\,|h\Uparrow\rangle\\ |1\uparrow\rangle\,|h\Downarrow\rangle\,,\ |2\uparrow\rangle\,|h\Downarrow\rangle\,,\ |1\uparrow\rangle\,|h\Uparrow\rangle\,,\ |2\uparrow\rangle\,|h\Uparrow\rangle\}\end{gathered}$$

where h represents either one of the two lowest-lying heavy-hole eigenstates. From Eq. (2.1) and (2.2), the matrix elements for the exciton Hamiltonian, $H^{\mathcal{X}^0} = H^{\text{Con}} + H^{\text{Cou}} + E_g\hat{I}$, can be found easily:

$$H^{\mathcal{X}^0} = \begin{bmatrix} E_1^{(\mathcal{X}^0)} & -V^{\text{Cou}}_{1h,h2} & 0 & 0 & 0 & 0 & 0 & 0 \\ -\left(V^{\text{Cou}}_{1h,h2}\right)^* & E_2^{(\mathcal{X}^0)} & 0 & 0 & 0 & 0 & 0 & 0 \\ 0 & 0 & E_1^{(\mathcal{X}^0)} & -V^{\text{Cou}}_{1h,h2} & 0 & 0 & 0 & 0 \\ 0 & 0 & -\left(V^{\text{Cou}}_{1h,h2}\right)^* & E_2^{(\mathcal{X}^0)} & 0 & 0 & 0 & 0 \\ 0 & 0 & 0 & 0 & E_1^{(\mathcal{X}^0)} & -V^{\text{Cou}}_{1h,h2} & 0 & 0 \\ 0 & 0 & 0 & 0 & -\left(V^{\text{Cou}}_{1h,h2}\right)^* & E_2^{(\mathcal{X}^0)} & 0 & 0 \\ 0 & 0 & 0 & 0 & 0 & 0 & E_1^{(\mathcal{X}^0)} & -V^{\text{Cou}}_{1h,h2} \\ 0 & 0 & 0 & 0 & 0 & 0 & -\left(V^{\text{Cou}}_{1h,h2}\right)^* & E_2^{(\mathcal{X}^0)} \end{bmatrix}$$

Here $E_1^{(\mathcal{X}^0)} = E_1 + E_h + E_g - V^{\text{Cou}}_{1h,h1}$ and $E_2^{(\mathcal{X}^0)} = E_2 + E_h + E_g - V^{\text{Cou}}_{2h,h2}$, where E_g is the bandgap. Since $H^{\mathcal{X}^0}$ is block-diagonal with four identical 2×2 matrices, there are two eigen-energies in this system where each of them is four-fold degenerate. In reality, however, due to the strain-induced breaking of the S_4-symmetry[63], the degeneracy is lifted, causing exciton fine structure splittings, also known as electron-hole exchange splittings, of about 0.1 meV[40, 39, 9, 10]. Since these fine structure splittings are much smaller compared to the energy splitting at the anti-crossing, they are ignored for the moment. The energy level structure for a neutral exciton resembles that of a single electron, with the energy splitting at the anti-crossing given by

$$\Delta_{\mathcal{X}^0} = \sqrt{\left(E_2 - E_1 + V^{\mathrm{Cou}}_{1h,h1} - V^{\mathrm{Cou}}_{2h,h2}\right)^2 + 4\left|V^{\mathrm{Cou}}_{1h,h2}\right|^2}$$

Another charge configuration having equally simple energy level structure as the neutral exciton is the doubly-charged exciton, $\mathcal{X}^{2-}$, which consists of two spin-paired electrons and a neutral exciton. It has the same number of basis states as the neutral exciton, here written as:

$$\{|1\downarrow,1\uparrow,2\downarrow\rangle\,|h\Downarrow\rangle\,,\ |1\downarrow,2\downarrow,2\uparrow\rangle\,|h\Downarrow\rangle\,,\ |1\downarrow,1\uparrow,2\downarrow\rangle\,|h\Uparrow\rangle\,,\ |1\downarrow,2\downarrow,2\uparrow\rangle\,|h\Uparrow\rangle\,,$$
$$|1\downarrow,1\uparrow,2\uparrow\rangle\,|h\Downarrow\rangle\,,\ |1\uparrow,2\downarrow,2\uparrow\rangle\,|h\Downarrow\rangle\,,\ |1\downarrow,1\uparrow,2\uparrow\rangle\,|h\Uparrow\rangle\,,\ |1\uparrow,2\downarrow,2\uparrow\rangle\,|h\Uparrow\rangle\}$$

Using Eq. (2.2) and the identities given at the end of Appendix C, the Coulomb matrix elements can be determined in the same manner as before. We then arrive at the following for the doubly-charged exciton Hamiltonian:

$$H^{\mathcal{X}^{2-}} = \begin{bmatrix} E_1^{(\mathcal{X}^{2-})} & V^{(\mathcal{X}^{2-})} & 0 & 0 & 0 & 0 & 0 & 0 \\ V^{(\mathcal{X}^{2-})*} & E_2^{(\mathcal{X}^{2-})} & 0 & 0 & 0 & 0 & 0 & 0 \\ 0 & 0 & E_1^{(\mathcal{X}^{2-})} & V^{(\mathcal{X}^{2-})} & 0 & 0 & 0 & 0 \\ 0 & 0 & V^{(\mathcal{X}^{2-})*} & E_2^{(\mathcal{X}^{2-})} & 0 & 0 & 0 & 0 \\ 0 & 0 & 0 & 0 & E_1^{(\mathcal{X}^{2-})} & V^{(\mathcal{X}^{2-})} & 0 & 0 \\ 0 & 0 & 0 & 0 & V^{(\mathcal{X}^{2-})*} & E_2^{(\mathcal{X}^{2-})} & 0 & 0 \\ 0 & 0 & 0 & 0 & 0 & 0 & E_1^{(\mathcal{X}^{2-})} & V^{(\mathcal{X}^{2-})} \\ 0 & 0 & 0 & 0 & 0 & 0 & V^{(\mathcal{X}^{2-})*} & E_2^{(\mathcal{X}^{2-})} \end{bmatrix}$$

where

$$E_1^{(\mathcal{X}^{2-})} = 2E_1 + E_2 + E_h + E_g + V^{\mathrm{Cou}}_{11,11} + 2V^{\mathrm{Cou}}_{12,21} - V^{\mathrm{Cou}}_{12,12} - 2V^{\mathrm{Cou}}_{1h,h1} - V^{\mathrm{Cou}}_{2h,h2}$$

$$E_2^{(\mathcal{X}^{2-})} = E_1 + 2E_2 + E_h + E_g + V^{\mathrm{Cou}}_{22,22} + 2V^{\mathrm{Cou}}_{12,21} - V^{\mathrm{Cou}}_{12,12} - V^{\mathrm{Cou}}_{1h,h1} - 2V^{\mathrm{Cou}}_{2h,h2}$$

$$V^{(\mathcal{X}^{2-})} = V^{\mathrm{Cou}}_{1h,h2} - V^{\mathrm{Cou}}_{11,12} - V^{\mathrm{Cou}}_{12,22}$$

The matrices $H^{\mathcal{X}^0}$and $H^{\mathcal{X}^{2-}}$ have the same form and differ only in their corresponding matrix elements. Therefore, the energy level structure of a doubly-charged exciton is similar to that of a neutral exciton, i. e., four-fold degenerate and contains an anti-crossing, but is tilted and shifted with repect to the latter due to differences in matrix elements. The energy splitting at the anti-crossing is given by:

$$\Delta_{\mathcal{X}^{2-}} = \sqrt{\left(E_2 - E_1 + V^{\text{Cou}}_{22,22} - V^{\text{Cou}}_{11,11} + V^{\text{Cou}}_{1h,h1} - V^{\text{Cou}}_{2h,h2}\right)^2 + 4\,|V^{(\mathcal{X}^{2-})}|^2}$$

Fig. 2.3 below shows the energy levels for $\mathcal{X}^{2-}$ as a function of applied bias. Here, the heavy-hole wavefunction is localized in the top QD, which has lower energy than the bottom QD. The energy level of the two-electron triplet state, $E_T^{1,2}$, is subtracted from both $\mathcal{X}^{2-}$ levels in order to project the plot in a more convenient way for later discussion on optical transitions. The original energy levels are shown in the inset.

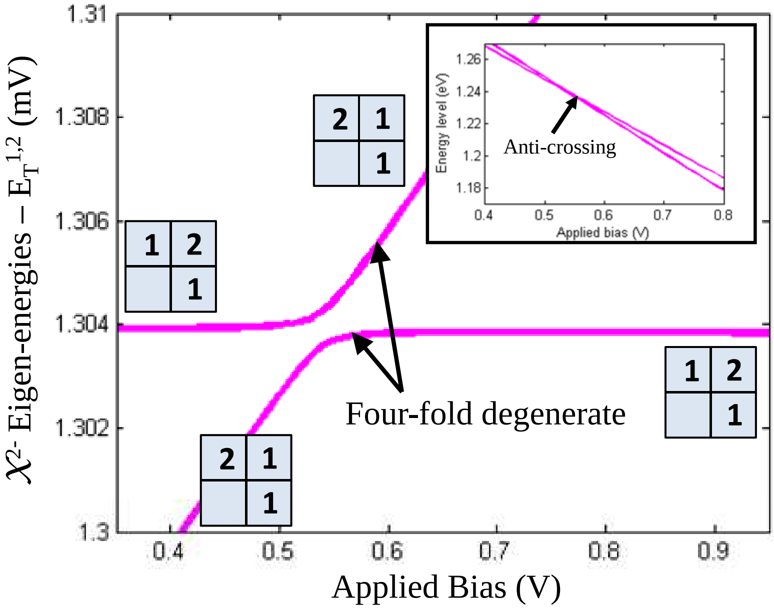

Figure 2.3: Calculated eigen-energies for a doubly-charged exciton, $\mathcal{X}^{2-}$, as a function of applied bias. The energy levels are plotted with $E_T^{1,2}$ as the reference. Window diagrams indicate spatial charge configurations in regions away from the anti-crossing. Inset: Original non-tilted plot.

2.4 Charge stability plateaus and co-tunneling regimes

The examples presented above can be generalized to any charge configuration where the Hamiltonian can be conveniently written in terms of confinement energies and Coulomb matrix elements. Even so, one needs to keep in mind that these quantities are bias dependent. Therefore, different sets of matrix elements need to be numerically evaluated for different applied bias. It was this bias dependency that provides the means to deterministically charge the QDM with a desired number of electrons. This is because by changing bias voltage across the sample, the potential energies of individual QDs relative to the Fermi level can be tuned. The sketch in Fig. 2.4 below illustrates how electrons are added progressively into the QDM when the forward bias is increased.

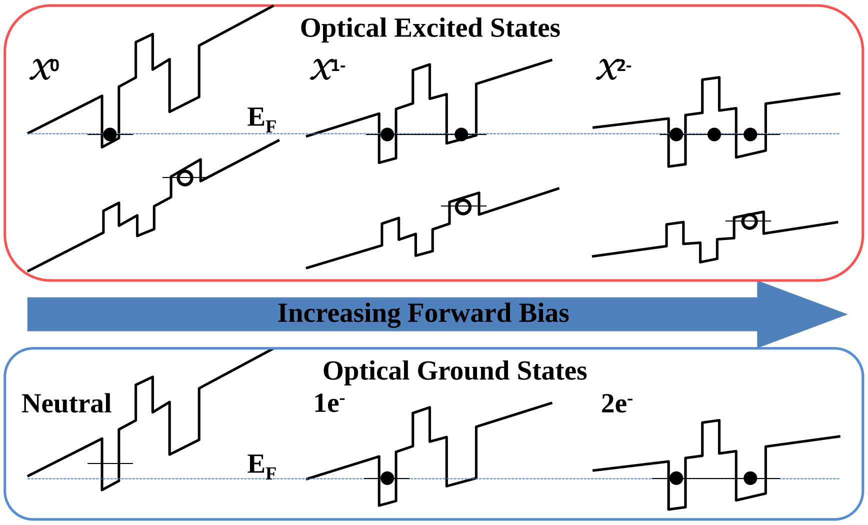

Figure 2.4: Sketches portraying how band diagram changes with applied bias, along with charging sequence. Note that different numbers of electrons as well as charge configurations can exist at a given bias. This figure shows only how the addition of electrons occurs as a function of bias. (Upper panel: optical excited states; Lower panel: optical ground states)

It is important to note that as long as the eigen-energy of a given charge configuration lies below the Fermi level, this configuration can exist. As a result, mutiple charge configurations can be present simultaneously at a given bias. Nonetheless, in most cases, the system will relax to a stable configuration which has the lowest energy level. This configuration can be determined easily by overlaying the calculated eigen-energies of various charge configurations on the same plot, as shown in Fig. 2.5 (a) and (b) for the optical ground state and the optical excited states, respectively. Bias regions where each of these configurations is stable, also known as the charge stability plateaus, are shaded with distinct colors. Near the boundaries of these stability plateaus, two or more charge configurations are energetically degenerate. This means a stable charge configuration is absent in the vicinity of these boundaries, where it is often imagined that an electron rapidly moves in and out of the QDM. Hence, these regions are known as the co-tunneling regimes. As will be seen later in the next chapter, the effects of stability plateaus and co-tunneling regimes are extremely important in the optical characterization and manipulation of the two-electron charge configurations.

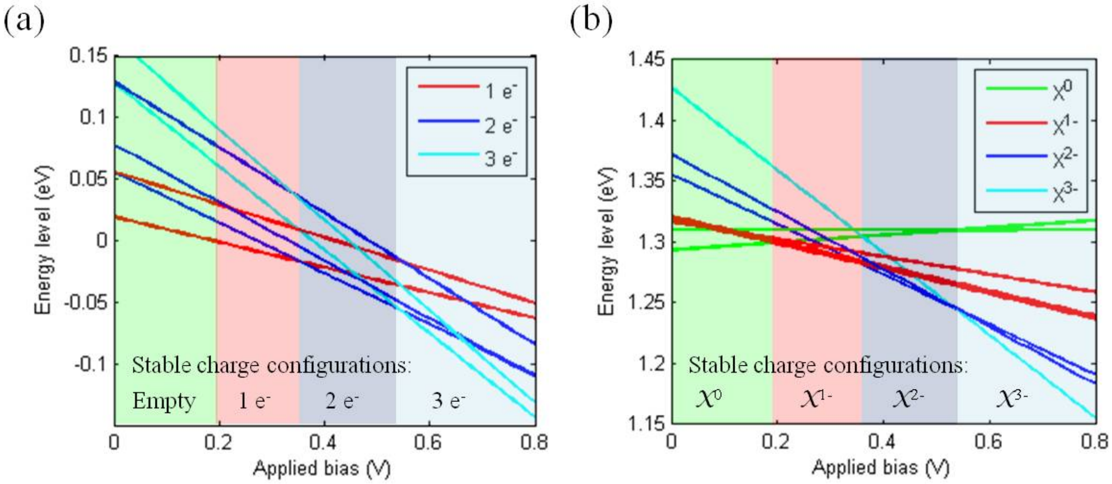

Figure 2.5: Energy level structures of different charge configurations for (a) optical ground states and (b) optical excites states. Regions shaded in green, red, blue and cyan indicate stability plateaus for neutral, $1e^-$, $2e^-$ and $3e^-$ configurations for the optical ground states, and $\mathcal{X}^0$, $\mathcal{X}^{1-}$, $\mathcal{X}^{2-}$ and $\mathcal{X}^{3-}$for the optical excited states, respectively.

Another important feature in Fig. 2.5 is the correspondance between the charging sequence of the optical ground states and their respective optical excited states. In general, the stability plateau of a charge configuration and that of its correponding excitonic states do not necessarily overlap. This is mainly due to the difference in the Coulomb matrix elements associated with the addition of an electron-hole pair. However, as apparent in Fig. 2.5 above, there are considerable overlaps between corresponding ground and optical excited states for the sample under study. This is crucial when it comes to optical manipulations of the electronic states. As will be discussed in following chapters, stable optical ground and excited states are of paramount importance in processes such as optical pumping for electron spin initialization.

2.5 Optical transitions between two-electron states and doubly-charged excitons

Most studies performed on self-assembled semiconductor QDs involve optical excitations. For single QDs, the most fundamental way to distinguish a charged exciton from a neutral one is by measuring the energy splitting (about 6 meV) between two resonances in bias-dependent photoluminescence (PL) spectroscopy. In the case of a

QDM, distinctive features like the anti-crossings produce a variety of structures in PL. Recognizing these complex patterns on a bias-dependent PL map then becomes essential in identifying different charge configurations in a QDM. In order to manage this, one must know the optical dipole allowed transitions between the eigenstates of a charge configuration and their corresponding optical excited states. One of the most important cases in QDMs, as well as the focus of this thesis, is the two electron configuration. For this reason, it is used below as an example showing how dipole allowed transitions can be determined.

A convenient way for deriving the selection rules between two optically coupled manifolds is by considering the symmtry properties of the quantum states involved. In the context of self-assembled InAs QDs, an excellent discussion on the group theoretical derivation of selection rules for QD-confined neutral excitons and trions can be found in Ref. [63]. The approach therein is extended here to the case of a doubly-charged exciton. As a brief summary of this method, consider the matrix element for optical dipole interaction,

$$\langle n| V^{\mathrm{Opt}} |m\rangle ,$$

where $|n\rangle$ and $|m\rangle$, being two eigenstates of the system, possess certain symmetry inherited from the underlying crystal structure. Let us say that $|n\rangle$ and $|m\rangle$ transform according to irreducible representations (*irreps*) $\Gamma_n^{(\mathcal{G})}$ and $\Gamma_m^{(\mathcal{G})}$ of space group $\mathcal{G}$. In general, the operator V^{Opt} can be written in terms of *irreducible tensor operators* $V_j^{(\mathcal{G})}$, which transforms according to the *irrep* $\Gamma_j^{(\mathcal{G})}$. The operation of V^{Opt} on $|m\rangle$ results in a state vector that transforms in the same way as the product representation

$$\sum_j p_j \Gamma_j^{(\mathcal{G})} \times \Gamma_m^{(\mathcal{G})}$$

which is in general reducible and has the irreducible decomposition

$$\sum_j p_j \Gamma_j^{(\mathcal{G})} \times \Gamma_m^{(\mathcal{G})} = \sum_k q_k \Gamma_k^{(\mathcal{G})} \tag{2.8}$$

The matrix element $\langle n| V^{\mathrm{Opt}} |m\rangle$ is nonzero only if the right hand side of Eq. (2.8) contains $\Gamma_n^{(\mathcal{G})}$.

A self assembled InAs QD has a point group symmetry of C_{2v}. The reduction of symmetry from the bulk InAs space group, which is cubic T_d^2, is due to strain and anisotropy developed during the growth process[64, 63]. There are four single valued and one double valued *irreps* for the symmetry group C_{2v}, denoted by Γ_1, Γ_2, Γ_3, Γ_4 and Γ_5, respectively. The character table for these representations is given below, along with their irreducible decompositions. In most optical excitation schemes, the beam travels along z-direction and the electric field vector is pointing in the transverse direction. For x-polarized electric field, the corresponding irreducible tensor operator transforms according to Γ_3, while y-polarized field corresponds to the *irrep* Γ_4.

C_{2v}	Basis	E	$\bar{E}$	C_2	σ_y	σ_x
				$\bar{C}_2$	$\bar{\sigma}_y$	$\bar{\sigma}_x$
Γ_1	z, x^2, y^2, z^2	1		1	1	1
Γ_2	xy	1		1	-1	-1
Γ_3	x, xz	1		-1	1	-1
Γ_4	y, yz	1		-1	-1	1
Γ_5	$\left\{+\frac{1}{2}, -\frac{1}{2}\right\}$	2	-2	0	0	0

$$\begin{aligned}
&\Gamma_1 \times \Gamma_i = \Gamma_i\\
&\Gamma_i \times \Gamma_i = \Gamma_1\\
&\Gamma_2 \times \Gamma_3 = \Gamma_4\\
&\Gamma_2 \times \Gamma_4 = \Gamma_3\\
&\Gamma_3 \times \Gamma_4 = \Gamma_2\\
&\Gamma_5 \times \Gamma_i = \Gamma_5,\ i \neq 5\\
&\Gamma_5 \times \Gamma_5 = \Gamma_1 + \Gamma_2 + \Gamma_3 + \Gamma_4
\end{aligned}$$

Table 2.1: Character table and irreducible decompositions for C_{2v} point group. σ_y represents mirror reflection in the xz-plane, while σ_x in the yz-plane.

To proceed, we need to determine the *irreps* according to which the eigenstates involved transform. Let us rewrite the two-electron optical ground states in Eq. (2.5) in another basis:

$$\begin{aligned}
\left|\gamma_1^{1,1}\right\rangle &= \left|S^{1,1}\right\rangle\\
\left|\gamma_1^{2,2}\right\rangle &= \left|S^{2,2}\right\rangle\\
\left|\gamma_2^{1,2}\right\rangle &= \left|S^{1,2}\right\rangle\\
\left|\gamma_1^{1,2}\right\rangle &= \left|T_0^{1,2}\right\rangle\\
\left|\gamma_3^{1,2}\right\rangle &= \tfrac{1}{\sqrt{2}}\left(\left|T_+^{1,2}\right\rangle - \left|T_-^{1,2}\right\rangle\right)\\
\left|\gamma_4^{1,2}\right\rangle &= \tfrac{1}{\sqrt{2}}\left(\left|T_+^{1,2}\right\rangle + \left|T_-^{1,2}\right\rangle\right)
\end{aligned} \tag{2.9}$$

It is easy to see that the singlet states $\left|\gamma_1^{1,1}\right\rangle$ and $\left|\gamma_1^{2,2}\right\rangle$ transform like Γ_1, while the spin triplets $\left|\gamma_1^{1,2}\right\rangle$, $\left|\gamma_3^{1,2}\right\rangle$ and $\left|\gamma_4^{1,2}\right\rangle$, which behave like the p_z, p_x and p_y orbitals, transform according to Γ_1, Γ_3 and Γ_4, respectively. The remaining singlet $\left|\gamma_2^{1,2}\right\rangle$ transforms according to either Γ_1 or Γ_2, depending on the details of the spatial wavefunctions. Here it is assumed to transform like Γ_2, but in the absence of magnetic field, the outcome remains the same if Γ_1 is used instead. For the $\mathcal{X}^{2-}$ configuration, each eigenstate contains two spin-paired electrons and a neutral exciton, and thus transforms like the product state $\Gamma_1 \times \Gamma_i = \Gamma_i$ where $i \neq 5$. Similar to the two-electron ground states, we can express the optical excited states in a symmetry adapted basis and classify them according to their *irreps*:

$$\begin{aligned}
\Gamma_1 : &\quad \left\{ \begin{array}{l} \left|\boldsymbol{\xi}_1^{1,h}\right\rangle = \frac{1}{\sqrt{2}}\left(|1\uparrow,2\downarrow,2\uparrow\rangle\,|h\Uparrow\rangle + |1\downarrow,2\downarrow,2\uparrow\rangle\,|h\Downarrow\rangle\right) \\ \left|\boldsymbol{\xi}_1^{2,h}\right\rangle = \frac{1}{\sqrt{2}}\left(|1\downarrow,1\uparrow,2\uparrow\rangle\,|h\Uparrow\rangle + |1\downarrow,1\uparrow,2\downarrow\rangle\,|h\Downarrow\rangle\right) \end{array} \right. \\
\Gamma_2 : &\quad \left\{ \begin{array}{l} \left|\boldsymbol{\xi}_2^{1,h}\right\rangle = \frac{1}{\sqrt{2}}\left(|1\uparrow,2\downarrow,2\uparrow\rangle\,|h\Uparrow\rangle - |1\downarrow,2\downarrow,2\uparrow\rangle\,|h\Downarrow\rangle\right) \\ \left|\boldsymbol{\xi}_2^{2,h}\right\rangle = \frac{1}{\sqrt{2}}\left(|1\downarrow,1\uparrow,2\uparrow\rangle\,|h\Uparrow\rangle - |1\downarrow,1\uparrow,2\downarrow\rangle\,|h\Downarrow\rangle\right) \end{array} \right. \\
\Gamma_3 : &\quad \left\{ \begin{array}{l} \left|\boldsymbol{\xi}_3^{1,h}\right\rangle = \frac{1}{\sqrt{2}}\left(|1\downarrow,2\downarrow,2\uparrow\rangle\,|h\Uparrow\rangle - |1\uparrow,2\downarrow,2\uparrow\rangle\,|h\Downarrow\rangle\right) \\ \left|\boldsymbol{\xi}_3^{2,h}\right\rangle = \frac{1}{\sqrt{2}}\left(|1\downarrow,1\uparrow,2\downarrow\rangle\,|h\Uparrow\rangle - |1\downarrow,1\uparrow,2\uparrow\rangle\,|h\Downarrow\rangle\right) \end{array} \right. \\
\Gamma_4 : &\quad \left\{ \begin{array}{l} \left|\boldsymbol{\xi}_4^{1,h}\right\rangle = \frac{1}{\sqrt{2}}\left(|1\downarrow,2\downarrow,2\uparrow\rangle\,|h\Uparrow\rangle + |1\uparrow,2\downarrow,2\uparrow\rangle\,|h\Downarrow\rangle\right) \\ \left|\boldsymbol{\xi}_4^{2,h}\right\rangle = \frac{1}{\sqrt{2}}\left(|1\downarrow,1\uparrow,2\downarrow\rangle\,|h\Uparrow\rangle + |1\downarrow,1\uparrow,2\uparrow\rangle\,|h\Downarrow\rangle\right) \end{array} \right.
\end{aligned} \tag{2.10}$$

The result above directly follows the assignment of *irreps* to the two-electron states in Eq. (2.9). To see this, one must keep in mind that a spin-up hole transforms in the same manner as a spin-down electron, and vice versa. The fact that the basis states $\left|\boldsymbol{\xi}_1^{1,h}\right\rangle$, $\left|\boldsymbol{\xi}_2^{1,h}\right\rangle$, $\left|\boldsymbol{\xi}_3^{1,h}\right\rangle$ and $\left|\boldsymbol{\xi}_4^{1,h}\right\rangle$ all belong to different *irreps* tells us that, unlike what was shown in Fig. 2.3, they are not necessarily degenerate. In reality, there is a small energy difference between $\left|\boldsymbol{\xi}_3^{1,h}\right\rangle$ and $\left|\boldsymbol{\xi}_4^{1,h}\right\rangle$, known as the exciton hyperfine or electron-hole exchange splitting. In order to keep our discussion here simple, this splitting is ignored.

From the symmetry of the basis states and the irreducible tensor operators, optical dipole allowed transitions can be easily determined. For example, since $\Gamma_1 \times \Gamma_3 = \Gamma_3$, the x-polarized light couples $\left|\boldsymbol{\gamma}_1^{1,1}\right\rangle$, $\left|\boldsymbol{\gamma}_1^{2,2}\right\rangle$ and $\left|\boldsymbol{\gamma}_1^{1,2}\right\rangle$ with the optical excited states $\left|\boldsymbol{\xi}_3^{1,h}\right\rangle$ and $\left|\boldsymbol{\xi}_3^{2,h}\right\rangle$. Likewise, from $\Gamma_1 \times \Gamma_4 = \Gamma_4$, transitions between $\left|\boldsymbol{\xi}_4^{1,h}\right\rangle$ and $\left|\boldsymbol{\xi}_4^{2,h}\right\rangle$ and the aforementioned optical ground states are allowed under y-polarized excitation. Fig. 2.6 above shows all dipole allowed transitions between the two-electron optical ground states and the excited states $\left|\boldsymbol{\xi}_1^{1,h}\right\rangle$, $\left|\boldsymbol{\xi}_2^{1,h}\right\rangle$, $\left|\boldsymbol{\xi}_3^{1,h}\right\rangle$ and $\left|\boldsymbol{\xi}_4^{1,h}\right\rangle$. For the remaining half of the excited states, similar selection rules are obtained.

The optical transitions between two-electron states and $\mathcal{X}^{2-}$ can be identified in bias-dependent PL spectra by virtue of the distinctive pattern of the resonant energies. In PL, a laser beam with higher frequency than the optical resonances is used to excite charge carriers into higher-lying energy levels. These charges then relax to different $\mathcal{X}^{2-}$ states through various non-radiative pathways. When an electron-hole pair recombines, leaving two electrons in either singlet or triplet states, a photon

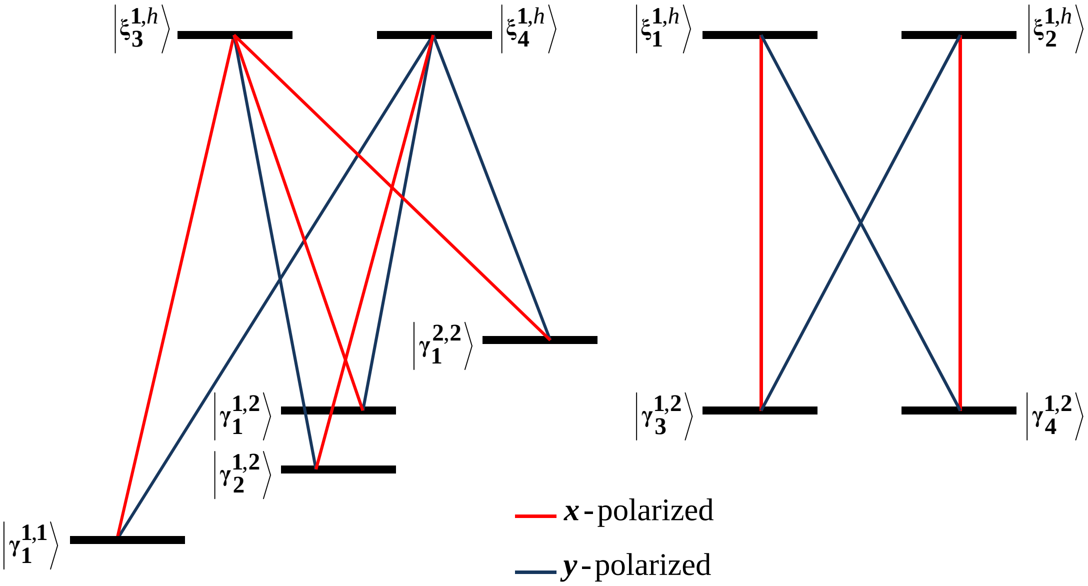

Figure 2.6: Selection rules for optical transitions between the two-electron optical ground states and the excited states $\left|\boldsymbol{\xi}_1^{1,h}\right\rangle$, $\left|\boldsymbol{\xi}_2^{1,h}\right\rangle$, $\left|\boldsymbol{\xi}_3^{1,h}\right\rangle$ and $\left|\boldsymbol{\xi}_4^{1,h}\right\rangle$. For the selection rules involving $\left|\boldsymbol{\xi}_1^{2,h}\right\rangle$, $\left|\boldsymbol{\xi}_2^{2,h}\right\rangle$, $\left|\boldsymbol{\xi}_3^{2,h}\right\rangle$ and $\left|\boldsymbol{\xi}_4^{2,h}\right\rangle$, simply replace superscripts "1" in the label for the excited states by "2".

with frequency corresponding to the energy difference between the excited and ground states is created. A PL map is generated by measuring the resonant frequencies at different applied bias, as shown in Fig. 2.7(c), which was measured with a QDM named QDM-A.

To understand the complex spectra observed, consider the energy level structures of the two-electron states in Fig. 2.2 and that of the $\mathcal{X}^{2-}$ configuration in Fig. 2.3, reproduced in Fig. 2.7(a) above, where both contain an anti-crossing. Here the energy level of $\left|\gamma_1^{2,2}\right\rangle$ lies outside the plot range. From the selection rules shown in Fig. 2.6, there are 10 allowed optical transitions for each x- and y-polarization between the 5 ground states and the 8 excited states shown. Four of them are indicated by vertical arrows, which correspond to transitions between the singlets, $\left|\gamma_1^{1,1}\right\rangle$ and $\left|\gamma_1^{1,2}\right\rangle$, and the excited states $\left|\boldsymbol{\xi}_3^{1,h}\right\rangle$, $\left|\boldsymbol{\xi}_4^{1,h}\right\rangle$, $\left|\boldsymbol{\xi}_3^{2,h}\right\rangle$ and $\left|\boldsymbol{\xi}_4^{2,h}\right\rangle$. Due to the Coulomb matrix elements associated with the addition of an electron-hole pair, the anti-crossing of the $\mathcal{X}^{2-}$ configuration is shifted with respect to that of the two-electron states. The resulting resonant energy structure in Fig. 2.7(b) contains four anti-crossings, where two of which to the left arise from that of $\mathcal{X}^{2-}$, while the other two to the right are from the singlet anti-crossing of the two-electron states. The four transitions labeled in Fig. 2.7(a) give rise to the large Stark shift lines forming an "X-pattern" at the center of Fig. 2.7(b). These lines are known as the indirect transitions because they can be loosely interpreted as the result of the recombination between an electron and a hole localized in separate QDs.

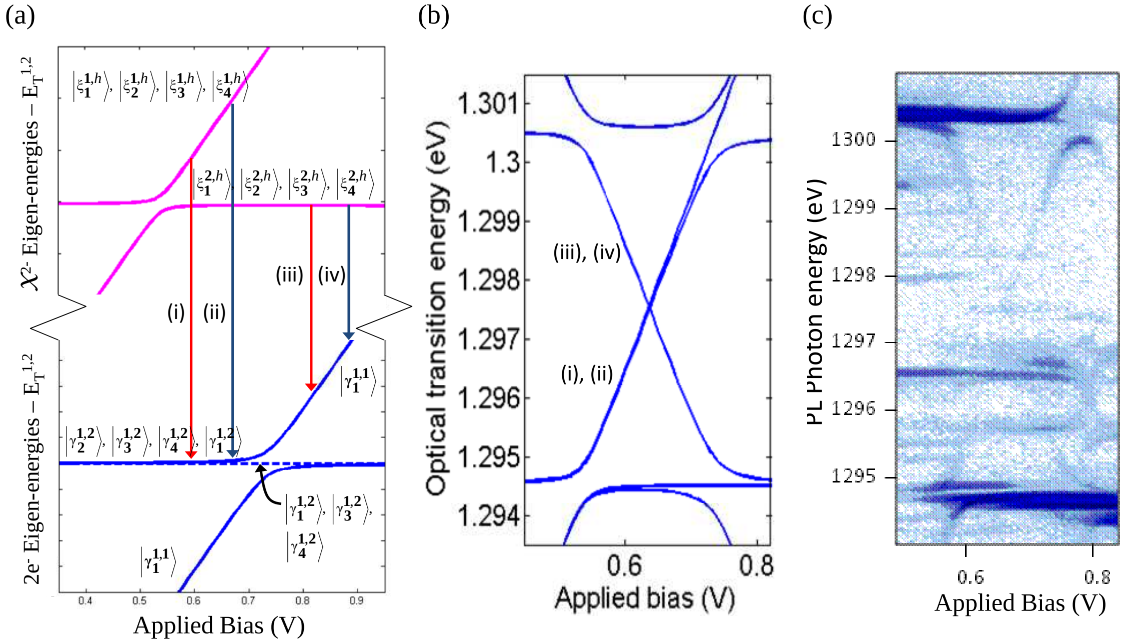

Figure 2.7: (a) Optical transitions between the $\mathcal{X}^{2-}$ configuration and the two-electron states. Note that only 4 out of 20 possible transitions are labeled. Red arrows represent x-polarized optical transitions, while blue arrows denote y-polarization. (b) Resulting resonant energy structure showing the characteristic "X-pattern". (c) PL map of a QDM (QDM-A). The energy of the CW excitation laser is 1.38 eV (900 nm).

2.6 Remarks on neutral exciton and trion transitions, conclusion and outlook

At the end of the preceding section, the theoretical model is shown to successfully reproduce the essential features of the complex structure observed PL. Although the discussion here is confined to the two-electron states and the doubly-charged exciton, similar modeling procedure can be extended to the other charge configurations with minimal incremental efforts. Since the Coulomb matrix elements numerically evaluated for the $\mathcal{X}^{2-}$ case can be reused for all other charge configurations, the task of calculating their eigen-energies.reduces to merely diagonalizing the Hamiltonians associated with these charge configurations. Furthermore, selection rules for optical transitions are readily available thanks to previous works on neutral excitons and trions in single QDs, as reported in Ref. [63]. To see how they are related to those in a QDM, consider the irreducible decompositions shown below (assuming that electrons occupy only the two lowest-lying energy levels):

Configuration	*Irreps* of electrons	*Irrep* of hole	Irreducible decomposition
$1e^-$	Γ_5	–	Γ_5
$3e^-$	$\Gamma_1 \times \Gamma_5 = \Gamma_5$	–	Γ_5
$\mathcal{X}^0$	Γ_5	Γ_5	$\Gamma_5 \times \Gamma_5 = \Gamma_1 + \Gamma_2 + \Gamma_3 + \Gamma_4$
$\mathcal{X}^{1-}$	$\Gamma_1, \Gamma_2, \Gamma_3, \Gamma_4$	Γ_5	$\Gamma_i \times \Gamma_5 = \Gamma_5$, $i \neq 5$
$\mathcal{X}^{3-}$	Γ_1	Γ_5	$\Gamma_1 \times \Gamma_5 = \Gamma_5$

The list above shows that the optical transitions between the single-electron and three-electron configurations and their respective optical excited states transform like that of a trion in single QDs. An example of calculated optical resonance map that includes $\mathcal{X}^0$, $\mathcal{X}^{1-}$ and $\mathcal{X}^{3-}$ related transitions, in addition to those of $\mathcal{X}^{2-}$, is shown in Fig. 2.8. Here, the inter-QD spacing and QD sizes are different from those used in previous calculations, and the hole is confined to the top QD. The two "X-patterns" in the bias-dependent spectra arise from the $\mathcal{X}^{1-}$-single electron transitions (left) and from the $\mathcal{X}^{2-}$-two-electron transitions (right) discussed earlier. It is interesting to note that the result qualitatively reproduces the essential features of the PL map found in Ref. [9].

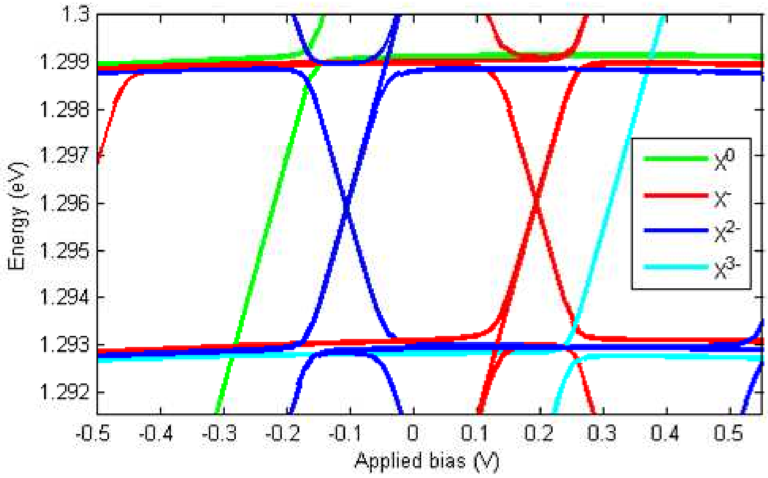

Figure 2.8: Numerically calculated bias dependent optical resonances for $\mathcal{X}^0$-neutral QDM, $\mathcal{X}^{1-}$-single electron, $\mathcal{X}^{2-}$-two-electron, and $\mathcal{X}^{3-}$-three-electron transitions. For the purpose of showing the double X-patterns, the inter-QD spacing and QD sizes used here are different from those in previous calculations.

In contrast to the phenomenological, piecewise methods commonly used in the literatures[38, 9, 42, 27, 65, 39, 40, 41, 10, 36], the model presented in this and the previous chapters provides a more holistic picture of the electronic and optical properties of a QDM. From this model, one could gain insights into the physical origins of certain ad hoc parameters employed in other literatures, such as the tunneling constant, kinetic exchange and electron-hole exchange. On the one hand, the model is developed here for the purpose of understanding the essential physics of a QDM, and subsequently for assistance in identifying different optical transitions in PL spectra. On the other hand, this "bottom-up" approach offers a systematic way to study the effects of physical parameters such as strain or inter-QD distance on the electronic properties of a QDM. This potentially serves as an invaluable tool for the design and implementation of QDMs for applications in quantum information processing. Meanwhile, for the purpose in this thesis, the model provides guidance in choosing a suitable sample bias for further study, as will be discussed in the next chapter.

CHAPTER III

Optical Pumping in the Two-Electron Configuration: Electron Spin Preparation in Zero and Nonzero External Magnetic Fields

The preceding chapter emphasized the importance of the two-electron configuration as a test-bed for many aspects of quantum mechanics, and as a platform to investigate the electronic and optical properties of QDMs. For applications in quantum information processing, the study of the two-electron manifold is motivated by the prospect in scaling up a single QD electron spin qubit to two-qubit operations in a QDM. Using the energy level structure shown previously, the identification of the singlet-triplet states of the two-electron configuration via optical pumping is explained in this chapter. The characterization of QDMs for two-qubit operations requires the knowledge of optical selection rules in magnetic fields, which will also be derived here. The result is an eight-level system that serves as the model for all further studies reported in this thesis.

One of the five DiVincenzo criteria[6] stipulates that for quantum computation, one must be able to initialize the qubits to a known state. A convenient way to achieve this is by emulating earlier success in single self-assembled QDs, where the samples are placed in magnetic fields, and the electron spins are initialized via optical cooling[15, 13]. Later in this chapter, it is shown how initialization of two-electron spin states is accomplished in a similar manner with an applied magnetic field in Voigt geometry, but with multiple pump lasers. The results give us a brief introduction to the effects of nuclear environment on the lineshapes of optical resonances, which will be the focus of the next chapter.

3.1 The "sweet spot" for two electron spin manipulation

One of the objectives of the analyses in preceding chapters is to assist in identifying a suitable voltage bias for two-qubit operations. In Chapter 2, we have seen that the two-electron states can be written in singlet-triplet basis: $|S^{1,1}\rangle$, $|S^{2,2}\rangle$, $|S^{1,2}\rangle$, $|T_{-}^{1,2}\rangle$, $|T_{0}^{1,2}\rangle$ and $|T_{+}^{1,2}\rangle$, where the subscripts denote spin projections while superscripts charge configurations. If we ignore the off-diagonal terms in Eq. (2.6), the Hamiltonian for the four-dimensional subspace, $\mathfrak{S}^{1,2}$, spanned by the basis states $\{|S^{1,2}\rangle, |T_{-}^{1,2}\rangle, |T_{0}^{1,2}\rangle, |T_{+}^{1,2}\rangle\}$ can be written as

$$H_{2e^-}^{(1,2)} = -\frac{V_{12,12}^{\mathrm{Cou}}}{\hbar^2} \sum_{\alpha,\beta,\gamma,\delta} \hat{S}_{\alpha\beta,\gamma\delta}^{(2)} \hat{a}^{\dagger}(\alpha)\, \hat{a}^{\dagger}(\beta)\, \hat{a}(\gamma)\, \hat{a}(\delta) + \frac{1}{2} E_{ST} \sum_{\alpha} \hat{a}^{\dagger}(\alpha)\, \hat{a}(\alpha) \tag{3.1}$$

where the spin operator $\hat{S}_{\alpha\beta,\gamma\delta}^{(2)}$ is defined as

$$\hat{S}_{\alpha\beta,\gamma\delta}^{(2)} = \langle\alpha| \otimes \langle\beta|\, \hat{\mathbf{S}}_{\gamma} \cdot \hat{\mathbf{S}}_{\delta}\, |\gamma\rangle \otimes |\delta\rangle\,, \ \hat{\mathbf{S}}_{\gamma} \text{ and } \hat{\mathbf{S}}_{\delta} \text{ are single-spin operators, and}$$

$$E_{ST} = E_1 + E_2 + V_{12,21}^{\mathrm{Cou}} - \frac{1}{2} V_{12,12}^{\mathrm{Cou}}$$

The first term in Eq. (3.1) is known as the Heisenberg exchange Hamiltonian which gives rise to the energy splitting of $2V_{12,12}^{\mathrm{Cou}}$ between the singlet and triplet states, while the second term is merely a common energy shift.

It is apparent that the Heisenberg exchange term gives the basic mechanism for the interaction between electron spins neccesary for two-qubit operations. Hence, it is desirable that the subspace $\mathfrak{S}^{1,2}$ becomes isolated from the other two singlet states, or, $V_{11,12}^{\mathrm{Cou}}$, $V_{12,22}^{\mathrm{Cou}} \ll V_{12,12}^{\mathrm{Cou}}$. From Chapter 2, we know that this occurs in regions away from the anti-crossing. For convenience, the bias dependent optical transitions from Chapter 2 is reproduced in Fig. 3.1 below.

While the operation point in bias should be chosen as far away from the anti-crossing as possible, it is necessary to keep the singlet-triplet splitting at least several linewidths of the optical resonance. This is to ensure that all resonances can be resolved when an external magnetic field is applied so that the individual states can be optically manipulated without significant coupling the other states, causing unintended dynamics. Ideally, the singlet and triplet transitions should have zero DC Stark shift so that the resonant frequencies remain unaffected by fluctuations in the applied voltage. More importantly, at the operation point, the basis states spanning subspace $\mathfrak{S}^{1,2}$ should belong to the lowest energy charge configuration in

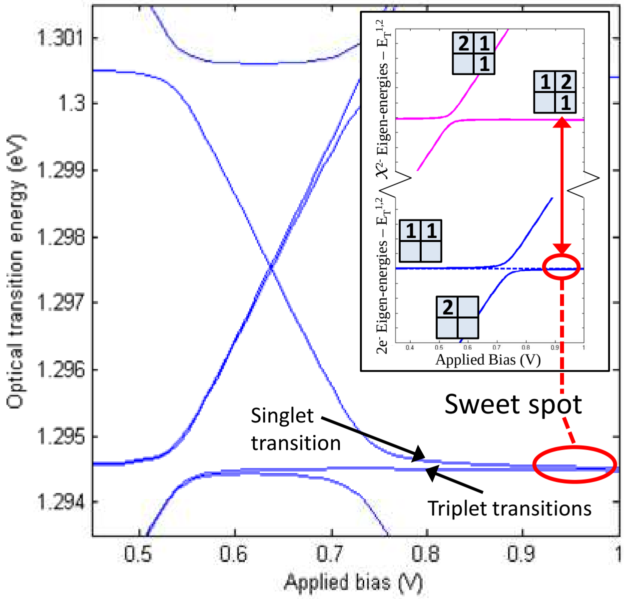

Figure 3.1: $\mathcal{X}^{2-}$-two-electron optical transition energies versus bias reproduced from Chapter 2. The energy levels for two-electron and $\mathcal{X}^{2-}$ configurations are shown in the inset, where window diagrams indicate charge configurations away from the anti-crossings. The sweet spot, marked by the red circle in the transition map, corresponds to the recombination of an electron-hole pair localized in the top QD, leaving behind two localized electrons, as indicated by the two-sided arrow. The singlet and triplet transitions are also marked.

order to remain as stable optical ground states of the system. The bias voltage that meets all the requirements above is called the "sweet spot". At the sweet spot, the wavefunctions are sufficiently localized so that the two electrons presumably reside in seperate QDs. However, in order to maintain a nonzero singlet-triplet splitting, a small amount of wavefunction overlap must remain. As can be seen in the inset of Fig. 3.1, in the $\mathcal{X}^{2-}$ manifold, the separation in bias between the sweet spot and the anti-crossing of the $\mathcal{X}^{2-}$ states is even larger than that between the sweet spot and the two-electron anti-crossing. This far away from the anti-crossing, tunneling between the two QDs is negligible. Therefore, the optical excited states here can be regarded as consisting of an isolated electron in the bottom QD and a trion in the top QD.

A sweet spot is optically addressable only if it lies within the stability plateau of both the two-electron and the $\mathcal{X}^{2-}$configurations. Due to the inhomogeneity of the QDMs across the sample, in practice, an extensive search is normally needed before an optically active singlet-triplet system is found. In bias dependent photoluminescence spectra, here known as PL maps, the singlet-triplet transitions around the sweet spot are signified by two near parallel resonances, as indicated in Fig. 3.2(a) and (b) for two different QDMs named QDM-B and QDM-C, respectively, found at different locations on the sample. Note that due to the high density of QDMs on the sample, many QDMs are illuminated by the 1 μm-diameter excitation beam simultaneously. The well-defined $\mathcal{X}^{2-}$ charge stability plateaus manifest in the disappearence of the singlet and triplet transitions outside of the circled regions in both PL maps.

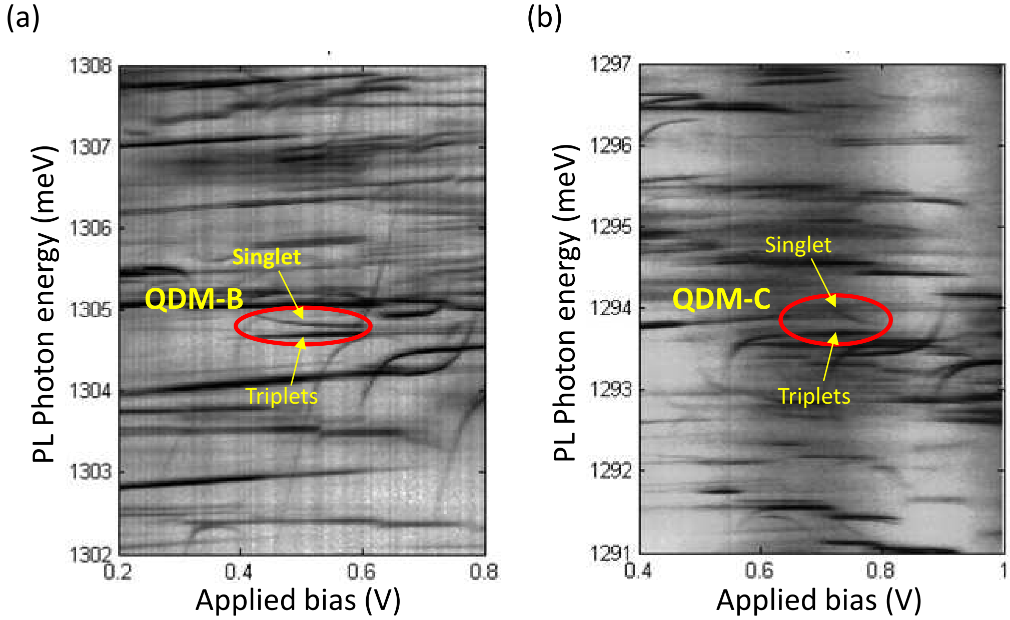

Figure 3.2: PL maps for multiple QDMs illuminated simultaneously with an excitation laser at 1.38 eV (900 nm). Two QDMs with two-electron stablility plateaus near the sweet spot are identified, marked by red circles in (a) and (b) for QDM-B and QDM-C, respectively. The singlet and triplet transitions for each QDM are also indicated.

3.2 Optical pumping and state preparation of a singlet-triplet qubit in zero magnetic field

The singlet and triplet resonances for both QDMs in Fig. 3.2 arise from the optical transitions between the basis states of subspace $\mathfrak{S}^{1,2}$, defined in § 3.1, and the manifold $\left\{\xi_i^{2,h}\right\}$, given in Eq. (2.10), where $i = 1, 2, 3, 4$. As pointed out in Chapter 2, in regions far away from the anti-crossings, the spatial basis provides a somewhat accurate picture of the quantum states in a QDM (see § 2.1). Thus, in the vicinity of the sweet spot, the manifold $\left\{\xi_i^{2,h}\right\}$ presumably consists of four spin states of the configuration $\begin{pmatrix} 1,2 \\ 0,1 \end{pmatrix}$, where an electron occupies a localized state in the bottom QD while a trion is formed in the top QD. Here, the basis for the subspace $\mathfrak{S}^{1,2}$ and the optical excited states, $\xi_i^{2,h}$, are more conveniently rewritten as:

$$\begin{gathered}
\text{Optical ground states :}\\
\tfrac{1}{\sqrt{2}}\left(\left|\downarrow\right\rangle\left|\uparrow\right\rangle - \left|\uparrow\right\rangle\left|\downarrow\right\rangle\right) \equiv \left|S^{1,2}\right\rangle\\
\tfrac{1}{\sqrt{2}}\left(\left|\downarrow\right\rangle\left|\uparrow\right\rangle + \left|\uparrow\right\rangle\left|\downarrow\right\rangle\right) \equiv \left|T_0^{1,2}\right\rangle\\
\left|\downarrow\right\rangle\left|\downarrow\right\rangle \equiv \left|T_-^{1,2}\right\rangle\\
\left|\uparrow\right\rangle\left|\uparrow\right\rangle \equiv \left|T_+^{1,2}\right\rangle
\end{gathered} \tag{3.2}$$

$$\begin{gathered}
\text{Optical excited states :}\\
\left|\downarrow\right\rangle\left|t_\Downarrow\right\rangle \equiv \left|1\downarrow, 1\uparrow, 2\downarrow\right\rangle\left|h\Downarrow\right\rangle\\
\left|\downarrow\right\rangle\left|t_\Uparrow\right\rangle \equiv \left|1\downarrow, 1\uparrow, 2\downarrow\right\rangle\left|h\Uparrow\right\rangle\\
\left|\uparrow\right\rangle\left|t_\Downarrow\right\rangle \equiv \left|1\downarrow, 1\uparrow, 2\uparrow\right\rangle\left|h\Downarrow\right\rangle\\
\left|\uparrow\right\rangle\left|t_\Uparrow\right\rangle \equiv \left|1\downarrow, 1\uparrow, 2\uparrow\right\rangle\left|h\Uparrow\right\rangle
\end{gathered} \tag{3.3}$$

In the notation of the product states above, the "ket" to the left represents a quantum state predominantly confined to the bottom QD, while the one to the right the top QD. $\left|t_\Downarrow\right\rangle$ and $\left|t_\Uparrow\right\rangle$ denote trion states with spin-down and spin-up heavy-holes, respectively, in $+z$-direction, here known as the spin-down and spin-up trions.

Since the quantum states are treated as those localized within single QDs, the selection rules for dipole allowed optical transitions can be readily inferred from those of single QDs[13, 63, 66]. For circularly polarized optical fields in a single QD, a spin-down electron, $\left|\downarrow\right\rangle$, and a spin-down trion, $\left|t_\Downarrow\right\rangle$, are coupled by σ_--polarized light, while σ_+-polarized light.couples a spin-up electron, $\left|\uparrow\right\rangle$, and a spin-up trion, $\left|t_\Uparrow\right\rangle$. The optical transition matrix elements vanish for all other combinations. From this and the assumption that the applied optical field does not effect the bottom QD electron due to detuning, we arrive at the selection rules between the two-electron subspace $\mathfrak{S}^{1,2}$ and the optical excited states as shown in Fig. 3.3 below. It is important to note that by using the definitions

$$\sigma_+ = \frac{\hat{x} + i\hat{y}}{\sqrt{2}} \quad \text{and} \quad \sigma_- = -\frac{\hat{x} - i\hat{y}}{\sqrt{2}} \tag{3.4}$$

one recovers the selection rules shown in Fig. 2.6 in the basis of $\left\{\gamma_i^{1,2}\right\}$ and $\left\{\xi_j^{2,h}\right\}$

following Eq. (2.9) and (2.10), where $i, j = 1, 2, 3, 4$.

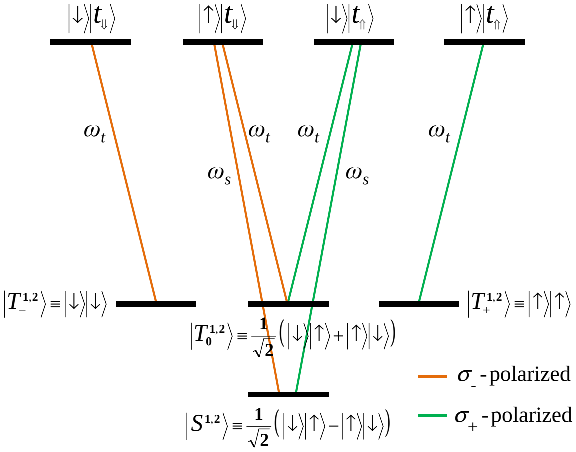

Figure 3.3: Selection rules for the two-electron subspace $\mathfrak{S}^{1,2}$ with circularly polarized light and zero applied magnetic field. ω_s and ω_t denote resonant frequencies of the singlet and triplet transitions, respectively.

Fig. 3.3 shows that the two-electron states $|S^{1,2}\rangle$ and $\left|T_0^{1,2}\right\rangle$ form two Λ-systems with the excited states $|\downarrow\rangle\,|t_\Uparrow\rangle$ and $|\uparrow\rangle\,|t_\Downarrow\rangle$. When a probe laser resonant with, say, the singlet transition is incident on the QDM, the population in the singlet state is being excited to one of the optical excited states, from where the population then spontaneously decays to either the triplet state $\left|T_0^{1,2}\right\rangle$, or back to the singlet state. If the rate of optical excitation is larger then the total rate of population relaxation back to the singlet state, the initial population in the singlet state will be depleted when a steady state is reached. As a result, the two-electron spin is prepared in the triplet manifold and this process is known as the optical pumping. In single QDs, this method is used to initialize the electron spin state in conjunction with the application of an external magnetic field which lifts the spin degeneracy[13, 15]. In QDMs, however, due to the presence of singlet-triplet splitting, optical pumping occurs without an applied magnetic field[7, 67, 8].

The effects of optical pumping are revealed in the bias dependent single laser absorption spectra, known here as the absorption map, as shown in Fig. 3.4(a) for QDM-B. Within the stability plateau of the singlet-triplet optical ground states, the probe laser on resonance with the singlet state pumps the population to the triplet, and vice versa, resulting in a loss of the absorption signal. At the co-tunneling regimes, however, instability of the two-electron configuration causes rapid spin relaxation and population redistribution among the optical ground states. This compromises the optical pumping process and allows the absorption signals to be observed for both singlet and triplet transitions. The resulting “absorption gaps” between the co-tunneling regimes are hallmarks of optical pumping and serve as additional tools for the identification of the singlet-triplet states without an applied magnetic field. When a strong pump laser on resonance with the other leg of the Λ-system is applied, as shown in Fig. 3.4(c) and (e), the effects of optical pumping are reversed. Here, the process of optical re-pump induced by the pump laser recovers the probe absorption signals within the stability plateau, as shown in Fig. 3.4(b) and (d) for the singlet and triplet transitions, respectively.

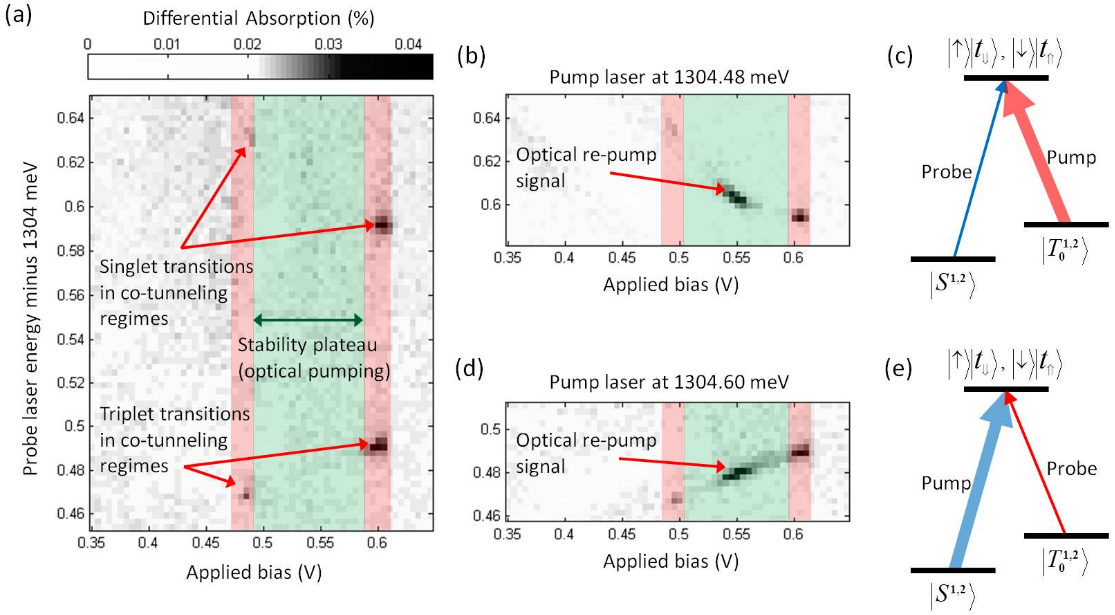

Figure 3.4: Absorption maps of QDM-B showing the effects of optical pumping and re-pump. (a) Differential absorption of the probe laser is diminished in the stability plateau of the singlet-triplet optical ground states, indicated by the green shaded region. Red shaded areas centered at 0.48 V and 0.6 V are co-tunneling regimes. (b) The absorption signal for the singlet transition within the stability plateau is restored by the application of a pump laser on resonance with the triplet transition, as shown in the energy level diagram in (c). (d) Recovery of triplet absorption signal within the stability plateau following the optical pumping scheme as shown in (e). Similar effects of optical pumping and re-pump are observed in QDM-C.

It is important to point out that according to the selection rules in Fig. 3.3, the triplet states, $|T_-^{1,2}\rangle$ and $|T_+^{1,2}\rangle$, and their corresponding optical excited states, $|\downarrow\rangle\,|t_{\Downarrow}\rangle$ and $|\uparrow\rangle\,|t_{\Uparrow}\rangle$, are isolated from the Λ-systems mentioned above. From this, one would expect that the optical pumping does not affect $|T_-^{1,2}\rangle$ and $|T_+^{1,2}\rangle$ states, and that the absorption signal of the triplet transition does not vanish in the stability plateau.

However, the data in Fig, 3.4 clearly shows that the population in the entire triplet manifold is depleted due to optical pumping. This implies that there is a mixing[7] among the triplet states or the optical excited states. This mixing can be caused by a number of mechanisms such as Overhauser field fluctuations and inter-QD electron-hole exchange interaction.

Another point to note here is that the radiative spontaneous decay channels between the excited states and the singlet configurations of $|S^{1,1}\rangle$ and $|S^{2,2}\rangle$ have been neglected in the discussion above. This is justified by the fact that the optical transitions involving these states are indirect (see § 2.5), and therefore occur at much lower rates than other direct transitions[68, 69]. From the PL maps, the matrix elements of the indirect optical transitions are estimated to be two orders of magnitude less than those of direct transitions. Furthermore, the singlet configurations of $|S^{1,1}\rangle$ and $|S^{2,2}\rangle$ are unstable in the vicinity of the sweet spot. Hence, we can assume that any population in these states will rapidly relax to the $\mathfrak{S}^{1,2}$ subspace. As a result, the two-electron levels and their excited state manifold around the sweet spot can simply be described by the eight-level system shown in Fig. 3.3. This eight-level model becomes the framework within which coherent optical manipulations of the singlet and triplet states, in addition to spin initialization, can be achieved[7]. This leads to the utilization of the singlet-triplet system as a *single* qubit. The main appeal of the singlet-triplet qubit lies in the $|S^{1,2}\rangle$-$|T_0^{1,2}\rangle$ subspace, which is immune to the decoherence inducing fluctuations of the nuclear spins of the underlying lattice[70, 71]. This is known as the decoherence-free subspace and has been shown to exhibit a long coherence time in the order of 1 μs[8].

3.3 Singlet-triplet states in nonzero magnetic fields

To utilize the singlet-triplet states for two-qubit operations, it is necessary to lift the degeneracy of the triplet states so that each individual state can be optically addressed independently. The easiest way to achieve this is by the application of an external magnetic field. In recent studies of QDMs, external magnetic fields have been applied in Faraday geometry to enhance the coherence time of a singlet-triplet qubit[8], and also in Voigt geometry to provide a proof-of-principle demonstration of a two-qubit phase gate[7]. Later in this chapter, it is shown how the magnetic field in Voigt geometry allows us to deterministically prepare the system in any of its four spin eigenstates. Although the focus of this thesis is on the Voigt geometry, for the sake of completeness and due to its simplicity, Faraday geometry and the resulting energy level structure of the singlet-triplet states are also discussed.

In Faraday geometry, the external magnetic field is applied parallel to the propagation direction of the laser beam, here designated as the z-direction. In this configuration, the eigenstates of the system remain as shown in Fig. 3.3 but the energy levels are shifted relative to one another due to Zeeman interaction. In particular, the degeneracy of the triplet states is lifted. The Hamiltonian for the Zeeman interaction is given by

$$H^{\text{Zee}}_{\text{Faraday}} = \frac{1}{\hbar} \sum_{\alpha,\beta} \langle \alpha | \, \mu_B B_z \left(g_{e,\parallel} \hat{S}_{e,z} - g_{h,\parallel} \hat{S}_{h,z} \right) | \beta \rangle \, \hat{a}^{\dagger} \left(\alpha \right) \hat{a} \left(\beta \right)$$

where μ_B is the Bohr magneton and B_z the applied magnetic field in Faraday geometry, while $g_{e,\parallel}$ and $g_{h,\parallel}$ are the longitudinal g-factors for electron and heavy-hole, respectively. The spin operator $\hat{S}_{e,z}$ acts only on the electron spin and, similarly, $\hat{S}_{h,z}$ on the hole spin. In matrix representation, $H^{\text{Zee}}_{\text{Faraday}}$ takes the form

$$H^{\text{Zee}}_{z,ST} = \mu_B g_{e,\parallel} B_z \begin{bmatrix} 0 & 0 & 0 & 0 \\ 0 & -1 & 0 & 0 \\ 0 & 0 & 0 & 0 \\ 0 & 0 & 0 & 1 \end{bmatrix}$$

for the singlet-triplet ground states in the basis of $\{|S^{1,2}\rangle, |T^{1,2}_{-}\rangle, |T^{1,2}_{0}\rangle, |T^{1,2}_{+}\rangle\}$, and

$$H^{\text{Zee}}_{z,\mathcal{X}^{2-}} = \frac{1}{2} \mu_B B_z \begin{bmatrix} -g_{e,\parallel} + 3g_{h,\parallel} & 0 & 0 & 0 \\ 0 & -g_{e,\parallel} - 3g_{h,\parallel} & 0 & 0 \\ 0 & 0 & g_{e,\parallel} + 3g_{h,\parallel} & 0 \\ 0 & 0 & 0 & g_{e,\parallel} - 3g_{h,\parallel} \end{bmatrix}$$

for the optical excited states in the basis of $\{|\downarrow\rangle |t_{\Downarrow}\rangle, |\downarrow\rangle |t_{\Uparrow}\rangle, |\uparrow\rangle |t_{\Downarrow}\rangle, |\uparrow\rangle |t_{\Uparrow}\rangle\}$. Here, it is assumed that the electron g-factor is the same in both QDs. The resulting magnetic field dependent energy level structure, here known as the "fan diagram", is schematically shown in Fig. 3.5(a), along with all six dipole allowed optical transitions. Note that among the four triplet resonances, each pair of co-polarized transitions are energetically degenerate. Hence, only a total of four distinct resonances are observed in the absorption spectra, as shown in Fig. 3.5(b) for QDM-B in the co-tunneling regime (0.6 V). As a consequence of the degeneracy, it is impossible to independently determine the electron and hole g-factors from the measured resonances. This is because for both singlet and triplet transitions, the Zeeman splitting is the same and is given by $\mu_B B_z \left| g_{e,\parallel} + 3g_{h,\parallel} \right|$.

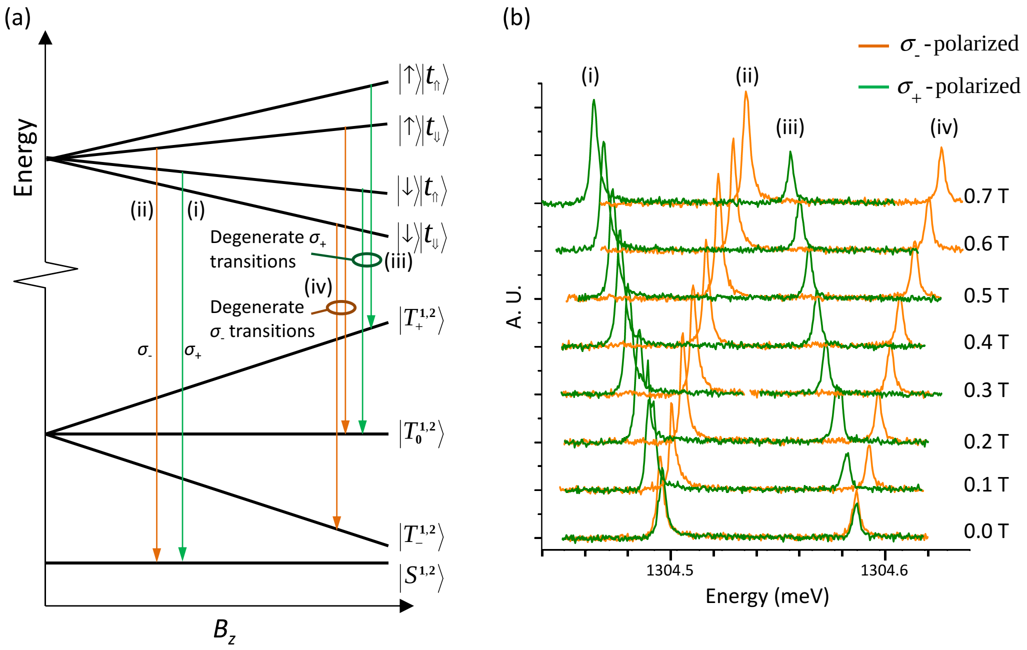

Figure 3.5: (a) Fan diagram showing the energy levels of the singlet-triplet ground states and the optical excited states in an external magnetic field in Faraday geometry. All six dipole allowed optical transitions are indicated, along with the degenerate transitions collectively labeled by the Roman numerals (iii) and (iv) for σ_+ and σ_- transitions, respectively. (b) Magnetic field dependent absorption spectra of QDM-B for σ_+ and σ_--polarized probes in the co-tunneling regime (0.6 V). The spectra are offset for clarity.

In Voigt geometry, also known as the transverse configuration, the magnetic field is applied in a direction perpendicular to the laser beam, here designated as the x-direction. The Hamiltonian,

$$H_{\mathrm{Voigt}}^{\mathrm{Zee}} = \frac{1}{\hbar} \sum_{\alpha,\beta} \langle\alpha| \, \mu_B B_x \left(g_{e,\perp} \hat{S}_{e,x} - g_{h,\perp} \hat{S}_{h,x} \right) |\beta\rangle \, \hat{a}^{\dagger}(\alpha) \, \hat{a}(\beta)$$

can be expressed in matrix representation as

$$H_{x,ST}^{\mathrm{Zee}} = \frac{1}{2} \mu_B g_{e,\perp} B_x \begin{bmatrix} 0 & 0 & 0 & 0 \\ 0 & 0 & \sqrt{2} & 0 \\ 0 & \sqrt{2} & 0 & \sqrt{2} \\ 0 & 0 & \sqrt{2} & 0 \end{bmatrix}$$

for the singlet-triplet ground states, and

$$H^{\text{Zee}}_{x,\mathcal{X}^{2-}} = \frac{1}{2}\mu_B B_x \begin{bmatrix} 0 & -3g_{h,\perp} & g_{e,\perp} & 0 \\ -3g_{h,\perp} & 0 & 0 & g_{e,\perp} \\ g_{e,\perp} & 0 & 0 & -3g_{h,\perp} \\ 0 & g_{e,\perp} & -3g_{h,\perp} & 0 \end{bmatrix}$$

for the optical excited states. Here, $g_{e,\perp}$ and $g_{h,\perp}$ are the transverse g-factors for electron and heavy-hole, respectively. Again, the transverse electron g-factor is assumed to be the same in both QDs. The eigenstates and eigen-energies of the eight-level system in transverse magnetic field is listed below.

$$\begin{array}{lr}
\text{Singlet-triplet ground states:} & \\
\text{Eigenstates} & \text{Eigen-energies} \\
|1\rangle = \left|S^{1,2}\right\rangle = \frac{1}{\sqrt{2}}\left(|\downarrow\rangle|\uparrow\rangle - |\uparrow\rangle|\downarrow\rangle\right) & -2J_{ex} \\
|2\rangle = \frac{1}{2}\left(\left|T^{1,2}_{-}\right\rangle + \left|T^{1,2}_{+}\right\rangle - \sqrt{2}\left|T^{1,2}_{0}\right\rangle\right) = \frac{1}{2}\left(|\downarrow\rangle|\downarrow\rangle + |\uparrow\rangle|\uparrow\rangle - |\downarrow\rangle|\uparrow\rangle - |\uparrow\rangle|\downarrow\rangle\right) & -\mu_B g_{e,\perp} B_x \\
|3\rangle = \frac{1}{\sqrt{2}}\left(\left|T^{1,2}_{-}\right\rangle - \left|T^{1,2}_{+}\right\rangle\right) = \frac{1}{\sqrt{2}}\left(|\downarrow\rangle|\downarrow\rangle - |\uparrow\rangle|\uparrow\rangle\right) & 0 \\
|4\rangle = \frac{1}{2}\left(\left|T^{1,2}_{-}\right\rangle + \left|T^{1,2}_{+}\right\rangle + \sqrt{2}\left|T^{1,2}_{0}\right\rangle\right) = \frac{1}{2}\left(|\downarrow\rangle|\downarrow\rangle + |\uparrow\rangle|\uparrow\rangle + |\downarrow\rangle|\uparrow\rangle + |\uparrow\rangle|\downarrow\rangle\right) & \mu_B g_{e,\perp} B_x
\end{array}$$

$$\begin{array}{ll}
\text{Optical excited states:} & \\
\text{Eigenstates} & \text{Eigen-energies} \\
|5\rangle = \frac{1}{2}\left(|\downarrow\rangle|t_{\Downarrow}\rangle - |\downarrow\rangle|t_{\Uparrow}\rangle - |\uparrow\rangle|t_{\Downarrow}\rangle + |\uparrow\rangle|t_{\Uparrow}\rangle\right) & \frac{1}{2}\mu_B B_x\left(-g_{e,\perp} + 3g_{h,\perp}\right) + E_{ex} \\
|6\rangle = \frac{1}{2}\left(|\downarrow\rangle|t_{\Downarrow}\rangle + |\downarrow\rangle|t_{\Uparrow}\rangle - |\uparrow\rangle|t_{\Downarrow}\rangle - |\uparrow\rangle|t_{\Uparrow}\rangle\right) & \frac{1}{2}\mu_B B_x\left(-g_{e,\perp} - 3g_{h,\perp}\right) + E_{ex} \\
|7\rangle = \frac{1}{2}\left(|\downarrow\rangle|t_{\Downarrow}\rangle - |\downarrow\rangle|t_{\Uparrow}\rangle + |\uparrow\rangle|t_{\Downarrow}\rangle - |\uparrow\rangle|t_{\Uparrow}\rangle\right) & \frac{1}{2}\mu_B B_x\left(g_{e,\perp} + 3g_{h,\perp}\right) + E_{ex} \\
|8\rangle = \frac{1}{2}\left(|\downarrow\rangle|t_{\Downarrow}\rangle + |\downarrow\rangle|t_{\Uparrow}\rangle + |\uparrow\rangle|t_{\Downarrow}\rangle + |\uparrow\rangle|t_{\Uparrow}\rangle\right) & \frac{1}{2}\mu_B B_x\left(g_{e,\perp} - 3g_{h,\perp}\right) + E_{ex}
\end{array} \tag{3.5}$$

where $E_{ex} = E_1 + E_h + V^{\text{Cou}}_{11,11} + V^{\text{Cou}}_{12,21} - 2V^{\text{Cou}}_{1h,h1} - V^{\text{Cou}}_{2h,h2}$. Here, the eigen-energy of state $|3\rangle$ is taken as the reference. If we let

$$|{+x}\rangle = \frac{1}{\sqrt{2}}\left(|\downarrow\rangle + |\uparrow\rangle\right),\ |{-x}\rangle = \frac{1}{\sqrt{2}}\left(|\downarrow\rangle - |\uparrow\rangle\right),$$

$$|t_{+x}\rangle = \frac{1}{\sqrt{2}}\left(|t_{\Downarrow}\rangle + |t_{\Uparrow}\rangle\right) \text{ and } |t_{-x}\rangle = \frac{1}{\sqrt{2}}\left(|t_{\Downarrow}\rangle - |t_{\Uparrow}\rangle\right),$$

the eigenstates can be rewritten as

$$\begin{array}{l}
|1\rangle = \left|S'\right\rangle \equiv \frac{1}{\sqrt{2}}\left(|{-x}\rangle|{+x}\rangle - |{+x}\rangle|{-x}\rangle\right) \\
|2\rangle = \left|T'_{-}\right\rangle \equiv |{-x}\rangle|{-x}\rangle \\
|3\rangle = \left|T'_{0}\right\rangle \equiv \frac{1}{\sqrt{2}}\left(|{-x}\rangle|{+x}\rangle + |{+x}\rangle|{-x}\rangle\right) \\
|4\rangle = \left|T'_{+}\right\rangle \equiv |{+x}\rangle|{+x}\rangle
\end{array} \tag{3.6}$$

$$\begin{aligned}
|5\rangle &= |{-x}\rangle\,|t_{-x}\rangle \\
|6\rangle &= |{-x}\rangle\,|t_{+x}\rangle \\
|7\rangle &= |{+x}\rangle\,|t_{-x}\rangle \\
|8\rangle &= |{+x}\rangle\,|t_{+x}\rangle
\end{aligned}$$

Eq. (3.6) above shows that in Voigt geometry, the optical ground states retain singlet-triplet characteristic, but with spin projections aligned along the direction of the applied magnetic field.

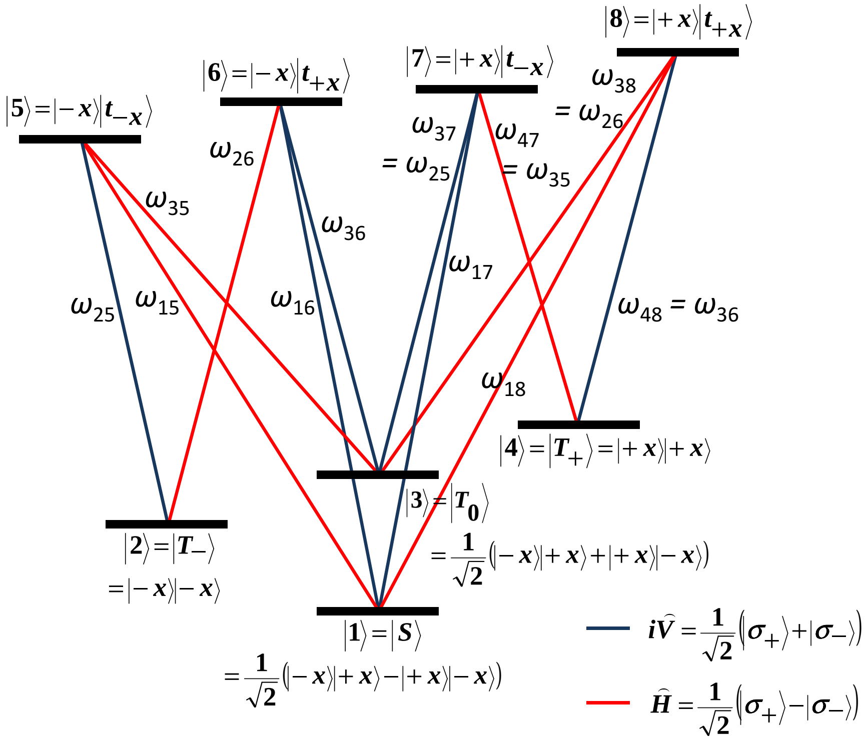

Figure 3.6: The eight-level system and selection rules for optical transitions in a transverse magnetic field (Voigt geometry). For brevity, the primes in the optical ground states are dropped from now on. All transition energies are labeled according to the corresponding ground and excited states, given in numerical subscripts. Degeneracies $\omega_{25} = \omega_{37}$, $\omega_{26} = \omega_{38}$, $\omega_{35} = \omega_{47}$ and $\omega_{36} = \omega_{48}$ are also indicated. Blue and red solid lines represent vertical and horizontal polarizations, respectively.

To determine the selection rules for optical excitation in Voigt geometry, we can follow the same procedure presented in the previous section, where σ_+-polarized light couples $|\uparrow\rangle$ and $|t_{\Uparrow}\rangle$, while σ_--polarized light couples $|\downarrow\rangle$ and $|t_{\Downarrow}\rangle$. Using the definition in Eq. (3.4), let the horizontal and vertical polarizations be defined as $\hat{H} = \hat{x} = \frac{1}{\sqrt{2}}(\sigma_+ - \sigma_-)$ and $\hat{V} = \hat{y} = \frac{1}{\sqrt{2}i}(\sigma_+ + \sigma_-)$, respectively. It is then straight forward to find that the selection rules for optical transitions using linearly polarized light are as shown in Fig. 3.6. Due to spin mixing induced by the transverse magnetic field, transitions which are forbidden in Fig. 3.3 are now allowed. This gives rise to a total of twelve optical transitions. It is important to note that the eight-level system here contains four pairs of doubly degenerate transitions, namely $(\omega_{25}, \omega_{37})$, $(\omega_{26}, \omega_{38})$, $(\omega_{35}, \omega_{47})$ and $(\omega_{36}, \omega_{48})$. Hence, there are eight distinct optical resonances.

The absorption spectra for the eight-level system in Voigt geometry is shown in Fig. 3.7(a) and (b). From Eq. (3.5), the Zeeman splitting for the vertically polarized transitions is given by $\mu_B B_z \left|g_{e,\perp} + 3g_{h,\perp}\right|$, while that for the horizontally polarized transitions is $\mu_B B_z \left|g_{e,\perp} - 3g_{h,\perp}\right|$. In contrast to the Faraday geometry, here the electron and hole g-factors can be independently determined from the Zeeman splittings. For QDM-B, it is found that the electron and hole g-factors are 0.21 and -0.068 respectively, while for QDM-C, they are 0.43 and -0.084. Since $g_{e,\perp} \approx -3g_{h,\perp}$ in QDM-B, $\mu_B B_z \left|g_{e,\perp} + 3g_{h,\perp}\right| \approx 0$ and as a result, the vertically polarized transitions in QDM-B appear to be degenerate at low magnetic fields. The stark difference in the absorption spectra between Fig. 3.7(a) and (b) highlights the role of inhomogeneity in the observed behavior of the eight-level system.

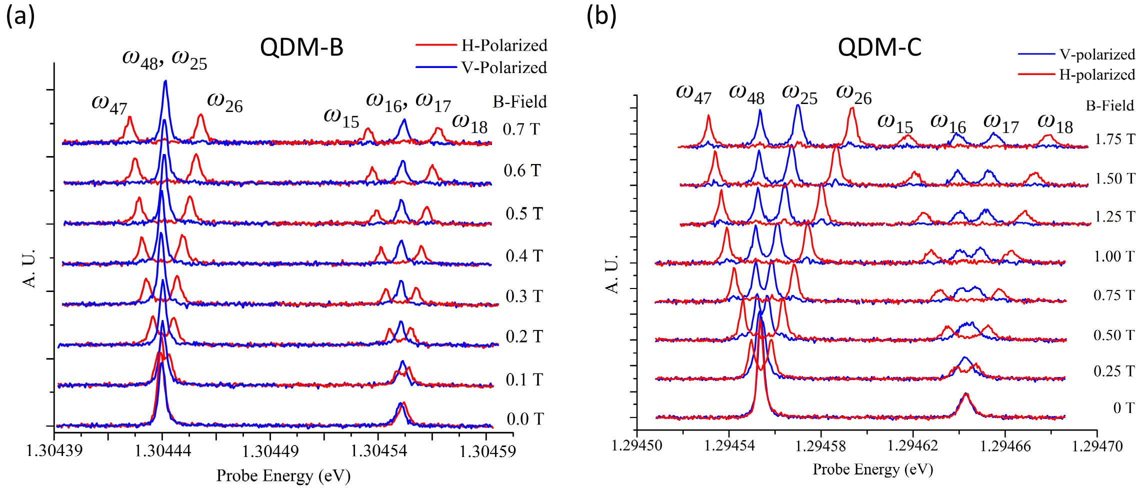

Figure 3.7: Magnetic field dependent absorption spectra for (a) QDM-B and (b) QDM-C in the co-tunneling regimes of respective QDMs, with all eight resonances marked. The spectra are offset for clarity. The vertically polarized resonances in (a) appear to be degenerate at low magnetic fields due to mutual cancellation of electron and hole g-factors in the Zeeman splitting given by $\frac{1}{2}\mu_B B_z \left|g_{e,\perp} + 3g_{h,\perp}\right|$. The resonance peaks of these transitions become resolved at much higher magnetic fields of at least 3 T.

3.4 Two-electron spin preparation via multi-laser optical pumping

In single QDs, the application of an external magnetic field in Voigt geometry causes dark transitions to become bright[15]. This enhances the efficiency of spin flip Raman scattering process and thereby enables fast electron spin preparation by optical pumping. In the same spirit, this method is employed here in conjunction with multiple pump lasers to initialize the two-electron spin to a desired optical ground state. From Fig. 3.7(b), it is shown that for QDM-C, all eight optical resonances can be resolved by the application of a moderate magnetic field. Therefore, in the remaining of this chapter, all experimental studies are performed using QDM-C in 1.5 T applied magnetic field in Voigt geometry.

As mentioned in § 3.2, optical pumping cannot occur in co-tunneling regimes due to rapid relaxation among the optical ground states of multiple charge configurations. To demonstrate optical pumping, it is necessary to operate within the stability plateau of the singlet-triplet configuration. In Fig. 3.8(a), two vertically polarized CW pump lasers, here known as Pump 1 and Pump 2, on resonance with transitions ω_{25} and ω_{48} respectively, are incident on the QDM. Due to the degeneracy in transition frequencies, the pumps also act on transitions ω_{36} and ω_{37}. In a similar manner to the optical pumping process discussed in § 3.2, the system is initialized to the singlet state. A weak probe laser is then scanned across the relevant frequency range in the presence of the pumps. The absorption spectra reveals two peaks corresponding to transitions ω_{15} and ω_{18}, as shown in Fig. 3.8(b). When either of the pump lasers is blocked, the absorption signal at the singlet transitions is diminished. This is because the probe laser now acts as a weak pump, and together with the remaining pump laser, say, Pump 1, initializes the system to the other ground state which is not pumped by the blocked beam, in this case $|T_+\rangle$.

The effectiveness of the optical pumping process can be evaluated by considering the population distribution among the optical ground states under thermal equilibrium. In a magnetic field of 1.5 T, the Zeeman splitting between $|T_-\rangle$ and $|T_+\rangle$ is 74.4 μeV, while the $|S\rangle$-$|T_0\rangle$ splitting is 116.6 μeV. From these values, it is estimated that at the operating temperature of 6 K, the probability density for $|S\rangle$, $|T_-\rangle$, $|T_0\rangle$ and $|T_+\rangle$ are 29.4%, 25.2%, 23.5% and 21.9%, respectively, assuming that Maxwell-Boltzmann distribution applies. In Fig. 3.8(b), the absence of signal at the frequencies of triplet transitions $\omega_{47} = \omega_{35}$ and $\omega_{26} = \omega_{38}$ suggests that the initialization to the singlet state is close to unity. As a crude estimate, the initialization fidelity is taken

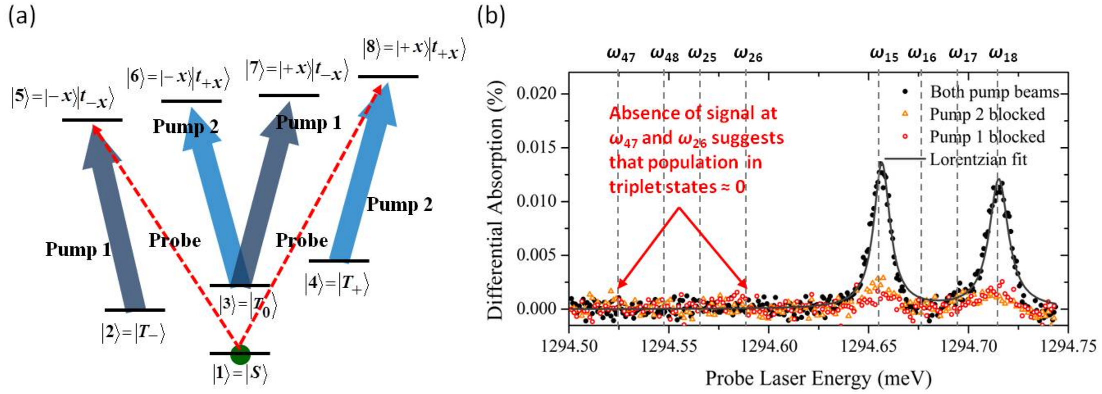

Figure 3.8: (a) Pump configuration for initialization to the singlet state via population pumping. Blue and red arrows represent vertically polarized pump lasers and horizontally polarized scanning probe, respectively. Green solid circle indicates the target state, in this case the singlet state. (b) Differential absorption spectra obtained by scanning the probe laser across all eight resonances, as indicated by vertical dash lines. Solid circles show the data taken with the pump lasers set to $\omega_{25} = \omega_{37}$ and $\omega_{36} = \omega_{48}$ transitions. The realization of singlet state initialization is suggested by the absence of signal at $\omega_{47} = \omega_{35}$ and $\omega_{26} = \omega_{38}$. Measurements are repeated with one of the pump lasers blocked (hollow circles and triangles), resulting in diminished absorption signal.

as the area under the curve in the vicinity of ω_{15} and ω_{18} divided by the total area under the curve of the Lorentzian fit shown in Fig. 3.8(b). A measurement noise limited fidelity of 98 % is then obtained. From this value, the spin temperature as a result of optical pumping is estimated to be 0.24 K. This is significantly lower than the operating temperature of 6 K.

Although vertically polarized pump lasers are chosen in the scheme shown in Fig. 3.8(a), initialization to the singlet state can also be accomplished with horizontally polarized pumps. Furthermore, by tuning one of the pump lasers to the resonance of a singlet transition, the dual laser optical pumping method can be used to initialize the system to the triplet states $|T_+\rangle$ and $|T_-\rangle$. Fig. 3.9 summarizes all six possible dual laser optical pumping schemes for initialization to the singlet, $|T_+\rangle$ and $|T_-\rangle$ states, including the one discussed above. Each of these states can be prepared with two pump configurations. For initialization to the triplet states, the fidelity can be estimated in the same manner as above, and the values of 0.90 and 0.94 are obtained for the cases of $|T_+\rangle$ and $|T_-\rangle$, respectively. In both cases, the loss of fidelity is mainly due to measurement noise from the experimental setup. The results of the dual laser optical initialization process can be summarized by the truth table shown in Fig.

3.10.

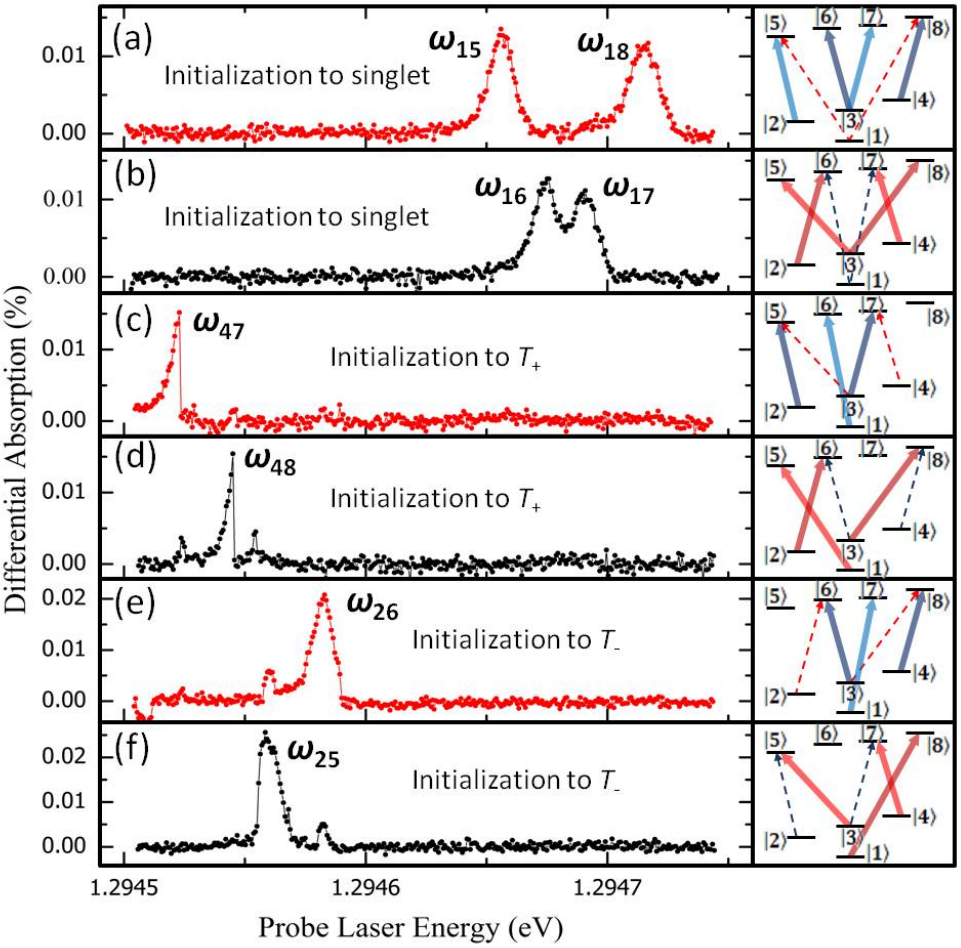

Figure 3.9: All six possible configurations for dual laser optical pumping and their resulting absorption spectra. Panel (a) & (b): Initialization to the singlet state. The absence of signal at the triplet resonances signifies high-fidelity spin preparation of the singlet state. Pump configurations giving rise to these spectra are given in the boxes to the right, where solid arrows represent pump lasers while dashed arrows the probe. Vertically polarized light is color coded in blue while horizontally polarized light in red. Panel (c) & (d): Initialization to $|T_+\rangle$ state. Panel (e) & (f): Initialization to $|T_-\rangle$ state.

So far the discussion has not involved the coherence of the spin states. In Fig. 3.8(a), when the scanning probe and one of the pump lasers are in two-photon resonance, i. e., when their frequency difference equals the corresponding singlet-triplet

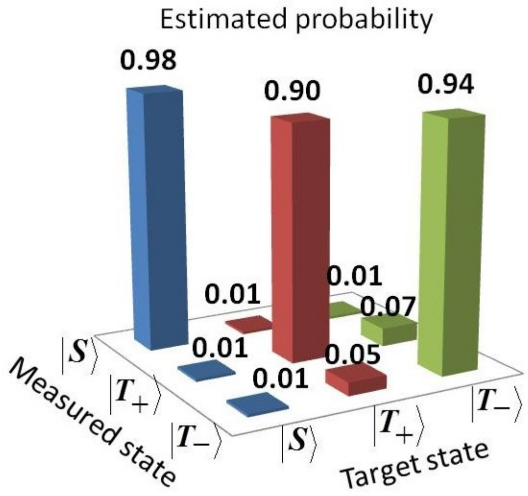

Figure 3.10: Truth table for the process of dual laser optical initialization. Columns color-coded in blue, red and green correspond to initialization to the singlet, $|T_+\rangle$ and $|T_-\rangle$, respectively. Here, the fidelity for the initialization process for each case is given by the diagonal elements, from which the values of 0.98, 0.90 and 0.94 are obtained for the singlet, $|T_+\rangle$ and $|T_-\rangle$, respectively.

splitting, a dark-state will be formed due to coherence population trapping. Therefore, one expects to see dark-state dips in the spectrum given by the solid circles in Fig. 3.8(b). The absence of a dark-state dip suggests a significant degradation of the coherence lifetime, which stands in contrast to the long spin coherence observed in QDMs and single QDs[11, 8]. Another anomaly is seen in Fig. 3.9 where the absorption lineshapes shown in panels (c) to (e) deviate considerably from Lorentzian. These observations suggest the involvement of the nuclear spin ensemble of the underlying crystal lattice in the dynamics of optical spin manipulation. In the next chapter, some of these phenomena will be further explored.

From DiVincenzo criteria for quantum computation[6], it suffices to be able to initialize to a known quantum state, given that other criteria are met. However, to demonstrate a universal set of quantum gates, it helps to perform quantum process tomography, which requires all basis states as input. Here, the only two-electron spin state that cannot be prepared using the method discussed above is $|T_0\rangle$. As seen in Fig. 3.6, due to the degeneracy in transition frequencies, any pump laser acting on $|T_+\rangle$ or $|T_-\rangle$ also depletes the population in $|T_0\rangle$ state. Nevertheless, if the system is first initialized to the singlet state, one can then transfer the population to the $|T_0\rangle$ state via stimulated Raman adiabatic passage (STIRAP) or by using a sequence of

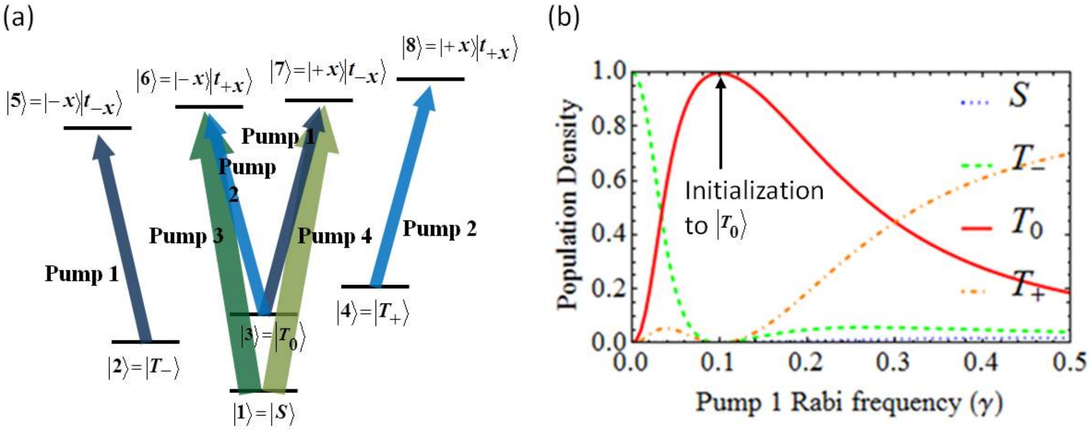

Figure 3.11: (a) Pump configuration for spin preparation of $|T_0\rangle$ state using four CW lasers. The population is confined to the $|S\rangle$-$|T_0\rangle$ subspace due to Pump 1 and Pump 2. By virtue of CPT driven by Pump 2 and Pump 3 on one side and Pump 1 and Pump 4 on the other, a coherent superposition of $|S\rangle$ and $|T_0\rangle$ is formed. If Pump 3 and Pump 4 are made arbitrary strong, the system is essentially prepared in $|T_0\rangle$ state. (b) Calculated ground state populations as a function of Pump 1 Rabi frequency in units of radiative decay rate, γ. Rabi frequencies used here are 0.1γ, 2γ and 2γ for Pump 2, Pump 3 and Pump 4, respectively.

circularly polarized picosecond pulses. A third method requiring only CW lasers is shown in Fig. 3.11(a). As in the case for singlet state initialization, Pump 1 and Pump 2 deplete the population in $|T_+\rangle$ and $|T_-\rangle$. As a result, the system is confined to the $|S\rangle$-$|T_0\rangle$ subspace. Here, Pump 2 and Pump 3 are in two-photon resonance, thereby forming a Λ-system containing states $|S\rangle$, $|6\rangle$ and $|T_0\rangle$. Similarly, Pump 1 and Pump 4 form another Λ-system. From these two Λ-systems, coherent population trapping (CPT) ensues and a coherent superposition of $|S\rangle$ and $|T_0\rangle$ is created, of which the relative composition is determined by the intensities of the pump lasers. As shown in Fig. 3.11(b), if Pump 3 and Pump 4 have much higher intensities compared to Pump 1 and Pump 2, the system is essentially initialized to $|T_0\rangle$ state when the intensities of Pump 1 and Pump 2 are equal. Since the process of CPT is integral for the $|T_0\rangle$ initialization technique discussed here, the effectiveness of this method relies on the coherence properties of the eigth-level system. Although this *coherent optical pumping* scheme is yet to be demonstrated experimentally, it is in principle viable given sufficient isolation of the eight-level system from the decoherence inducing environment.

3.5 Conclusion

In this chapter, the effects of optical pumping in two-electron configuration with zero and nonzero applied magnetic fields are presented. The most important result derived here is given in Fig. 3.6 for the eight-level system in a transverse magnetic field (Voigt geometry). The accuracy of this eight-level model, along with the selection rules for optical transitions, is demonstrated by a series of optical pumping schemes shown in Fig. 3.9. At the same time, the resulting spectra from optical pumping suggest that high fidelity two-electron spin initialization can be achieved. It should be emphasized that the loss of initialization fidelity here is mainly due to noise associated with the measurement and one expects significant improvements when better instrumentation is employed. However, the results from optical pumping also expose some unexpected behaviors, notably the highly asymmetrical lineshapes in the absorption spectra. These deviations from ideal lineshapes are known to originate from the nuclear spin polarization and might present as an obstacle for the demonstration of two-qubit operations using QDMs. In the next chapter, it will be shown how this impediment can be overcome by means of optical manipulations with CW lasers.

CHAPTER IV

Dynamic Nuclear Spin Polarization and Optical Nuclear Spin Locking in QDMs: Extended Two-Electron Spin Coherence

The physical platform for two-electron spin manipulation in optically active QDMs is laid out in the previous chapter as the eight-level system in a transverse magnetic field shown in Fig. 3.6. Based on this simple model, it was shown that optical two-electron spin initialization to all four eigenstates is, in principle, attainable via the multi-laser optical pumping technique. Three of these cases, namely the singlet, $|T_+\rangle$ and $|T_-\rangle$ spin state preparations are experimentally demonstrated, while initialization to $|T_0\rangle$ is theoretically possible with the application of four CW lasers. The simplicity of the eight-level model obscures the fact that the interactions between the QDM-confined electrons and their surrounding environment is entirely ignored. From the irregularity of the lineshapes observed, it is obvious that these interactions play significant roles in the optical measurements of the two-electron spin states. Among them, the nuclear hyperfine interaction between an electron and the underlying nuclear spin ensemble of the lattice is known to produce complex behaviors in the presence of optical excitations.

The nuclear hyperfine interaction couples the electron spin to a fluctuating bath of nuclear spins. Because of this, the energy states of the two-electron system become unstable under the influence of a changing net polarization of the nuclear spin ensemble. The presence of nuclear spin fluctuations complicates certain aspects of optical studies in QDMs. For example, as seen in the previous chapter, it is difficult to extract coherent properties of a QDM from the absorption lineshapes due to the absence of dark-state dips caused by nuclear spin fluctuations. Furthermore, it will become troublesome later on for two-qubit operations where a precise control of the detuning and timing of the optical fields is required. As instability in energy levels causes random shifts in spin precession frequencies, the fidelity of two qubit operations deteriorates in the presence of nuclear spin fluctuations.

Fortunately, as was first demonstrated in single QDs[3], nuclear spin fluctuations in QDMs can also be controlled optically. In this chapter, it will be explained how nuclear hyperfine interaction gives rise to a non-collinear hyperfine term which induces a net nuclear spin polarization (NSP), in conjunction with optical pumping and strain induced electric field gradient. Again, due to the nuclear hyperfine interaction, the NSP in turn produces an effective magnetic field, known as the Overhauser field, that shifts the energy levels of the spin states. This interplay between the electron and nuclear spins forms the basic mechanism[72, 73, 74, 75] for dynamic nuclear spin polarization (DNSP). The DNSP is known to cause highly asymmetric lineshapes depending on the spin states of the electron. However, under conditions where the DNSP is stabilized via optical nuclear spin locking, it gives rise to the suppression of nuclear spin fluctuations[3]. The outcomes show "DNSP-free" dark-state lineshapes from which long spin coherence of about 1 μs can be inferred for the two-electron spin states. For the QDM used in this study, the significance of this observation lies in the fact that all optical manipulations involve only the trion states of the top QD. Since the electron wavefunctions are largely confined within individual QDs at the operating bias, this implies that the nuclear spin locking is somehow channelled from the top QD to the bottom QD, possibly due to the small amount of electron wavefunction overlap. The result is hereby interpreted as non-local nuclear spin locking. Meanwhile, as an effort to lay down the groundworks for the optical nuclear spin locking technique, the effects of DNSP and its physical origin in the context of optical studies in QDMs will be discussed in the following section.

4.1 Resonance pulling and resonance pushing lineshapes as indicators of electron spin induced DNSP

As noted in the previous chapter, in all cases of optical spin preparation with two pump lasers, the absorption lineshapes deviate significantly from the expected dark-state profile. To look at these lineshapes more closely, let us begin with the cases where the spin preparation of $|T_{-}\rangle$ and $|T_{+}\rangle$ states is accomplished by using pump configurations shown in Fig. 4.1(a) and (c), respectively. In both schemes, Pump 1 behaves simply as a narrow-band light source to deplete any population in the singlet state resulting from spontaneous decay and ground state population relaxation. Its frequency is chosen so that it does not couple to the same excited state as Pump 2 in order to avoid population transfer to the singlet state via coherent population trapping (CPT), i.e., formation of a dark state. Pump 2 and the probe laser couple states $|T_-\rangle$, $|T_0\rangle$, $|T_+\rangle$, $|6\rangle$ and $|8\rangle$, forming a double Λ-system with a shared $|T_0\rangle$ ground state. Due to the degeneracy in optical resonances, these two Λ-systems are identical except for their optical dipole moments. In an ideal case, the dipole moment of transition ω_{25} is a factor of $\sqrt{2}$ greater than that of ω_{37}, while the dipole moment of ω_{35} is smaller than that of ω_{47} by a factor of $\sqrt{2}$. Due to the resemblance of the double Λ-system to the letter "M", it is hereby referred to as an M-subsystem. When Pump 2 and the probe form a two-photon resonance, i.e., when their frequency difference equals the corresponding triplet state splitting, CPT ensues and one expects a dark-state dip in the probe absorption spectrum, as shown in the inset of Fig. 4.1(b).

For the pump configuration shown in Fig. 4.1(a), the measured absorption spectra of the probe given in Fig. 4.1(b) shows a strong signal at the $|T_-\rangle$ resonance of ω_{25}, and negligible signals at other transitions. This is consistent with the spin preparation of the $|T_-\rangle$ state discussed in the previous chapter. However, it is evident that the measured probe absorption lineshapes significantly deviates from that expected. A more complex structure of a broadened resonance with a round top, abrupt rising and falling edges, and a shifted "partial dip" is obtained. This resonance profile is observed in earlier studies in single QDs[3, 76] and is referred to as the "frequency pulling[77, 78]" or "dragging[76]" behavior. Furthermore, by scanning the probe laser in backward direction (decreasing in frequency), the lineshape obtained is different from that of forward direction. In other words, hysteresis with respect to scan direction is present in the system. This and the frequency pulling behavior are the hallmarks of DNSP in InAs QDs.

In the other scheme for the initialization of the $|T_+\rangle$ state shown in Fig. 4.1(c), the roles of Pump 2 and the probe are reversed. An M-subsystem identical to the previous one is formed. Again, the presence of a strong signal at the $|T_+\rangle$ resonance of ω_{47} indicates that the system is almost entirely in $|T_+\rangle$ state throughout the scan. When the probe laser is scanned in forward direction towards the resonance at ω_{47}, the signal first increases, but upon approaching the two photon resonance, drops abruptly to a value close to the noise floor. As the scanning progresses, the signal reappears suddenly then gradually diminishes. The same behavior is observed in the backward scan, resulting in a lineshape that roughly resembles a mirror reflection of the former about the resonance frequency of ω_{47}. These striking profiles as shown in Fig. 4.1(d) are the outcomes of the "frequency pushing" or "anti-dragging[76]"

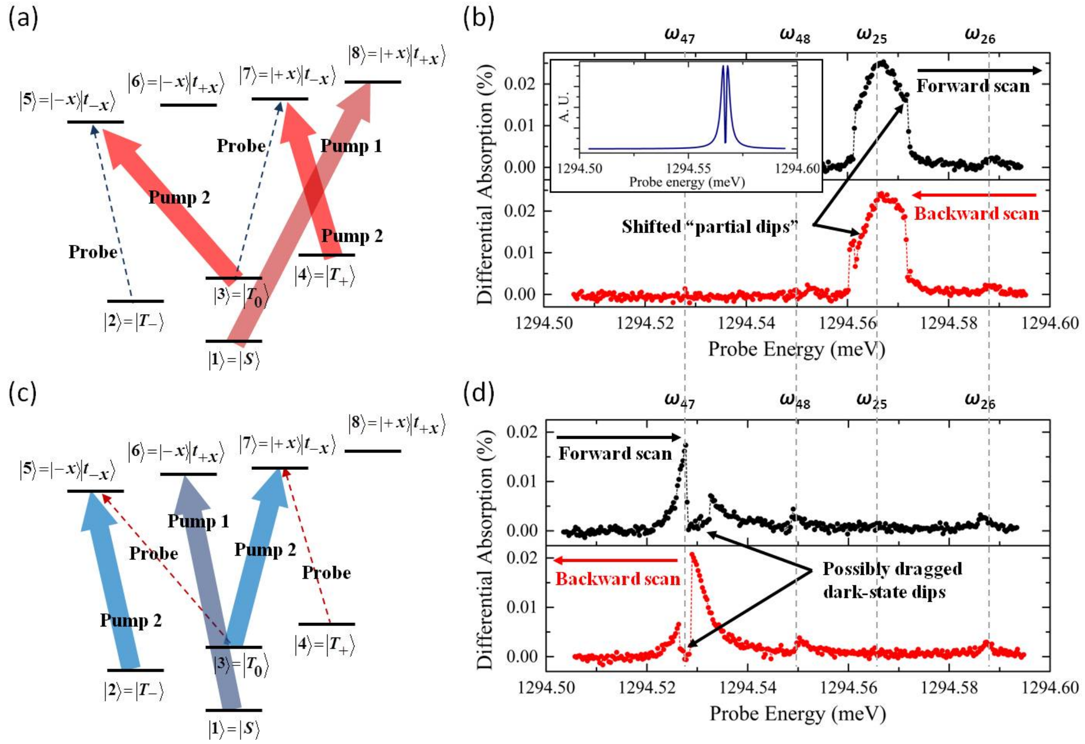

Figure 4.1: Resonance pulling and pushing lineshapes in spin triplet manifold. (a) Pump configuration for $|T_-\rangle$ state preparation. Here thick solid arrows represent the pumps while dashed arrow the probe. Polarizations of the optical fields are indicated by red and blue for horizontal and vertical, respectively. (b) Following the pumping scheme in (a), the upper panel shows the absorption spectrum of a vertically polarized probe laser scanned in forward (increasing in frequency) direction, while the lower panel in backward direction. The spectra show hysteresis with respect to scan direction and resonance pulling behavior due to DNSP. Inset: Ideal CPT lineshape with a dark-state dip. (c) Pump configuration for $|T_+\rangle$ state preparation. (d) Absorption spectra showing resonance pushing behavior with a horizontally polarized probe. In both pump configurations, the spin state of the optically excited trion, determined by the heavy-hole spin, remains the same.

behavior.

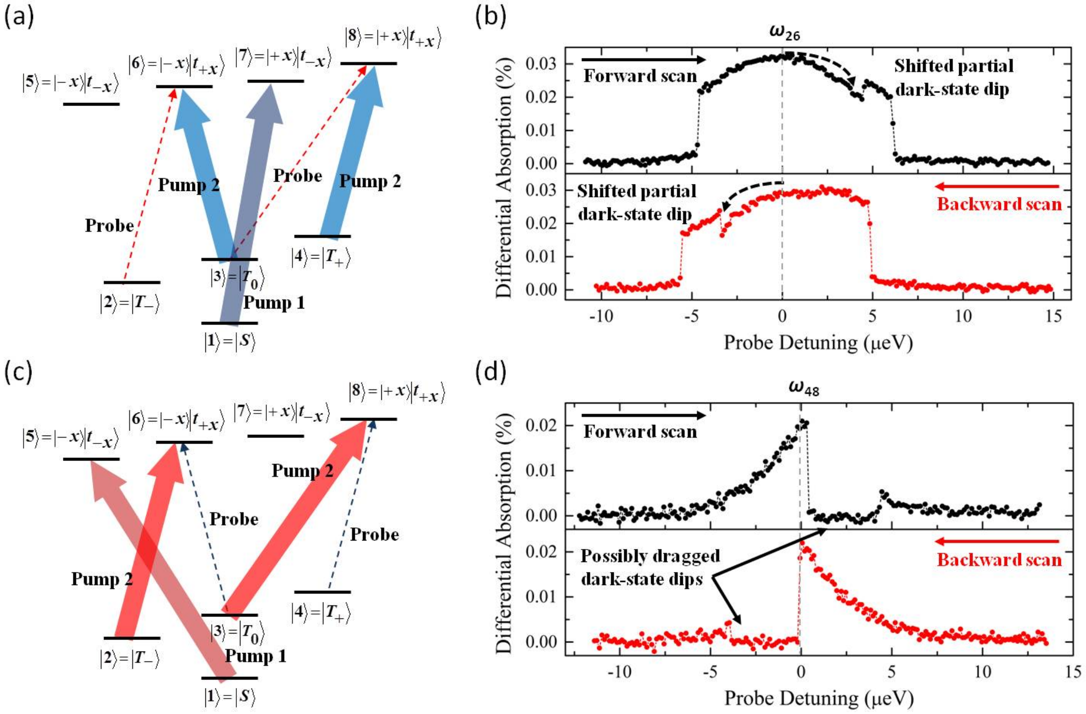

Figure 4.2: (a) and (c) Optical spin preparation of $|T_-\rangle$ and $|T_+\rangle$ states, respectively, using alternative pump configurations. (b) and (d) Corresponding high-resolution probe absorption spectra showing that, despite the difference in pump configurations and resulting heavy-hole spins, the observed behavior is qualitatively similar to that shown in Fig. 4.1.

It worths noting that in both pump configurations discussed above, the probe and Pump 2 couple to the spin-down state of the heavy-hole. At this point it seems reasonable to assume that the resonance profiles are associated with the electron spins, where $|T_-\rangle$ state gives rise to frequency pulling behavior, while $|T_+\rangle$ frequency pushing. To provide further evidence that the hole spin indeed plays little role in DNSP, it is necessary to couple to a different hole spin. This is achieved with alternative pump configurations shown in Fig. 4.2(a) and (c) for initializing to $|T_-\rangle$ and $|T_+\rangle$ states, respectively. The corresponding probe absorption spectra are given in Fig. 4.2(b) and (d), in which the probe laser is scanned in finer step sizes compared to previous experiments, across the resonances where the signals are expected to appear. Here, the probe and Pump 2 excite the spin-up heavy-hole state, as opposed to the spin-down state in previous cases. Nonetheless, both frequency pulling and pushing lineshapes qualitatively similar to those in Fig. 4.1(b) and (d) are obtained, each arising from the initialization of $|T_-\rangle$ and $|T_+\rangle$ states, respectively. This implies that although the upper-QD trion maybe involved in the mechanism of DNSP, its spin projection, which is entirely determined by the heavy-hole spin, plays negligible role. As a side note, the optically induced DNSP reported earlier in single QDs is attributed to either electron-nuclear non-collinear hyperfine interaction arising from nuclear quadrupolar field[79, 76, 73, 74], or hole-nuclear non-collinear hyperfine coupling due to heavy-hole-light-hole mixing[3, 73]. It is very likely that the underlying mechanism of DNSP in QDs varies from one sample to another[76, 74], and the results above suggest that the behavior of the QDM under study is governed by the former.

4.2 General mechanism of DNSP in InAs QDs

Although a detailed physical description of DNSP in QDMs is yet to be elucidated, a partial understanding can be developed based on earlier studies in single QDs. As mentioned in the introductory section of this chapter, the theoretical framework of DNSP is cast in the form of a feedback loop leading to the generation of NSP via optical pumping and the back-action of the NSP on the optical resonances[75]. Both processes arise from the electron-nuclear hyperfine interaction. In the former, it takes the shape of the non-collinear hyperfine[79, 76, 73, 74] term having the generic form $\sum_i A_i^{\mathrm{NC}} \hat{S}_{e,x} \hat{I}_{i,y}$, and electron spin mediated nuclear spin diffusion[80, 79, 81, 74] term given by $\sum_{i,j} A_{ij}^{\mathrm{SD}} \hat{S}_{e,x} \hat{I}_{i,+} \hat{I}_{j,-}$. Here, A_i^{NC} and A_i^{SD} are coupling constants for the non-collinear and spin diffusion terms, respectively. $\hat{S}_{e,x}$ denotes electron spin operator in the x-direction (in the same direction as the applied magnetic field), chosen here as the quantization axis, while $\hat{I}_{i,z}$ is the spin operator of i-th nucleus. The spin-flip operators are defined as $\hat{I}_{i,\pm} = \hat{I}_{i,z} \mp i\hat{I}_{i,y}$.

In recent studies of single QDs, the non-collinear term is found to be the largest contributor for NSP[79, 82, 76, 74, 81] and is due to the interaction between the electric nuclear quadrupolar moment and the electric field gradient induced by strain. The fact that strain is ubiquitous in nanostructures due to lattice mismatch and alloying makes the nuclear quadrupolar interaction important. To briefly see how the non-collinear term arises from nuclear quadrupolar interaction, let us begin with the Hamiltonian

$$\begin{aligned} H = {} & H^{\mathrm{OPT}} + \frac{g_e \mu_B}{\hbar} \widehat{\mathbf{S}}_e \cdot \mathbf{B} - \frac{\mu_N}{\hbar} \sum_i g_{n,i} \widehat{\mathbf{I}}_i \cdot \mathbf{B} \qquad (4.1) \\ & - \frac{\mu_0}{4\pi} \gamma_e \sum_i \gamma_{N,i} \widehat{\mathbf{I}}_i \cdot \left[\frac{8\pi}{3} \widehat{\mathbf{S}}_e \delta\left(\mathbf{r}_i\right) - \frac{r_i^2 \widehat{\mathbf{S}}_e - 3\mathbf{r}_i \left(\widehat{\mathbf{S}}_e \cdot \mathbf{r}_i \right)}{r_i^5} + \frac{\hat{\mathbf{L}}}{r_i^3} \right] - \frac{1}{2} \sum_i \hat{\mathbf{Q}}_i^{(2)} \cdot \mathbf{V}_i^{(2)} \end{aligned}$$

Here, H^{OPT} represents the Hamiltonian term for QD-optical field interaction. The second and third terms are the Zeeman interactions for electron and nuclei, respectively, in which μ_N is the nuclear magneton while $g_{n,i}$ the g-factor of i-th nucleus. The fourth term is the hyperfine interaction in terms of separation between the electron and i-th nucleus, $\mathbf{r}_i$. γ_e and $\gamma_{N,i}$ denote electron and nuclear gyromagnetic ratios, respectively, while $\hat{\mathbf{L}}$ the electron orbital angular momentum operator. Finally, the fifth term gives us nuclear quadrupolar interaction, where $\hat{\mathbf{Q}}_i^{(2)}$ and $\mathbf{V}_i^{(2)}$ are the nuclear quadrupolar moment and electric field gradient tensors, respectively, evaluated at the site of i-th nucleus. The hole-nuclear hyperfine term is neglected in the Hamiltonian above since it is expected to be an order of magnitude smaller compared to the electron-nuclear hyperfine term[83, 84, 85, 86, 87]. The hyperfine interaction consists of the Fermi contact term, the electron-nuclear magnetic dipole coupling and the spin-orbit coupling between nuclear spin and electron angular momentum, in the order presented in Eq. (4.1) above. If we assume s-type Bloch states with slowly varying envelop wavefunctions for the electron[3], we can keep only the Fermi contact term, so that the Hamiltonian in Eq. (4.1) is simplified to

$$H \approx H^{\mathrm{OPT}} + \frac{g_e \mu_B}{\hbar} \widehat{S}_{e,x} B_x - \frac{\mu_N}{\hbar} \sum_i g_{n,i} \widehat{I}_{i,x} B_x + \sum_i A_{e,i} \widehat{\mathbf{S}}_e \cdot \widehat{\mathbf{I}}_i - \frac{1}{2} \sum_i \hat{\mathbf{Q}}_i^{(2)} \cdot \mathbf{V}_i^{(2)} \quad (4.2)$$

for an applied magnetic field in Voigt geometry. $A_{e,i}$ is also known as the electron-nuclear hyperfine constant. To see how Eq. (4.2) gives rise to the non-collinear hyperfine term, we apply a unitary transformation so that the Hamiltonian in the rotated basis, $\tilde{H}$, has the form

$$\tilde{H} = e^{\mathscr{S}} H e^{-\mathscr{S}}$$

With an appropriate choice of $\mathscr{S}$, e. g.

$$\mathscr{S} = \frac{1}{B_x} \sum_i c_i \left[2 \left(\hat{I}_{i,+} \hat{I}_{i,x} - \hat{I}_{i,x} \hat{I}_{i,-} \right) + \hat{I}_{i,+} - \hat{I}_{i,-} \right]$$

where c_i is a constant, the quadrupolar term in Eq. (4.2) can be eliminated. This is known as the Schrieffer-Wolff transformation[88, 76, 74] and a detailed discussion is given in Appendix D. The resulting Hamiltonian is

$$\tilde{H} \approx H^{\mathrm{OPT}} + \frac{g_e \mu_B}{\hbar} \widehat{S}_{e,x} B_x - \frac{\mu_N}{\hbar} \sum_i g_{n,i} \widehat{I}_{i,x} B_x + \sum_i A_{e,i} \widehat{\mathbf{S}}_e \cdot \widehat{\mathbf{I}}_i + \sum_i A_i^{\mathrm{NC}} \left(i \hat{S}_{e,x} \hat{I}_{i,y} + \cdots \right)$$

where the non-collinear hyperfine constant, A_i^{NC}, is proportional to the product of nuclear quadrupolar moment and electric field gradient. Once again, the quantization axis is chosen to be along the x-direction. It is important to emphasize that the Schrieffer-Wolff transformation does not alter the Hamiltonian physically, but merely shows certain aspects of the interactions in a more explicit manner. From $\hat{I}_{i,z} = \frac{1}{2}\left(\hat{I}_{i,+} + \hat{I}_{i,-}\right)$, it is easy to see that the non-collinear term induces nuclear spin flips, and as an accumulative effects across the nuclear ensemble, results in NSP.

The spread of NSP across the entire QDM, especially to locations where the strain is negligible, is facilitated by the electron spin mediated nuclear spin diffusion term mentioned earlier. The derivation of this term can be done by neglecting the nuclear quadrupolar interaction in Eq. (4.2), and again, by applying the Schrieffer-Wolff transformation but this time using

$$\mathscr{S} = \frac{1}{B_x}\sum_i c_i^{'}\left(\hat{S}_+\hat{I}_{i,-} - \hat{S}_-\hat{I}_{i,+}\right)$$

we have

$$\begin{aligned} \tilde{H}^{'} \approx\ & H^{\mathrm{OPT}} + \frac{g_e\mu_B}{\hbar}\widehat{S}_{e,x}B_x - \frac{\mu_N}{\hbar}\sum_i g_{n,i}\widehat{I}_{i,x}B_x + \sum_i A_{e,i}\widehat{S}_{e,x}\widehat{I}_{i,x} \\ & + \sum_{i,j} A_{ij}^{\mathrm{SD}}\left(\hat{S}_{e,x}\hat{I}_{i,+}\hat{I}_{j,-} + \cdots\right) \end{aligned} \tag{4.3}$$

where

$$A_{ij}^{\mathrm{SD}} = \frac{\hbar A_{e,i}A_{e,j}}{4\left(g_e\mu_B + \mu_N g_{N,j}\right)B_x}$$

The term $\sum_i A_{e,i}\widehat{S}_{e,x}\widehat{I}_{i,x}$ in Eq. (4.3) above is known as the Overhauser shift, since it gives rise to an effective magnetic field, i. e., the Overhauser field, given by

$$B_{OH} = \frac{\hbar}{g_e\mu_B}\sum_i A_{e,i}\widehat{I}_{i,x}$$

As a result, the energy levels of the spin states and, subsequently, the optical resonances, are shifted. This in turn changes the dynamics of the optical pumping process and therefore, brings about the back-action of the NSP on the optical excitaton.

The effects of DNSP seen in the optical pumping experiments discussed above in § 4.1 is summarized in Fig. 4.3. The process begins with the optical initialization to a nonzero spin state of either $|T_-\rangle$ or $|T_+\rangle$, which induces NSP via non-collinear hyperfine interaction. When the probe laser is scanned across the resonance associated with the prepared spin state, the total electron spin projection of the system is perturbed

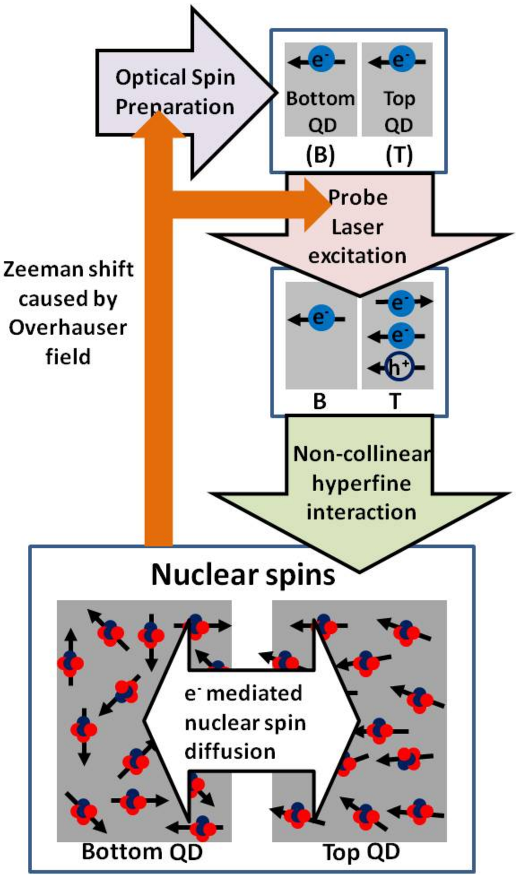

Figure 4.3: A schematic illustration of the mechanism of DNSP showing the feedback between optical pumping induced NSP and NSP induced Overhauser shift.

due to either optical transition to a trion state or CPT. In response, the amount of NSP is changed since the electrons and nuclei are coupled. This translates to a shift in the Overhauser field, which in turn alters the energy levels of the eigenstates and, consequentially, affects the dynamics of the optical pumping process. In optical pumping experiments, this feedback mechanism manifests in the frequency pulling and pushing lineshapes shown in Fig. 4.1 and 4.2. This "asymmetrical" response of the system with respect to the electron spin state is likely due to the change in the dynamics of the feedback loop[81, 75], since switching the electron spin state flips the sign of the non-collinear term. In order to reproduce the observations theoretically, one must find the steady state solution involving all physical processes labeled in Fig. 4.3. This proves to be a challenging task and, in the case of single QDs, several attempts are made[3, 88, 81, 73]. Nonetheless, the basic idea of DNSP discussed here is sufficient for the effort of suppressing the frequency pulling and pushing behaviors.

4.3 Recovery of dark-state lineshapes by nuclear spin locking: Extended electron spin coherence

The frequency pulling and pushing lineshapes provide little information on the coherence time of the two-electron spin state. Based on the understanding of DNSP given in § 4.2, these spectral distortions caused in part by changes in DNSP can be avoided if the effect of the probe laser on DNSP can be minimized. The most straightforward way to achieve this is by reducing the intensity of the probe laser at the expense of signal to noise ratio. For the purpose of measuring spin coherence time in CW spectroscopy by measuring the dip of the dark-state formed by CPT, this method is detrimental since a low signal to noise ratio in the vicinity of the dark-state dip greatly reduces the accuracy of the estimated coherence time. For a better approach, a third pump laser tuned to the two-photon resonance with Pump 2 is applied, as shown in Fig. 4.4(a) and (c). As previously noted, Pump 1 plays little role in the coherence of the optical ground states. In both schemes, a configuration similar to that for CPT in an ordinary Λ-system is formed by Pump 2 and 3 in each half of the M-subsystem. In this more complex CPT configuration, a coherent state is formed between the components of the triplet manifold ($|T_-\rangle$, $|T_0\rangle$ and $|T_+\rangle$) with probability amplitudes dictated by the relative intensities of the pumps and the relevant optical dipole moments. For the effective intensity ratio of Pump 2 to Pump 3 arbitrarily chosen to be $25 : 1$, most of the ground state probability amplitude is associated with the $|T_-\rangle$ state for the pump configuration shown in Fig. 4.4(a), while in Fig. 4.4(c), the prepared spin state is predominantly $|T_+\rangle$.

As long as the probe is weaker than the pumps, this has the effect of stabilizing the ground state probability amplitudes against the perturbation caused by the probe, thereby keeping the electron spin induced NSP relatively constant, i.e., locking the nuclear spins[3]. In the absorption spectra shown in Fig. 4.4(b) and (d), corresponding to the pump configurations in Fig. 4.4(a) and (c) respectively, a prominent dark state dip is now observed in each case. The full depth of both dips indicates strong suppression of nuclear spin fluctuations and long ground state decoherence times. The recovery of the dark-state profiles allows us to simulate the behavior of the system without considering the effects of DNSP. By using the eight-level master equation given in Appendix E, the numerically obtained best fit lineshapes are overlaid on the experimental results. The accuracy of the model is evident not just by the excellent fits it generates, but also by its ability to account for the kink, as indicated in Fig. 4.4(b), due to a slight misalignment of the pump detunings. From the fits in Fig.

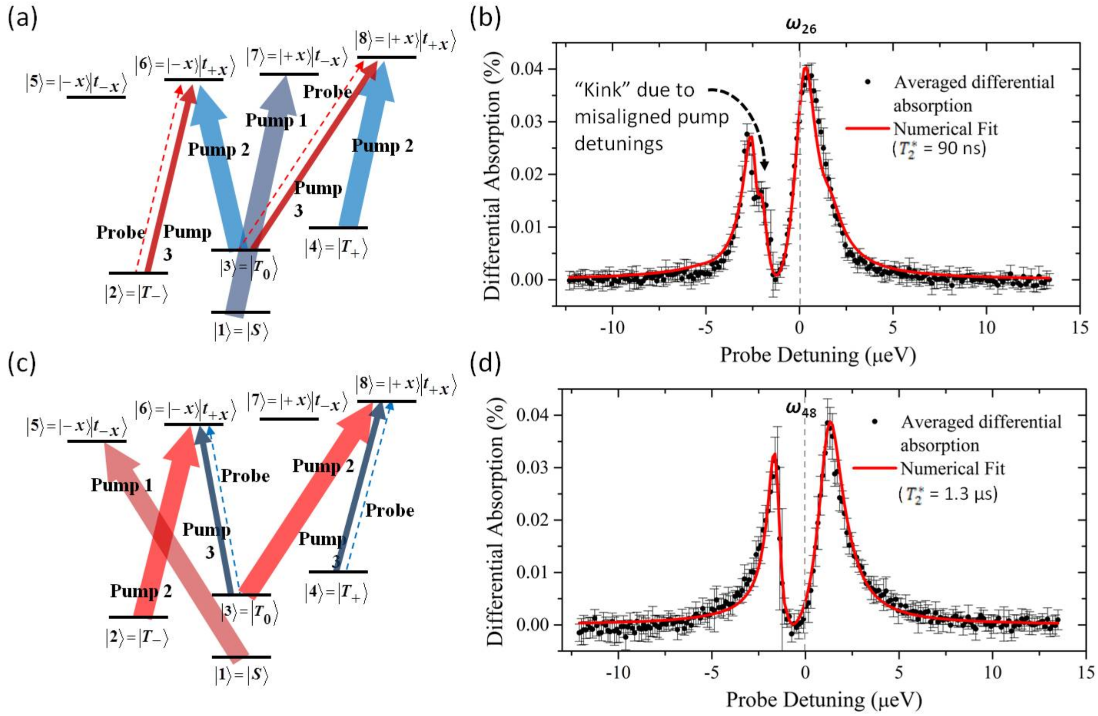

Figure 4.4: Nuclear spin locking and the recovery of dark state lineshapes. (a) and (c) Pump configurations similar to those shown in Fig. 4.2(a) and (c), except with the addition of Pump 3 at ω_{26} for case (a) and ω_{48} for case (c). (b) and (d) Corresponding absorption spectra showing dark-state profiles for the probe scanning across transitions ω_{26} and ω_{48}, respectively. Solid circles in the plots represent averaged data points obtained from a series of 7 scans and the error bars show standard deviations. Red solid lines are theoretical fits obtained from solving the eight-level master equation.

4.4(b) and (d), ground state decoherence times of 90 ns and 1.3 μs, respectively, are extracted. Compared to the estimated decoherence time of 2.5 ns due to thermally distributed nuclear fluctuations[1, 2, 3], these numbers correspond to extension of decoherence times by factors of 36 and 520. The difference in these values is likely due to the residual effects of DNSP caused by the scanning probe laser given that the actual Rabi frequency of Pump 3 is merely twice that of the probe.

4.4 Emergence of dark-state dips at singlet transitions: Nuclear spin narrowing

While the nonzero spin states $|T_-\rangle$ and $|T_+\rangle$ give rise to DNSP, the spin-zero singlet state does not since its contribution to the hyperfine interaction vanishes.

Therefore, the eigen-energy of the singlet state is unaffected by fluctuations in the Overhauser field. Nonetheless, the optical transitions from the singlet to the trion states are affected due to nonzero spins in the excited states. By tracing the resonance of singlet transitions, one can then extract information on the NSP. When the system is prepared in the singlet state following the scheme in Fig. 4.5(a) with Pump 3 blocked, the absorption spectrum of a weak probe scanned across transition ω_{18} shows a broadened lineshape (orange triangles in Fig. 4.5(b)) resembling a Voigt profile. This broadening is attributed to fluctuations in NSP and, subsequently, the Overhauser field. In experiment, the data acquisition time (4 s per data point) is expected to be much longer than the timescale of Overhauser field fluctuations. Therefore, each data point represents an averaged value derived from a distribution of Overhauser fields. To construct the numerical fit, the effect of nuclear spin fluctuations is treated the same way as in spectral diffusion, where the Overhauser field is assumed to be slowly varying compared to the optical processes. Calculated absorption spectra corresponding to different Overhauser fields are then averaged according to the best-fitting Overhauser field distribution. Some of these spectra, evaluated using 1 μs decoherence time, are shown in Fig. 4.5(d). Apparently, although each individual spectrum shows a dark-state dip, the averaging of different spectra obscures it, thus explaining its absence in the measurement. Assuming that the intrinsic Overhauser field has a Gaussian distribution, a numerically fitted standard deviation of 0.15 Tesla is obtained, in agreement with the theoretical order-of-magnitude estimate of 0.11 Tesla given in Appendix F.

With the application of Pump 3, the system is prepared in a coherent superposition of the singlet and $|T_+\rangle$ states via CPT. Due to a nonzero overall spin projection, DNSP ensues and its effects on the singlet transitions of ω_{18} is shown in Fig. 4.5(b) (hollow squares and circles). The dark-state dip now emerges with its depth enhanced as the intensity of Pump 3 is increased, resulting in spectra resembling CPT lineshapes. In addition, the overall linewidth is reduced. Both features above are reproduced in numerical simulation when narrowed Overhauser field distributions are assumed, as shown in Fig. 4.5(c). From the best-fit Overhauser field distributions, it is found that the higher the intensity of Pump 3, the narrower the distribution. Although the distribution can be further narrowed down, this occurs at the expense of the signal strength since the population of the singlet state is now being depleted, as can be seen from the peak heights in Fig. 4.5(b).

A more important effect of DNSP is revealed at the singlet transition of ω_{15}, which is not acted upon by Pump 3. A dark-state dip associated with the coherence

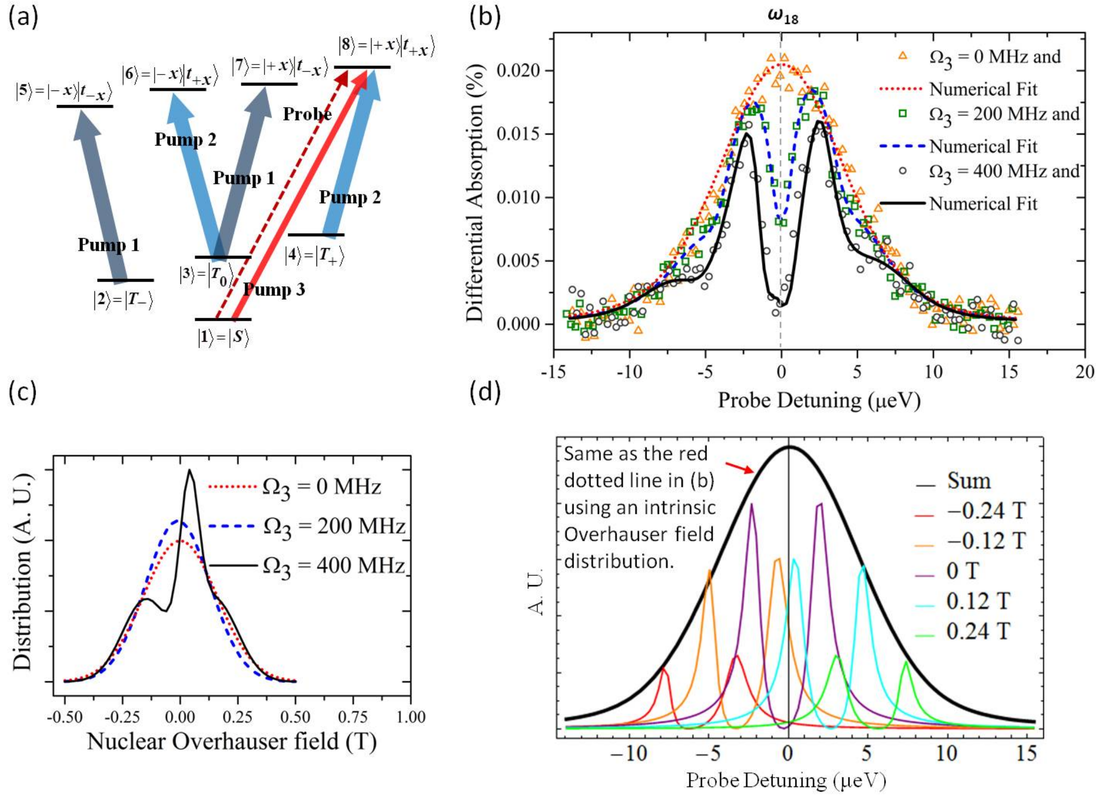

Figure 4.5: $|S\rangle$-$|T_+\rangle$ coherence and Overhauser field narrowing. (a) Pump configuration for the preparation of a coherent $|S\rangle$-$|T_+\rangle$ superposition. (b) Probe absorption spectra showing the emergence of dark-state dips at ω_{18} transition following the application of Pump 3. The spectra are taken with nominal Pump 3 intensities of 0 μW, 0.5 μW and 2.0 μW, corresponding to Rabi frequencies of about 0 MHz, 200 MHz and 400 MHz respectively. (c) Nuclear field distributions used in the numerical model for fitting the spectra in (b). (d) A schematic illustration explaining the disappearence of the dark-state dip due to averaging for the case without nuclear spin locking (Pump 3 blocked). The black curve is the weighted average of multiple colored curves (5 of them are shown) according to the intrinsic Overhauser field distribution (red dotted line in (c)).

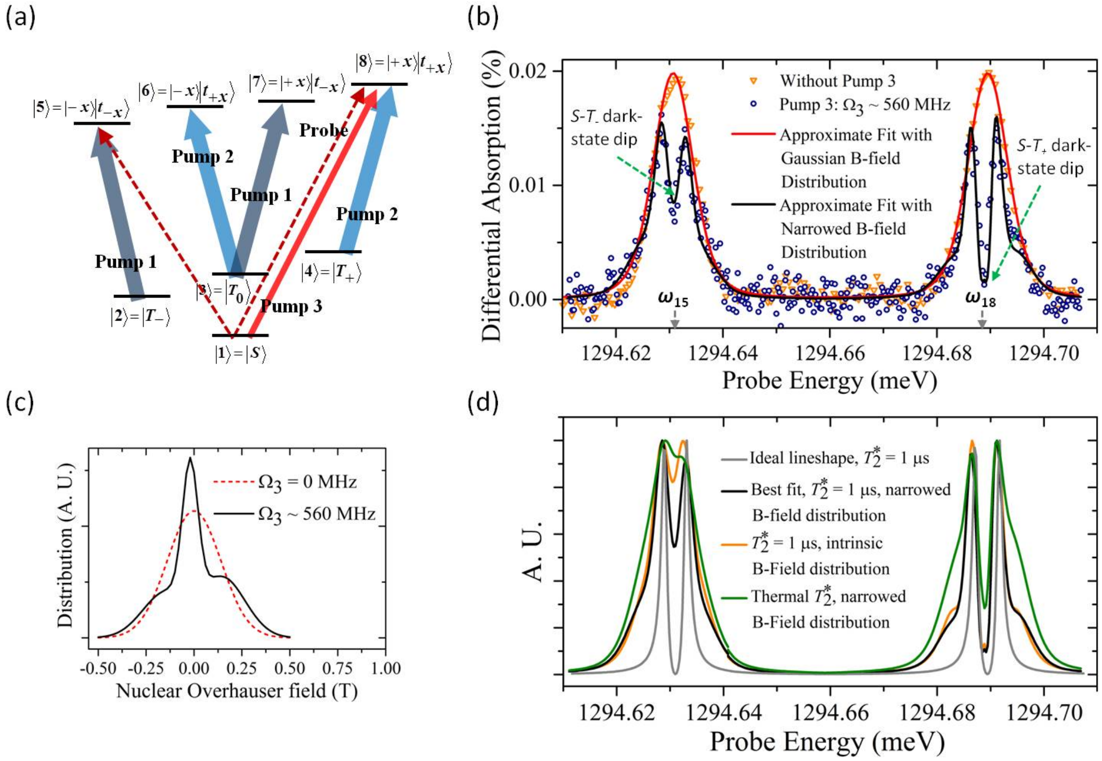

Figure 4.6: Dark-state dips at ω_{15} and ω_{18}. (a) The pump configuration here is similar to that shown in Fig. 4.5(a), but the probe is scanned across a wider range covering both singlet transitions. (b) Probe absorption spectra showing the emergence of dark-state dips at both singlet transitions, along with numerical fits. The Rabi frequency associated with Pump 3 is about 560 MHz. (c) Nuclear field distributions used in the numerical model for fitting the spectra in (b). (d) Comparison between spectra calculated from different combinations of dehonerence times and Overhauser field distributions. Here, the thermal value of decoherence time is assumed to be 2.5 ns[1, 2, 3].

between the singlet and $|T_-\rangle$ states now appears at ω_{15}, as shown in Fig. 4.6(b). A comparison between the two dark-state dips reveals that the one at ω_{18} is deeper than the other. This is due to the effect of Pump 3 which acts on ω_{18} and saturates the optical transition, a process related to hole burning in atomic vapors. Expectedly, when Pump 3 is tuned to the resonance of ω_{15}, the dip at ω_{15} becomes the deeper one. From theoretical calculations, a narrowed distribution of Overhauser field and long spin coherence of about 1 μs are necessary for the observation of the dark-state dip at ω_{15}. This is illustrated in Fig. 4.6(d) which shows several calculated lineshapes using different combinations of decoherence times and Overhauser field distributions. An approximate numerical fit using the narrowed Overhauser field distribution shown in

Fig. 4.6(c) and a decoherence time of 1μs is able to qualitatively reproduce all the essential features observed. The fact that this is achieved simultaneously for both singlet resonaces with a single set of fitting parameters suggests that the physical descriptions of the system provided here are well-grounded.

4.5 Conclusion and outlook

It is remarkable that the nuclear spin ensembles in two separate QDs can be stabilized simultaneously in the same manner as achieved in single QDs. The fact that all optical manipulations involve only the top QD lead us to the claim of non-local nuclear spin locking. This implies that the coupling between the two QDs remains efficient and robust in the presence of fluctuations of surrounding nuclear environment. The observation of long spin coherence involving all four two-electron spin eigenstates extends the applications of InAs QDMs to include the entire singlet-triplet manifold, where multiple two-qubit operations can be implemented within its decoherence time. Recently, it has been reported that suppressed spin fluctuations of a nuclear ensemble in an InAs QD persists beyond one second[22]. Therefore, for improved robustness, it might be advantageous to precede any two-qubit operation with the optical nuclear spin locking method discussed above[89].

On the other hand, the uniqueness of QDMs lies in the existence of a spin-zero singlet ground state that does not affect the NSP, while its corresponding optical transitions are sensitive to fluctuations in the Overhauser field. This can potentially serve as a tool for probing the dynamics of NSP. For instance, given sufficient signal to noise ratio and faster instrumentation, one might be able to trace the resonance of a singlet transition as a function of time. From this, the timescale of nuclear spin flip processes can be inferred. In addition, QDMs provide a platform for the investigation of potential coupling between two nuclear ensembles. This might prove useful for the fundamental study of mesoscopic entanglement as outlined by Schuetz et al.[90] Regardless, the work presented in this chapter suggests that a scalable architecture for quantum information processing composed of locally interacting QDs is feasible.

CHAPTER V

Towards a Universal Two-Qubit Gate

The observation of long two-electron spin coherence from the previous chapter establishes single QDMs as promissing platforms for the implementation of two-qubit operations. Since fast coherent manipulation of electron spins is typically required for gate operations, this chapter will begin with an introduction to the basics of pulsed laser excitation in QDMs. It is worth mentioning that picosecond pulses have been used in recent studies[87, 7] of InAs QDMs where coherent control of two-qubit states are being explored. In particular, as reported by Kim et al.[7], an all-optical two-qubit phase gate has been realized, using a QDM sample structure similar to the one used in this thesis. Even so, a universal two-qubit gate is still yet to be demonstrated.

In the original scheme proposed by Loss & DiVincenzo[91], a universal set of gates is achieved by modulating the strength of Coulomb exchange interaction between the two QDs. This has been realized in gate defined QDMs[92], albeit with a modest gate speed in the order of 10 MHz. In self-assembled QDMs, the presence of strong Coulomb exchange coupling means that high gate speed in the order of 10 GHz is possible. However, a low modulation depth together with the high speed required makes electrical gating of exchange interaction in self-assembled QDMs impractical. Instead, the recipe for realizing a universal two-qubit gate is learned from NMR[93], where a series of pulses resulting in single qubit rotations is applied, while the exchange interaction is kept constant. In the course of this chapter, it will be shown how picosecond pulses give rise to two-photon Raman transitions and subsequently single spin rotations. This, together with the Coulomb exchange interaction, constitutes the basis for the universality of two-qubit operations. A methodology for the readout of the populations of all four spin eigenstates will also be discussed.

5.1 Raman transitions with picosecond pulses: Single electron spin rotation

Previous chapters introduced coherent manipulation of the two-electron spin states using multiple *CW lasers*, which enables optical spin initialization and nuclear spin locking. As mentioned before, however, in order to implement a universal set of two-qubit operations, Raman transitions via pulsed excitations are required. Here in this section, the effects of picosecond pulses on the eight-level system are explored, from which the result shows adiabatic elimination of optical excited states and single spin rotation about the optical axis. These form the basis for two-qubit operations to be discussed in the next section.

In the previous chapter, the density matrix formalism was employed in the modeling of the eight level system under CW optical excitation. (See Appendix E). This choice is governed by the relevance of density matrix formalism in handling relaxations. Here, since the duration of the picosecond pulses is short compared to both the excited state lifetime and the spin decoherence time of about 2 ns and 1 μs, respectively, the effects of relaxation are unimportant. For simplicity, the amplitude picture is used in this section. An important assumption here is that the frequency bandwidth of the pulses is much larger than the spin splittings of the two-electron states. This is justified if one considers 2 ps pulses generated by Mira mode-locked Ti:Sapphire laser from Coherent Inc. Of which the frequency bandwidth is given by $TBP/\Delta t_p$, where TBP is the time-bandwidth product while Δt_p the FWHM pulse width. Assuming a Gaussian pulse shape with a TBP of 0.441 (0.315 for sech^2), the bandwidth is 221 GHz, or, equivalently, 0.92 meV. On the other hand, the largest spin splitting, given by that between the singlet and $|T_+\rangle$ states, is 0.153 meV in an applied magnetic field of 1.5 Tesla.

The optical field is defined as

$$\mathbf{E}\left(t\right)=\frac{1}{2}\left[\hat{x}E_x\left(t\right)+\hat{y}E_y\left(t\right)\right]e^{i\omega t}+c.c.$$

where ω is the center frequency of the pulses and *c.c.* represents complex conjugate. Assuming the dipole approximation holds, let us define the Rabi frequencies for the x- and y-polarized fields as

$$\Omega_x\left(t\right)=\frac{\mu E_x\left(t\right)}{\hbar}\quad\text{and}\quad\Omega_{iy}\left(t\right)=i\frac{\mu E_y\left(t\right)}{\hbar}$$

respectively. Here, μ is the dipole moment for transition ω_{25} which, ideally, is the same in magnitude as transitions ω_{26}, ω_{47} and ω_{48}. Note that $\Omega_{iy}(t)$ is defined as the quadrature component, as indicated by the factor i. By referring to Fig. 3.6 and using the rotating wave approximation, we can write the Hamiltonian of the eight-level system in field interaction picture as

$$\tilde{H} = \hbar \begin{bmatrix} \nu_1 & 0 & 0 & 0 & \frac{1}{2\sqrt{2}}\Omega_x(t) & \frac{1}{2\sqrt{2}}\Omega_{iy}(t) & -\frac{1}{2\sqrt{2}}\Omega_{iy}(t) & -\frac{1}{2\sqrt{2}}\Omega_x(t) \\ 0 & \nu_2 & 0 & 0 & \frac{1}{2}\Omega_{iy}(t) & \frac{1}{2}\Omega_x(t) & 0 & 0 \\ 0 & 0 & \nu_3 & 0 & \frac{1}{2\sqrt{2}}\Omega_x(t) & \frac{1}{2\sqrt{2}}\Omega_{iy}(t) & \frac{1}{2\sqrt{2}}\Omega_{iy}(t) & \frac{1}{2\sqrt{2}}\Omega_x(t) \\ 0 & 0 & 0 & \nu_4 & 0 & 0 & \frac{1}{2}\Omega_x(t) & \frac{1}{2}\Omega_{iy}(t) \\ \frac{1}{2\sqrt{2}}\Omega_x^*(t) & \frac{1}{2}\Omega_{iy}^*(t) & \frac{1}{2\sqrt{2}}\Omega_x^*(t) & 0 & \nu_5-\omega & 0 & 0 & 0 \\ \frac{1}{2\sqrt{2}}\Omega_{iy}^*(t) & \frac{1}{2}\Omega_x^*(t) & \frac{1}{2\sqrt{2}}\Omega_{iy}^*(t) & 0 & 0 & \nu_6-\omega & 0 & 0 \\ -\frac{1}{2\sqrt{2}}\Omega_{iy}^*(t) & 0 & \frac{1}{2\sqrt{2}}\Omega_{iy}^*(t) & \frac{1}{2}\Omega_x^*(t) & 0 & 0 & \nu_7-\omega & 0 \\ -\frac{1}{2\sqrt{2}}\Omega_x^*(t) & 0 & \frac{1}{2\sqrt{2}}\Omega_x^*(t) & \frac{1}{2}\Omega_{iy}^*(t) & 0 & 0 & 0 & \nu_8-\omega \end{bmatrix} \tag{5.1}$$

Here, ν_1 through ν_8 are similarly defined as in Appendix E. The probability amplitude in field interaction picture, denoted by $\mathbf{c}(t)$, is related to that in Schrödinger picture, $\mathbf{a}(t)$, by $\mathbf{c}(t) = \hat{U}(t)\,\mathbf{a}(t)$, where the unitary matrix $\hat{U}(t)$ is diagonal with elements $\{1, 1, 1, 1, e^{i\omega t}, e^{i\omega t}, e^{i\omega t}, e^{i\omega t}\}$. From the Hamiltonian above, the equations of motion for the probability amplitudes are given by

$$\begin{aligned}
\dot{c}_1(t) &= -i\left[-2\left|J_{ex}\right| c_1(t) + \frac{\Omega_x(t)}{2\sqrt{2}}c_5(t) + \frac{\Omega_{iy}(t)}{2\sqrt{2}}c_6(t) - \frac{\Omega_{iy}(t)}{2\sqrt{2}}c_7(t) - \frac{\Omega_x(t)}{2\sqrt{2}}c_8(t)\right] \\
\dot{c}_2(t) &= -i\left[-\delta_g c_2(t) + \frac{\Omega_{iy}(t)}{2}c_5(t) + \frac{\Omega_x(t)}{2}c_6(t)\right] \\
\dot{c}_3(t) &= -i\left[\frac{\Omega_x(t)}{2\sqrt{2}}c_5(t) + \frac{\Omega_{iy}(t)}{2\sqrt{2}}c_6(t) + \frac{\Omega_{iy}(t)}{2\sqrt{2}}c_7(t) + \frac{\Omega_x(t)}{2\sqrt{2}}c_8(t)\right] \\
\dot{c}_4(t) &= -i\left[\delta_g c_4(t) + \frac{\Omega_x(t)}{2}c_7(t) + \frac{\Omega_{iy}(t)}{2}c_8(t)\right] \\
\dot{c}_5(t) &= -i\left[(\Delta-\delta_a)\,c_5(t) + \frac{\Omega_x^*(t)}{2\sqrt{2}}c_1(t) + \frac{\Omega_{iy}^*(t)}{2}c_2(t) + \frac{\Omega_x^*(t)}{2\sqrt{2}}c_3(t)\right] \\
\dot{c}_6(t) &= -i\left[(\Delta-\delta_b)\,c_6(t) + \frac{\Omega_{iy}^*(t)}{2\sqrt{2}}c_1(t) + \frac{\Omega_x^*(t)}{2}c_2(t) + \frac{\Omega_{iy}^*(t)}{2\sqrt{2}}c_3(t)\right] \\
\dot{c}_7(t) &= -i\left[(\Delta+\delta_b)\,c_7(t) - \frac{\Omega_{iy}^*(t)}{2\sqrt{2}}c_1(t) + \frac{\Omega_{iy}^*(t)}{2\sqrt{2}}c_3(t) + \frac{\Omega_x^*(t)}{2}c_4(t)\right] \\
\dot{c}_8(t) &= -i\left[(\Delta+\delta_a)\,c_8(t) - \frac{\Omega_x^*(t)}{2\sqrt{2}}c_1(t) + \frac{\Omega_x^*(t)}{2\sqrt{2}}c_3(t) + \frac{\Omega_{iy}^*(t)}{2}c_4(t)\right]
\end{aligned} \tag{5.2}$$

where the detuning, Δ, and Zeeman splittings, δ_g, δ_a and δ_b are defined as follows:

$$\Delta = \omega_0 - \omega$$

$$\delta_g = \frac{\mu_B g_e B_x}{\hbar}, \qquad \delta_a = \tfrac{\mu_B B_x}{2\hbar}\left(g_e - 3g_h\right) \quad , \quad \delta_b = \frac{\mu_B B_x}{2\hbar}\left(g_e + 3g_h\right)$$

If we further define

$$\begin{aligned}
\tilde{c}_5\left(t\right) &= c_5\left(t\right) e^{i(\Delta-\delta_a)t} \\
\tilde{c}_6\left(t\right) &= c_6\left(t\right) e^{i(\Delta-\delta_b)t} \\
\tilde{c}_7\left(t\right) &= c_7\left(t\right) e^{i(\Delta+\delta_b)t} \\
\tilde{c}_8\left(t\right) &= c_8\left(t\right) e^{i(\Delta+\delta_a)t}
\end{aligned}$$

The last four equations in Eq. (5.2) can be rewritten as

$$\begin{aligned}
\dot{\tilde{c}}_5\left(t\right) &= -i\left[\frac{\Omega_x^*\left(t\right)}{2\sqrt{2}}c_1\left(t\right) + \frac{\Omega_{iy}^*\left(t\right)}{2}c_2\left(t\right) + \frac{\Omega_x^*\left(t\right)}{2\sqrt{2}}c_3\left(t\right)\right]e^{i(\Delta-\delta_a)t} \qquad (5.3)\\
\dot{\tilde{c}}_6\left(t\right) &= -i\left[\frac{\Omega_{iy}^*\left(t\right)}{2\sqrt{2}}c_1\left(t\right) + \frac{\Omega_x^*\left(t\right)}{2}c_2\left(t\right) + \frac{\Omega_{iy}^*\left(t\right)}{2\sqrt{2}}c_3\left(t\right)\right]e^{i(\Delta-\delta_b)t}\\
\dot{\tilde{c}}_7\left(t\right) &= -i\left[-\frac{\Omega_{iy}^*\left(t\right)}{2\sqrt{2}}c_1\left(t\right) + \frac{\Omega_{iy}^*\left(t\right)}{2\sqrt{2}}c_3\left(t\right) + \frac{\Omega_x^*\left(t\right)}{2}c_4\left(t\right)\right]e^{i(\Delta+\delta_b)t}\\
\dot{\tilde{c}}_8\left(t\right) &= -i\left[-\frac{\Omega_x^*\left(t\right)}{2\sqrt{2}}c_1\left(t\right) + \frac{\Omega_x^*\left(t\right)}{2\sqrt{2}}c_3\left(t\right) + \frac{\Omega_{iy}^*\left(t\right)}{2}c_4\left(t\right)\right]e^{i(\Delta+\delta_a)t}
\end{aligned}$$

Solving for $\tilde{c}_5\left(t\right)$, $\tilde{c}_6\left(t\right)$, $\tilde{c}_7\left(t\right)$ and $\tilde{c}_8\left(t\right)$ using integration by parts, we arrive at

$$\begin{aligned}
\tilde{c}_5\left(t\right) &= \frac{1}{\Delta-\delta_a}\left\{-\left[\frac{\Omega_x^*\left(t\right)}{2\sqrt{2}}c_1\left(t\right) + \frac{\Omega_{iy}^*\left(t\right)}{2}c_2\left(t\right) + \frac{\Omega_x^*\left(t\right)}{2\sqrt{2}}c_3\left(t\right)\right]e^{i(\Delta-\delta_a)t}\right. \qquad (5.4)\\
&\quad \left. + \int dt e^{i(\Delta-\delta_a)t}\frac{d}{dt}\left[\frac{\Omega_x^*\left(t\right)}{2\sqrt{2}}c_1\left(t\right) + \frac{\Omega_{iy}^*\left(t\right)}{2}c_2\left(t\right) + \frac{\Omega_x^*\left(t\right)}{2\sqrt{2}}c_3\left(t\right)\right]\right\}\\
\tilde{c}_6\left(t\right) &= \frac{1}{\Delta-\delta_b}\left\{-\left[\frac{\Omega_{iy}^*\left(t\right)}{2\sqrt{2}}c_1\left(t\right) + \frac{\Omega_x^*\left(t\right)}{2}c_2\left(t\right) + \frac{\Omega_{iy}^*\left(t\right)}{2\sqrt{2}}c_3\left(t\right)\right]e^{i(\Delta-\delta_b)t}\right.\\
&\quad \left. + \int dt e^{i(\Delta-\delta_b)t}\frac{d}{dt}\left[\frac{\Omega_{iy}^*\left(t\right)}{2\sqrt{2}}c_1\left(t\right) + \frac{\Omega_x^*\left(t\right)}{2}c_2\left(t\right) + \frac{\Omega_{iy}^*\left(t\right)}{2\sqrt{2}}c_3\left(t\right)\right]\right\}\\
\tilde{c}_7\left(t\right) &= \frac{1}{\Delta+\delta_b}\left\{\left[\frac{\Omega_{iy}^*\left(t\right)}{2\sqrt{2}}c_1\left(t\right) - \frac{\Omega_{iy}^*\left(t\right)}{2\sqrt{2}}c_3\left(t\right) - \frac{\Omega_x^*\left(t\right)}{2}c_4\left(t\right)\right]e^{i(\Delta+\delta_b)t}\right.\\
&\quad \left. + \int dt e^{i(\Delta+\delta_b)t}\frac{d}{dt}\left[-\frac{\Omega_{iy}^*\left(t\right)}{2\sqrt{2}}c_1\left(t\right) + \frac{\Omega_{iy}^*\left(t\right)}{2\sqrt{2}}c_3\left(t\right) + \frac{\Omega_x^*\left(t\right)}{2}c_4\left(t\right)\right]\right\}\\
\tilde{c}_8\left(t\right) &= \frac{1}{\Delta+\delta_a}\left\{\left[\frac{\Omega_x^*\left(t\right)}{2\sqrt{2}}c_1\left(t\right) - \frac{\Omega_x^*\left(t\right)}{2\sqrt{2}}c_3\left(t\right) - \frac{\Omega_{iy}^*\left(t\right)}{2}c_4\left(t\right)\right]e^{i(\Delta+\delta_a)t}\right.\\
&\quad \left. + \int dt e^{i(\Delta+\delta_a)t}\frac{d}{dt}\left[-\frac{\Omega_x^*\left(t\right)}{2\sqrt{2}}c_1\left(t\right) + \frac{\Omega_x^*\left(t\right)}{2\sqrt{2}}c_3\left(t\right) + \frac{\Omega_{iy}^*\left(t\right)}{2}c_4\left(t\right)\right]\right\}
\end{aligned}$$

For a large detuning, Δ, it is reasonable to assume that the Rabi frequencies and probability amplitudes are slowly varying compared to Δ, i. e.,

$$\begin{aligned} \left|\frac{d}{dt}\Omega_x\left(t\right)c_i\left(t\right)\right| &\ll \left|\Delta\Omega_x\left(t\right)c_i\left(t\right)\right| \text{ and} \\ \left|\frac{d}{dt}\Omega_{iy}\left(t\right)c_i\left(t\right)\right| &\ll \left|\Delta\Omega_{iy}\left(t\right)c_i\left(t\right)\right| \end{aligned}$$

In this case the integrals in Eq. (5.4) are small and can be neglected. We then obtain

$$\begin{aligned} c_5\left(t\right) &\approx -\frac{1}{\Delta-\delta_a}\left[\frac{\Omega_x^*\left(t\right)}{2\sqrt{2}}c_1\left(t\right)+\frac{\Omega_{iy}^*\left(t\right)}{2}c_2\left(t\right)+\frac{\Omega_x^*\left(t\right)}{2\sqrt{2}}c_3\left(t\right)\right] \\ c_6\left(t\right) &\approx -\frac{1}{\Delta-\delta_b}\left[\frac{\Omega_{iy}^*\left(t\right)}{2\sqrt{2}}c_1\left(t\right)+\frac{\Omega_x^*\left(t\right)}{2}c_2\left(t\right)+\frac{\Omega_{iy}^*\left(t\right)}{2\sqrt{2}}c_3\left(t\right)\right] \\ c_7\left(t\right) &\approx \frac{1}{\Delta+\delta_b}\left[\frac{\Omega_{iy}^*\left(t\right)}{2\sqrt{2}}c_1\left(t\right)-\frac{\Omega_{iy}^*\left(t\right)}{2\sqrt{2}}c_3\left(t\right)-\frac{\Omega_x^*\left(t\right)}{2}c_4\left(t\right)\right] \\ c_8\left(t\right) &\approx \frac{1}{\Delta-\delta_b}\left[\frac{\Omega_x^*\left(t\right)}{2\sqrt{2}}c_1\left(t\right)-\frac{\Omega_x^*\left(t\right)}{2\sqrt{2}}c_3\left(t\right)-\frac{\Omega_{iy}^*\left(t\right)}{2}c_4\left(t\right)\right] \end{aligned} \tag{5.5}$$

Substituting these into the first four equations in Eq. (5.5) and by $\Delta \gg \delta_a$, δ_b as mentioned above, we can write the equations of motion for the two-electron spin states in the form of an effective 4-level Hamiltonian as

$$H_{eff} \approx -\hbar\begin{bmatrix} \frac{2}{\hbar}J_{ex}+\Delta_S\left(t\right) & \frac{1}{\sqrt{2}}\Omega_{2e}\left(t\right) & 0 & -\frac{1}{\sqrt{2}}\Omega_{2e}\left(t\right) \\ \frac{1}{\sqrt{2}}\Omega_{2e}\left(t\right) & \delta_g+\Delta_S\left(t\right) & \frac{1}{\sqrt{2}}\Omega_{2e}\left(t\right) & 0 \\ 0 & \frac{1}{\sqrt{2}}\Omega_{2e}\left(t\right) & \Delta_S\left(t\right) & \frac{1}{\sqrt{2}}\Omega_{2e}\left(t\right) \\ -\frac{1}{\sqrt{2}}\Omega_{2e}\left(t\right) & 0 & \frac{1}{\sqrt{2}}\Omega_{2e}\left(t\right) & -\delta_g+\Delta_S\left(t\right) \end{bmatrix} \tag{5.6}$$

Here, the basis states consist of the two-electron subspace of the eight level system and are given by $\{|S\rangle, |T_-\rangle, |T_0\rangle, |T_+\rangle\}$. The diagonal term,

$$\Delta_S\left(t\right)=\frac{\left|\Omega_x\left(t\right)\right|^2+\left|\Omega_x\left(t\right)\right|^2}{4\Delta}$$

corresponds to the AC Stark shift, while the off-diagonal Raman term,

$$\Omega_{2e}\left(t\right)=\frac{\Omega_x^*\left(t\right)\Omega_{iy}\left(t\right)+c.c.}{4\Delta}$$

gives rise to the coupling between electron spin states. Hence, in the limit of a slowly varying temporal profile of the pulses and a large detuning, the excited state population is minimized and Raman transitions between optical ground states occur. This is known as the adiabatic elimination of the optical excited states. Note that in the effective Hamiltonian above, $|S\rangle$ and $|T_0\rangle$ are not coupled via the Raman pulses. This is because in deriving Eq. (5.6), we have made the simplification $\Delta \pm \delta_a \approx \Delta \approx \Delta \pm \delta_b$. In reality, however, nonzero values of δ_a and δ_b give rise to a small coupling term

$$\Omega_{S-T_0}(t) = \frac{1}{4}\left[|\Omega_x(t)|^2 \frac{\delta_a}{\Delta^2+\delta_a^2} + |\Omega_{iy}(t)|^2 \frac{\delta_b}{\Delta^2+\delta_b^2}\right]$$

that can bring about the Raman transition between $|S\rangle$ and $|T_0\rangle$ states.

To gain a better physical understanding of the effects of Raman pulses, it is insightful to write the effective Hamiltonian in Eq. (5.6) in a rotated basis defined as $H'_{eff} = \hat{U}' H_{eff} \hat{U}'^{\dagger}$ where

$$\hat{U}' = \begin{bmatrix} 0 & 0 & 0 & 1 \\ -\frac{1}{\sqrt{2}} & 0 & \frac{1}{\sqrt{2}} & 0 \\ \frac{1}{\sqrt{2}} & 0 & \frac{1}{\sqrt{2}} & 0 \\ 0 & 1 & 0 & 0 \end{bmatrix} \tag{5.7}$$

It is easy to verify that the operation of $\hat{U}'$ rotates the eigenstates into the *computational basis*: $\{|{+x}\rangle_B |{+x}\rangle_T, |{+x}\rangle_B |{-x}\rangle_T, |{-x}\rangle_B |{+x}\rangle_T, |{-x}\rangle_B |{-x}\rangle_T\}$. For clarity, subscripts B and T are introduced here to explicitly indicate electron wavefunctions predominantly localized in the bottom and top QDs, respectively. H'_{eff} is then given by

$$\begin{aligned} H'_{eff} &= -\hbar \begin{bmatrix} -\delta_g + \Delta_S(t) & \Omega_{2e}(t) & 0 & 0 \\ \Omega_{2e}(t) & \frac{1}{\hbar}J_{ex} + \Delta_S(t) & -\frac{1}{\hbar}J_{ex} & 0 \\ 0 & -\frac{1}{\hbar}J_{ex} & \frac{1}{\hbar}J_{ex} + \Delta_S(t) & \Omega_{2e}(t) \\ 0 & 0 & \Omega_{2e}(t) & \delta_g + \Delta_S(t) \end{bmatrix} \\ &= \frac{2}{\hbar^2}J_{ex}\hat{\mathbf{s}}_B \cdot \hat{\mathbf{s}}_T - 2\Omega_{2e}(t)\,\hat{s}_{T,z} + \frac{\mu_B g_e B_x}{\hbar}\left(\hat{s}_{B,x} + \hat{s}_{T,x}\right) - \left[\frac{1}{2}J_{ex} + \hbar\Delta_S(t)\right] \\ &= \frac{1}{2}J_{ex}\left(\hat{\boldsymbol{\sigma}} \otimes \hat{I}\right) \cdot \left(\hat{I} \otimes \hat{\boldsymbol{\sigma}}\right) - \hbar\Omega_{2e}(t)\left(\hat{I} \otimes \hat{\sigma}_1\right) + \frac{1}{2}\mu_B g_e B_x \left(\hat{\sigma}_3 \otimes \hat{I} + \hat{I} \otimes \hat{\sigma}_3\right) \\ &\quad - \left[\frac{1}{2}J_{ex} + \hbar\Delta_S(t)\right]\hat{I} \otimes \hat{I} \end{aligned} \tag{5.8}$$

where $\hat{\mathbf{s}}_B$ and $\hat{\mathbf{s}}_T$ denote spin operators for the electrons localized in the bottom and top QDs, respectively, while $\otimes$ represents tensor product. The terms in the last two lines correspond to the Heisenberg exchange interaction, pulsed Raman transition, Zeeman shift and a common energy shift, respectively, in the order of their appearance. To arrive at the last line, one needs to recall that the quantization axis is along the x-direction, so that

$$\begin{aligned}
\hat{s}_x &= \frac{\hbar}{2}\sigma_3 = \frac{\hbar}{2}\begin{bmatrix} 1 & 0 \\ 0 & -1 \end{bmatrix} \\
\hat{s}_z &= \frac{\hbar}{2}\sigma_1 = \frac{\hbar}{2}\begin{bmatrix} 0 & 1 \\ 1 & 0 \end{bmatrix} \\
\hat{s}_y &= -\frac{\hbar}{2}\sigma_2 = \frac{\hbar}{2}\begin{bmatrix} 0 & i \\ -i & 0 \end{bmatrix}
\end{aligned}$$

Eq. (5.8) above shows that the Raman term $\Omega_{2e}(t)$ couples $|+x\rangle_B|+x\rangle_T$ to $|+x\rangle_B|-x\rangle_T$, and also $|-x\rangle_B|+x\rangle_T$ to $|-x\rangle_B|-x\rangle_T$. In both cases, only the spin state of $|\pm x\rangle_T$ is affected. This means that the pulsed Raman transition here is essentially a single spin rotation about the optical axis (in z-direction) of the electron predominantly confined in the top QD. It is worth noting that this result is consistent with that of single QDs which allows fast spin manipulation for single qubit operations. In the following section, it will be revealed that the Hamiltonian in Eq. (5.8) forms the basis of a universal two-qubit gate.

5.2 An all-optical universal two-qubit gate in a QDM: Basic principles[1]

While the set of single-qubit operations belongs to the SU(2) group, two-qubit operations are elements of the SU(4) group and therefore can be conveniently represented by 4×4 unitary matrices up to a global phase. Any two-qubit operation can be classified[95, 96, 97, 98] either as a local gate, which belongs to the SU(2)⊗SU(2) subgroup, or a non-local gate, from the non-local, also known as the entangling, subgroup of SU(4)\[SU(2)⊗SU(2)]. Needless to say, the SU(2)⊗SU(2) subgroup comprises of single-qubit operations performed on each individual qubit in isolation. An entangling gate from the non-local subgroup, on the other hand, requires some kind of entanglement generating interaction between the two qubits. It has been proven that any entangling two-qubit operation combined with single-qubit rotations of any one of the two qubits can generate a set of universal two-qubit gates[99].

From the Hamiltonian in Eq. (5.8), it is clear that both the entangling operation and single-qubit rotations are provided by the exchange coupling and the pulsed

---

[1] See Ref. [94].

Raman term, together with the Zeeman interaction. A demonstration of the two-qubit universality in the context of self-assembled InAs QDMs is provided in Ref. [94] and is re-iterated here. Let us first look at the matrix representations of two-qubit operations. Up to a global phase, any 4×4 unitary matrix can be written as a linear combination of the 15 generators of SU(4), given by the set $\{\hat{\sigma}_i \otimes \hat{I},\ \hat{I} \otimes \hat{\sigma}_i,\ \left(\hat{\sigma}_i \otimes \hat{I}\right)\left(\hat{I} \otimes \hat{\sigma}_j\right)\}$, where $i, j = \{1, 2, 3\}$. Hence, for a system capable of generating a universal set of two-qubit operations, its time-evolution operator must contain all linear combinations of the 15 generators. For compactness, we will use the notations $\hat{\sigma}_{B,i} \equiv \hat{\sigma}_i \otimes \hat{I}$ and $\hat{\sigma}_{T,i} \equiv \hat{I} \otimes \hat{\sigma}_i$ in the following.

Let us consider a system described by the Hamiltonian in Eq. (5.8), re-written here as

$$\dot{\mathbf{c}} = -iH'\mathbf{c}$$

$$H' = H_0 + H_1(t)$$

where

$$\begin{aligned} H_0 &= \frac{1}{2}J'_{ex}\hat{\boldsymbol{\sigma}}_B \cdot \hat{\boldsymbol{\sigma}}_T + \frac{1}{2}\delta_g\left(\hat{\sigma}_{B,3} + \hat{\sigma}_{T,3}\right), \quad J'_{ex} = J_{ex}/\hbar \\ H_1(t) &= -\Omega_{2e}(t)\,\hat{\sigma}_{T,1} \end{aligned}$$

The term corresponding to a common energy shift of $-\left[\frac{1}{2}J_{ex} + \hbar\Delta_S(t)\right]$ is irrelevant to the discussion here and is therefore discarded. The time-evolution operator, $\hat{U}(t)$, of the system can be written in the form of Magnus expansion:

$$\begin{aligned} \hat{U}(t) &= \exp\Bigg(-i\int_0^t dt' H'(t') - \frac{1}{2!}\int_0^t dt' \int_0^{t'} dt'' \left[H'(t''), H'(t')\right] \qquad (5.9) \\ &- \frac{i}{3!}\int_0^t dt' \int_0^{t'} dt'' \int_0^{t''} dt''' \left\{\left[H'(t'''), \left[H'(t''), H'(t')\right]\right] + \left[\left[H'(t'''), H'(t'')\right], H'(t')\right]\right\} + \cdots\Bigg) \end{aligned}$$

The commutator appearing in the second order correction term can be expanded to give

$$\begin{aligned} \left[H'(t''), H'(t')\right] &= \left[H_0, H_1(t'')\right] + \left[H_1(t'), H_0\right] \qquad (5.10) \\ &= \frac{1}{2}\left[\Omega_{2e}(t') - \Omega_{2e}(t'')\right]\left[J'_{ex}\hat{\boldsymbol{\sigma}}_B \cdot \hat{\boldsymbol{\sigma}}_T + \delta_g\left(\hat{\sigma}_{B,3} + \hat{\sigma}_{T,3}\right), \hat{\sigma}_{T,1}\right] \\ &= i\left[\Omega_{2e}(t') - \Omega_{2e}(t'')\right]\left[J'_{ex}\left(\hat{\sigma}_{B,3}\hat{\sigma}_{T,2} - \hat{\sigma}_{B,2}\hat{\sigma}_{T,3}\right) + \delta_g\hat{\sigma}_{T,2}\right] \end{aligned}$$

Proceeding to the third order correction term, we have

$$\begin{aligned}\left[H'\left(t'''\right),\left[H'\left(t''\right),H'\left(t'\right)\right]\right] = 2\left[\Omega_{2e}\left(t'\right)-\Omega_{2e}\left(t''\right)\right]\Big\{\Omega_{2e}\left(t'''\right)\Big[J'_{ex}\left(\hat{\sigma}_{B,2}\hat{\sigma}_{T,2}+\hat{\sigma}_{B,3}\hat{\sigma}_{T,3}\right)+\delta_g\hat{\sigma}_{T,3}\Big]\\ +J'^{2}_{ex}\left(\hat{\sigma}_{T,1}-\hat{\sigma}_{B,1}\right)+\delta_g J'_{ex}\left(\hat{\sigma}_{B,3}\hat{\sigma}_{T,1}-\hat{\sigma}_{B,1}\hat{\sigma}_{T,3}\right)+\frac{1}{2}\delta_g^2\hat{\sigma}_{T,1}\Big\} \qquad (5.11)\end{aligned}$$

In Eq. (5.10), (5.11) and the first order term, H', 12 out of the 15 generators of SU(4) can be found. If one continues to evaluate the higher order terms, the remaining 3 generators, $\hat{\sigma}_{B,1}\hat{\sigma}_{T,2}$, $\hat{\sigma}_{B,2}\hat{\sigma}_{T,1}$ and $\hat{\sigma}_{B,2}$ will appear. Another way to reveal all 15 generators is by expanding the exponential form of the time-evolution operator into its power series. In the expansions above, the effective Rabi frequency for spin rotation, $\Omega_{2e}\left(t\right)$, has a time dependence corresponding to the applied Raman pulses. Therefore, it is in principle possible to generate any linear combination of the 15 generators of SU(4) by engineering the timing and amplitudes of the applied pulses.

In practice, an arbitrarily defined $\Omega_{2e}\left(t\right)$ can be implemented by using a sequence of picosecond pulses with varying intensity and temporal spacing. For convenience, let us assume a uniform temporal spacing of 60 ps, corresponding to a propagation delay of 18 mm in free space. The unitary operator after a sequence of k pulses $\{\Omega_{2e}\left(t_0\right), \Omega_{2e}\left(t_1\right), \cdots, \Omega_{2e}\left(t_{k-1}\right)\}$ can be approximated by

$$\hat{U}\left(t_k\right) \approx e^{-iH_0\tau_s}e^{-iH_1\left(t_{k-1}\right)\tau_p}\ldots e^{-iH_0\tau_s}e^{-iH_1\left(t_1\right)\tau_p}e^{-iH_0\tau_s}e^{-iH_1\left(t_0\right)\tau_p}$$

Here, τ_p and τ_s denote the temporal width and spacing of the picosecond pulses, respectively. Due to the fact that $\tau_p \ll \tau_s$, $\Omega_{2e}\left(t'\right)-\Omega_{2e}\left(t''\right)=0$ in most of the time except when $t', t'' = t_i$. Therefore, the higher order Magnus terms can be ignored. If we let $\hat{U}_T$ to represent the unitary matrix associated with the target two-qubit gate, the gate fidelity of $\hat{U}\left(t_k\right)$ can be crudely defined as

$$\frac{1}{N_i}\sum_i\left|\left\langle\Psi_i\right|\hat{U}_T^{\dagger}\hat{U}\left(t_k\right)\left|\Psi_i\right\rangle\right|^2$$

where the summation is taken over a number of input states, here given by the 4 spin eigenstates of the system. By varying the amplitudes of the pulses individually, the optimal pulse sequence corresponding to the highest gate fidelity can be numerically determined. One such pulse sequence is shown in Fig. 5.1(a) for the CNOT gate with a fidelity of 98 %. The corresponding populations of the four eigenstates for each input, also known as the "truth table", are given in Fig. 5.1(b). Here, the most important result lies in the total gate time of about 500 ps. Based on the estimate of T_2^* given in Chapter 4, about 1000 gate operations can be carried out within the spin coherence lifetime. In addition, assuming that the detuning, Δ, is chosen to be the pulse bandwidth of 0.92 meV, from the experimentally determined optical dipole moment, μ, of 0.086 μeV/$\sqrt{\mathrm{nW}}$, the average power needed for the pulse laser is estimated to be 6 mW. Therefore, the requirements for realizing a universal two-qubit gate are well within the capabilities of the instrumentation.

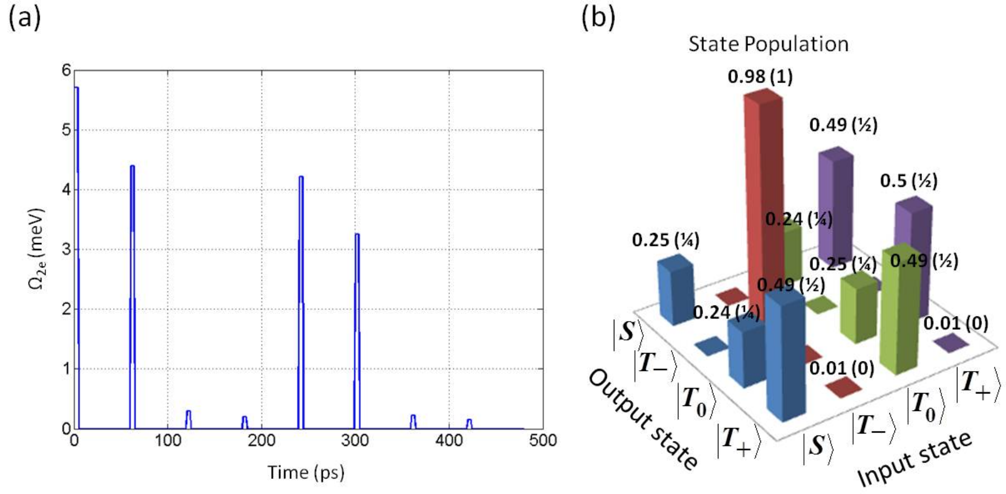

Figure 5.1: (a) Pulse sequence for implementing a CNOT gate using square pulses with pulse widths of 2 ps. J_{ex} and δ_g are assumed to be 120 μeV and 40 μeV, respectively. (b) Calculated truth table, i. e., state populations following the pulse sequence shown in (a) for each input eigenstates. Numbers in parenthesis are the populations of an ideal CNOT gate. Note that the singlet-triplet basis is used.

5.3 Optical readout of eigenstate populations

Having addressed the issues of spin initialization in Chapter 3 and optical spin manipulation in the previous section, the remaining challenge for the experimental demonstration of a two-qubit gate is the population readout of the eigenstates. For the purpose of characterizing a two-qubit operation, e. g., by performing quantum process tomography, it is imperative to be able to readout the population of all spin states individually. In single QDs, this can be accomplished simply by measuring the probe absorption. However, this is not the case in QDMs. As shown in Chapter 3, degeneracy in the optical transition frequencies precludes the measurement of individual spin states in the triplet manifold. As a result, the only eigenstate population that can be uniquely determined by probe absorption is that of the singlet state.

To overcome the difficulty in spin readout posed by the degeneracy, one can instead measure the rates of frequency resolved spontaneous emission following resonant excitations. It should be reminded that the measurements here are made in the basis consisting of singlet and triplet eigenstates. Conversion to the computational basis can be easily done using the unitary operator $\hat{U}'$ defined in Eq. (5.7). The measurement scheme is illustrated in Fig. 5.2 for the frequency resolved measurement of emitted photons at the resonance of ω_{35} and ω_{15}. Here, long excitation pulses of a few nanoseconds are used so that the bandwidth is sufficiently limited to avoid excitation of unintended transitions. A vertically polarized excitation pulse on resonance with transition ω_{25} excites the population from $|T_-\rangle$ to the excited state $|5\rangle$ and, simultaneously, from $|T_0\rangle$ to $|7\rangle$ due to the degeneracy. The detection of a horizontally polarized photon at ω_{35} signifies an event of spontaneous relaxation either from $|7\rangle$ to $|T_+\rangle$ or from $|5\rangle$ to $|T_0\rangle$, while a photon at ω_{15} corresponds to the relaxation from $|5\rangle$ to $|S\rangle$. As typically done in an experiment, a polarizer is placed after the sample in order to reject the excitation pulse. As a result, vertically polarized emissions are blocked and therefore are not considered here.

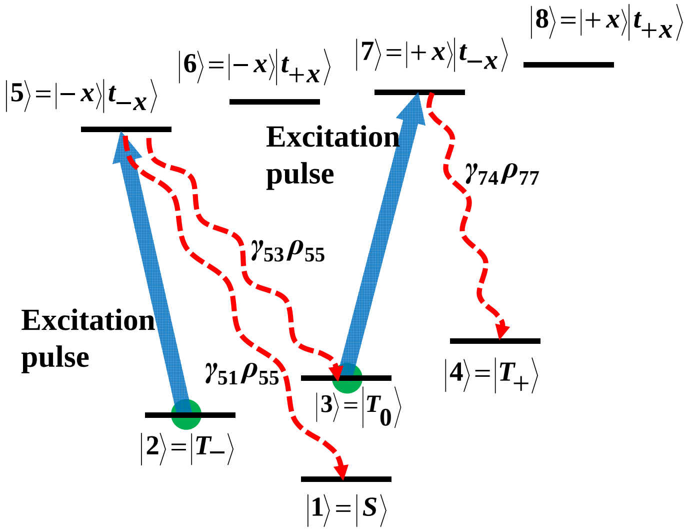

Figure 5.2: A schematic illustration of horizontally polarized spontaneous emissions following a vertically polarized excitation pulse on resonance with ω_{25}. Solid arrows represent excitation paths while wavy arrows spontaneous emission channels. Note that vertically polarized spontaneous emission channels are not shown as the emission is assumed to be blocked by a polarizer after the sample for the purpose of excitation beam rejection.

In the following discussion, let R_{ij} denotes the photon count rate measured within the optical linewidth of transition ω_{ij}, and γ_{kl} the spontaneous emission rate from state $|k\rangle$ to state $|l\rangle$. Using ρ_{ii} to represent the population of state $|i\rangle$, we can write

$$\begin{aligned} R_{35} = R_{47} &= \gamma_{53}\rho_{55} + \gamma_{74}\rho_{77} \\ &= \gamma_{53}\epsilon_{25}\rho_{22} + \gamma_{74}\epsilon_{37}\rho_{33} \end{aligned} \tag{5.12}$$

Here, ϵ_{ij} denotes the fraction of population being excited from state $|i\rangle$ to state $|j\rangle$ by the excitation pulse. For simplicity, the effect of optical pumping is ignored. However, if the duration of the excitation pulse is much longer than the excited state lifetime, optical pumping becomes important. This is because the population that ends up in $|T_0\rangle$ via the spontaneous decay channel of γ_{53} can be re-excited, thereby creating additional photon counts at ω_{47}. In this case, the correction term $\frac{\gamma_{53}}{\gamma_{53}+\gamma_{51}}\epsilon_{25}\rho_{22}$ should be added to the right hand side of Eq. (5.12). At ω_{15},

$$R_{15} = \gamma_{51}\rho_{55} = \gamma_{51}\epsilon_{25}\rho_{22} \tag{5.13}$$

Dividing Eq. (5.12) by (5.13), we have

$$\frac{R_{35}}{R_{15}} = 1 + 2\frac{\epsilon_{37}\rho_{33}}{\epsilon_{25}\rho_{22}}$$

Here, the ideal branching ratios of $\gamma_{53}/\gamma_{51} = 1$ and $\gamma_{74}/\gamma_{51} = 2$ are assumed. Nonetheless, it is important to point out that these values can be independently measured due to the fact that near unity initialization of states $|S\rangle$, $|T_-\rangle$ and $|T_+\rangle$ is possible, as discussed in Chapter 3. For example, to determine γ_{53}/γ_{51}, one simply prepares the system in the $|T_-\rangle$ state, then measures R_{35}/R_{15} with the same excitation pulse shown in Fig. 5.2. Assuming a unity excitation efficiency, i. e., $\epsilon_{ij} = 1$, then

$$\rho_{22} = \frac{2R_{15}}{R_{35} - R_{15}}\rho_{33} \tag{5.14}$$

Following the same derivation given above, but moving the excitation laser to the resonance of ω_{48}, we arrive at

$$\rho_{44} = \frac{2R_{18}}{R_{38} - R_{18}}\rho_{33} \tag{5.15}$$

Assuming that $\rho_{11} + \rho_{22} + \rho_{33} + \rho_{44} = 1$ holds, from Eq. (5.14) and (5.15), we obtain

$$\rho_{33} = (1 - \rho_{11})\left[1 + 2\left(\frac{R_{15}}{R_{35} - R_{15}} + \frac{R_{18}}{R_{38} - R_{18}}\right)\right]^{-1} \tag{5.16}$$

The population of the singlet state, ρ_{11}, can be independently measured by comparing the signal strength to the case where the system is initialized to the singlet state. Now, all state populations are given in terms of measurable quantities and can be individually determined from Eq. (5.14) to (5.16). It is worth mentioning that there are alternative spin readout procedures besides the one mentioned above. For example, if a circularly polarized excitation pulse is used, one can measure both horizontally and vertically polarized emissions. This then gives $\rho_{22}/\rho_{33} = R_{15}/R_{17}$ and $\rho_{44}/\rho_{33} = R_{18}/R_{16}$, assuming ideal excitation and branching ratios.

5.4 Proposed experimental demonstration of two-qubit gates

One of the easiest methods for demonstrating a two-qubit operation is by constructing a truth table which gives the measured populations of the four eigenstates as a function of input states as shown in Fig. 5.1(b). Combining the results from § 3.4, § 5.2 and § 5.3, here the processes of initialization, gate control and spin readout are incorporated into a proposed scheme for this purpose. The timing diagram for the optical pulses and the gated single photon counter is shown in Fig. 5.3, where the duration of each cycle is determined by the repetition rate of the pulsed laser. The long excitation pulses for initialization and readout are derived from CW lasers modulated with electro-optic modulators (EOMs). Although the duration of the initialization pulses is assumed to be 10 ns in Fig. 5.3, experimental results have shown that 4 ns suffices. For the picosecond gate pulses, a mode-locked Ti:Sapphire laser is used. For the two-qubit gate control, a pulse sequence can be created by passing the picosecond pulses through a beam splitter network, in which the amplitudes of individual pulses can be independently adjusted. Since the gate pulses are circularly polarized, it is preferable that the excitation lasers and the picosecond pulses are co-circularly polarized. In this way, they can all be rejected by a polarizer after the sample in order to prevent signal saturation or damage to the single photon counter.

Due to the constant presence of the Coulomb exchange interaction, the Bloch vector associated with the $S - T_0$ subspace continuously precesses about the axis defined by the singlet and $|T_0\rangle$ states. Consequentially, the operation of a two-qubit gate is only defined at the moment the system is being measured. However, if the measurement involves only the readout of population in the eigen-basis, the result will be less sensitive to the timing between the gate pulses and the readout pulse. Nonetheless, care should be taken in regard to the timing so that only photons emitted during the readout phase are registered. This can be achived by using a time-gated

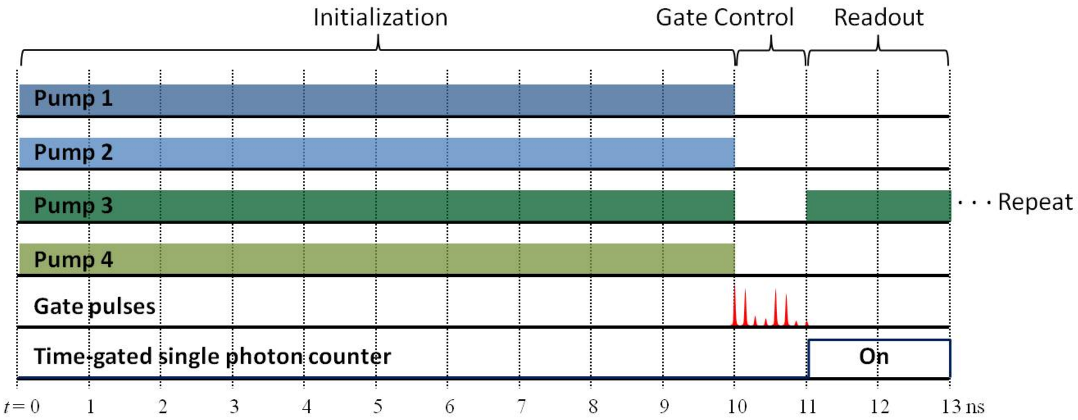

Figure 5.3: Timing diagram for the processes of initialization, gate control and readout of the two-qubit states. Here, the excitation lasers are configured to initialize the system to the $|T_0\rangle$ state, while the readout is intended for the singlet state. The frequencies of the excitation lasers are similar to the configuration shown Fig. 3.11.

single photon counter or a detector with a good timing resolution. Based on the lineshapes obtained in CW absorption measurements, an excited state spontaneous decay rate of about 500 MHz is inferred, as given in Appendix E. Therefore, a spin readout time of about 2 ns is recommended. As mentioned in the previous section, a much longer readout time may be used if one properly takes into account the effect of optical pumping.

Finally, from Chapter 4, we have seen that the hyperfine coupling between the electron spins and the nuclear spin ensemble can cause errors during the process of gate control. This is because one part of the Hamiltonian for the hyperfine coupling can be written in terms of an effective magnetic field arising from a non-zero nuclear spin polarization. The presence of this Overhauser field alters the precession frequency of the system about the quantization axis and may result in incorrect gate operations. Furthermore, the Overhauser field shifts the energy levels and complicates the processes that rely on careful detunings of the excitation lasers, e. g., initialization to the $|T_0\rangle$ state. Hence, it is desirable that the Overhauser field remains constant throughout the entire length of two-qubit gate demonstration. Therefore, it is important to interrupt the experiment at a regular interval to perform nuclear spin locking. Fortunately, it is likely that the lifetime of the nuclear spin polarization is very long, in the order of seconds, as observed in single QDs. The frequency of the interruption should be low enough that it can be executed between the acquisitions of each data point.

5.5 Conclusion

This chapter brings together many aspects of two-electron configuration in a QDM introduced earlier in an effort to show that the realization of a universal two-qubit gate is feasible. A large portion of this chapter is devoted to the theoretical groundwork for single spin rotations via pulsed Raman transitions. This, along with the inherent Coulomb exchange interaction, forms the basis for the universality of two-qubit operations in a QDM, thereby satisfying the DiVincenzo criterion requiring a universal set of gates. The development of multi-laser optical pumping technique for spin initialization and the observation of long spin decoherence time reported in Chapter 3 and 4, respectively, fulfill yet two more DiVincenzo criteria. The question concerning the measurement of individual quantum states is addressed in § 5.3. However, the procedure developed therein is yet to be demonstrated. If it is experimentally proven to be viable, we might then be able claim that the all five DiVincenzo criteria for a two qubit processor is fulfilled in a QDM.

CHAPTER VI

Summary and Future Directions

A large portion of this thesis is devoted to the theoretical descriptions of the QDM and, in particular, the two-electron configuration. The most important result is the eight-level system shown in Fig. 3.6. Based on which, a number of experiments are proposed and some of them have been demonstrated. These, along with other important findings, are summarized below.

6.1 Summary

Based on the simple energy band diagram of the QDM and by using the single-band-effective-mass model, the energy levels of an electron confined in a QDM can be calculated. When the energy levels are plotted with respect to applied bias, it is shown that they avoid crossing each other. This anti-crossing signifies coupling between the two QDs. With the addition of another electron, the QDM is now in the two-electron configuration. The Coulomb interaction between the two electrons not only shifts the energy levels but also gives rise to Heisenberg exchange interaction. As a result, the eigenstates of the two-electron configuration are given by the singlet and triplet states. The energy levels and the eigenstates can be determined by simply adding the Coulomb terms into the existing Hamiltonian. In a similar manner, the eigenstates of the $\mathcal{X}^{2-}$ configuration can also be found. Calculations showed that radiative decay from the $\mathcal{X}^{2-}$ states to the two-electron states produces a striking "X-pattern". This becomes the indicator of the two-electron configuration in the optical studies of QDMs.

For the demonstration of a two-qubit gate, it is advantageous to operate near the "sweet spot" in voltage bias. At this location, the energy levels of the two-electron states consist of the singlet state and the three-fold degenerate triplets. The optical excited states, however, behave as if the QDs are isolated, where an electron lies in the bottom QD while a trion is formed in the top QD. Due to the energy splitting between the singlet and triplet manifolds, optical pumping occurs at zero magnetic field. This serves as another indicator of the two-electron configuration. In a nonzero magnetic field in Voigt geometry, the degeneracy of the triplet states and of the optical excited states are lifted. The result, shown in Fig. 3.6, is an eight-level system with 12 optical transitions. Due to the degeneracy in transition frequencies, only a total of 8 distinct resonant frequencies are resolved. The eight-level model is experimentally verified by the fan diagram shown in Fig. 3.7.

In Voigt geometry, initialization of the spin state can be accomplished in the same manner as in single QDs. However, more than one pump laser is needed here. By using two pump lasers in various configurations, initialization to the singlet, $|T_+\rangle$ and $|T_-\rangle$ states has been demonstrated with initialization fidelities greater than 90 % . Notably, the multi-laser optical spin preparation technique used here is akin to the laser cooling process. For the case of the singlet state initialization, a spin temperature of 0.24 K is achieved, a remarkable decrease from the operating temperature of 6 K. The main drawback of the dual-laser optical pumping scheme lies in the fact that it cannot initialize the system to the $|T_0\rangle$ state due to the degeneracy in transition frequencies. Nonetheless, it is theoretically shown that initialization to the $|T_0\rangle$ state is possible with the application of four pump lasers. This four-laser optical spin preparation technique relies on the coherence of the spin state. From the absorption lineshapes observed, however, the coherence of the spin states appears to be affected by nuclear spim fluctuations of the underlying lattice. In the triplet manifold, this situation is excerbated by the process of dynamic nuclear spin polarization (DNSP).

Further studies in the absorption lineshapes reveal that DNSP is largely caused by the electron spins. This is corroborated by the fact that when the pump lasers are arranged in a configuration that induces coherent population trapping (CPT), a dark-state lineshape is recovered in the absorption profile of the weak probe laser. From the "DNSP-free" dark-state lineshapes, long spin coherence of about 1 μs can be extracted by fitting the lineshapes using the eight-level master equations. Similar analysis of the lineshapes associated with singlet transitions showed that the effects of nuclear spin fluctuations can be treated in the same way as spectral wandering. Furthermore, by holding a constant nonzero population in either the $|T_+\rangle$ or the $|T_-\rangle$ state via CPT, a narrowing in the Overhauser field distribution was observed. The significance of these results lies in the realization that the nuclear spin polarization in both QDs are stabilized while the optical excitation involves only the top QD. This demonstrates the effiect of non-local nuclear spin locking.

A theoretical study of the eight-level Hamiltonian showed that under pulsed excitation, detuned Raman transitions result in adiabatic elimination of the optical excited states and subsequently, single spin rotations of the electron confined in the top QD. This result has been verified in a recent study by Kim et al.[7]. Theoretically, single spin rotations and the Coulomb exchange interaction jointly constitute a universal two-qubit gate. The experimental demonstration of the two-qubit gate calls for a series of independently attenuated picosecond pulses which, according to theoretical calculations, is feasible in laboratory. One remaining component required for the experimental realization of a universal two-qubit gate is the readout of the spin states. This is also addressed theoretically, which showed that independent measurement of the populations of all four spin eigenstates is possible, given that frequency resolved single photon counting of spontaneous emission is used.

6.2 Future directions

Among numerous lines of research in QDMs, the most important task at hand is the demonstration of a universal two qubit gate. To achieve this goal, several components critical for the task need to be in place. Firstly, a robust methodology for spin readout needs to be established, of which a potentially feasible approach is discussed in § 5.3. The demonstration of this capability is crucial not only because it is an important element in the realization of gate operations, but also due to its use in characterizing the performance of other critical parts of the experiment. For example, it can be used to determine the initialization fidelity for the case of the $|T_0\rangle$ states, given that measuring the population of the $|T_0\rangle$ state independently is impossible with probe absorption.

Secondly, the initialization to the $|T_0\rangle$ state via coherent optical pumping as outlined in § 3.4 is also critical since it is necessary for the construction of the truth table. On the surface, this might seem straightforward, however, since the nature of the coupling between a *spin-1* $|T_0\rangle$ state and the nuclear spins is still unknown, complications might arise. Finally, a protocol for nuclear spin locking during the course of experiment needs to be developed so that interpretations of the results are not obscured by the effects of DNSP.

Beyond the confines of quantum gates, the mechanisms of various couplings between the QDM and its surroundings, such as the DNSP, are yet to be elucidated. It is well known that the decoherence of an electron spin is largely induced by the coupling between the electron and its nuclear environment. Other known mechanisms of decoherence include charge fluctuations in the vicinity of the QDs[7] and spin-orbit coupling in the form of Dzyaloshinski-Moriya interaction[100, 101]. Although the causes of spin decoherence is dominated by nuclear spin fluctuations, with a successful implementation of nuclear spin locking and a subsequent suppression of nuclear spin fluctuations, other sources of decoherence might surface. On the one hand, the understanding of these physical processes may guide us in improving the robustness of the quantum gates. On the other hand, it may be exploited for potential applications such as in quantum memory using nuclear spin ensembles[102].

It is important to keep in mind that despite the lengthy discussion presented, the scope of this thesis lies almost entirely within the two-electron configuration. The most important aspect of QDMs is that they provide us a variety of systems thanks to the existence of multiple charge configurations. Each of these configurations, owing to its uniqueness, gives rise to particular behaviors. One example is given by the "W-system[65]" arising from the anisotropic exchange (Dzyaloshinskii-Moriya) interaction in the single-electron or single-hole configuration. The presence of two "cycling transitions" in the outer arms of the W-system enables non-destructive readout of the electron spin state, while the middle Λ-system allows spin rotation via pulsed Raman transition. Besides being an integral part of quantum error correction, a cycling transition provides high measurement sensitivity that makes single shot readout possible. This feature is highly desirable in the implementations of protocols involving distant entanglement of spin qubits. In addition, a scalable architecture for quantum computation using W-systems has recently been proposed[27]. Therefore, a detailed experimental study of the W-system will be valuable for applications in quantum computation and communication.

Aside from the QDMs themselves, the integration of QDMs into photonic and electronic devices has also become an active area of research. In one recent study, QDMs have been integrated into photonic crystal cavities from which cavity-assisted Raman scattering and Purcell enhancement of inter-QD transitions have been observed[103]. Since the inter-QD transitions can be tuned over a wide spectral range by changing the applied bias, this system has the potential to serve as a frequency tunable single photon source. In another study, QDMs are embedded inside a fast field-effect device which is in turn encapsulated within a micro planar cavity[68]. This allows fast switching between intra-QD and inter-QD transitions and subsequently enables on-demand storage and retrieval of single photons. Evidently, the study of integrated QDM devices centers around controlling the interface between the QDMs and the outside world. Given the fact that the usefullness of a quantum gate largely relies on the effectiveness of its communication with the outside world, the integration of two-qubit operations with the additional degree of freedom provided by optical cavities seems to be another sensible area of study in the future.

APPENDICES

APPENDIX A

Comparison between Molecular Orbital Theory and Exact Solution in QDMs

The Molecular Orbital Theory (MOT) has been widely used in finding electronic wavefunctions of simple molecules, and is particularly successful in cases of diatomic molecules. In this appendix, the procedure outlined in Ref. [104] is applied to QDMs. The resulting eigen-energies are compared to exact solutions obtained from numerically solving the Schrödinger equation for a double-QD potential.

The potential function $V(\mathbf{r})$ used in the following analysis consists of QD potentials $V_1(\mathbf{r})$ and $V_2(\mathbf{r})$ associated with QDs 1 and 2 respectively, and a background $V_f(z)$ induced by a constant electric field in z-direction (See Fig. A.1). The origin of this electric field is discussed in the main text.

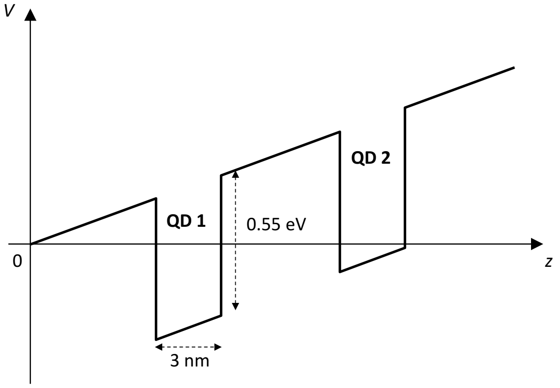

Figure A.1: Potential, $V(\mathbf{r})$, of the double-QD in z-direction

Let $\varphi_{1,i}(\mathbf{r})$ and $\varphi_{2,j}(\mathbf{r})$ be the electronic eigenfunctions associated with *single*-QDs

1 and 2 in isolation, i. e.

$$\left[\frac{\hat{\mathbf{p}}^2}{2m_e^*} + V_f(z) + V_1(\mathbf{r})\right]\varphi_{1,i}(\mathbf{r}) = E_{1,i}\varphi_{1,i}(\mathbf{r}), \text{ and}$$

$$\left[\frac{\hat{\mathbf{p}}^2}{2m_e^*} + V_f(z) + V_2(\mathbf{r})\right]\varphi_{2,j}(\mathbf{r}) = E_{2,j}\varphi_{2,j}(\mathbf{r})$$

Suppose that the double-QD wavefunction, $\Psi(\mathbf{r})$, can be written as a linear combination of single-QD states, we have

$$\Psi = \sum_{k,i} c_{k,i}|k,i\rangle, \text{ where } k = 1,2 \text{ and } i = 1,2,3,\ldots \tag{A.1}$$

Here, Dirac notation ($|1,i\rangle \equiv \varphi_{1,i}$ and $|2,j\rangle \equiv \varphi_{2,j}$) is used. Note that the basis set $\{|k,i\rangle\}$ is over-complete since for $k \neq l$, $\langle l,j|k,i\rangle \neq 0$ in general. By substituting Eq. A.1 into the Schrödinger equation for the double-QD potential, we get

$$\left(\frac{\hat{\mathbf{p}}^2}{2m_e^*} + V_f + V_1 + V_2\right)\sum_{k,i} c_{k,i}|k,i\rangle = E\sum_{k,i} c_{k,i}|k,i\rangle \tag{A.2}$$

After multiplying Eq. A.2 from the left by the bra $\langle l,j|$, we obtain the secular equation

$$\sum_{k,i}\left(\langle l,j|\frac{\hat{\mathbf{p}}^2}{2m_e^*} + V_f + V_1 + V_2 - E|k,i\rangle\right)c_{k,i} = 0 \tag{A.3}$$

One can rewrite Eq. A.3 in matrix form simply by using contracted index n and a map: $\{k,i\} \mapsto \{n\}$. Eq. A.3 then becomes

$$\sum_n (H_{mn} - ES_{mn})\,c_n = 0$$

where $H_{mn} = \langle m|\frac{\hat{\mathbf{p}}^2}{2m_e^*} + V_f + V_1 + V_2|n\rangle$ is the matrix elements for the double-QD Hamiltonian and $S_{mn} = \langle m|n\rangle$ is the overlap integral. Non-trivial solutions for the expansion coefficients c_n exist only if the secular determinant vanishes, i. e., $\det(H_{mn} - ES_{mn}) = 0$. As a simple illustration of how one can proceed from here, assume that QDM wavefunctions can be accurately simulated by superpositions of the ground states of individual QDs. In this case,

$$\Psi = c_{1,1}|1,1\rangle + c_{2,1}|2,1\rangle \tag{A.4}$$

Eq. A.3 is then reduced to

$$\sum_k \left(\langle l| \frac{\hat{\mathbf{p}}^2}{2m_e^*} + V_f + V_1 + V_2 - E \,|k\rangle \right) c_k = 0 \tag{A.5}$$

Here, indices $i, j = 1$ are dropped. Also,

$$\langle 1| \frac{\hat{\mathbf{p}}^2}{2m_e^*} + V_f + V_1 + V_2 \,|1\rangle = \langle 1| \frac{\hat{\mathbf{p}}^2}{2m_e^*} + V_f + V_1 \,|1\rangle + \langle 1| V_2 \,|1\rangle = E_1 + \langle 1| V_2 \,|1\rangle$$

$$\langle 1| \frac{\hat{\mathbf{p}}^2}{2m_e^*} + V_f + V_1 + V_2 \,|2\rangle = \langle 1| \frac{\hat{\mathbf{p}}^2}{2m_e^*} + V_f + V_2 \,|2\rangle + \langle 1| V_1 \,|2\rangle = E_2 S_{12} + \langle 1| V_1 \,|2\rangle$$

Similarly, $\langle 2| \frac{\hat{\mathbf{p}}^2}{2m_e^*} + V_f + V_1 + V_2 \,|2\rangle = E_2 + \langle 2| V_1 \,|2\rangle$ and $\langle 2| \frac{\hat{\mathbf{p}}^2}{2m_e^*} + V_f + V_1 + V_2 \,|1\rangle = E_1 S_{21} + \langle 2| V_2 \,|1\rangle$. In matrix form, Eq. A.5 becomes

$$\begin{bmatrix} \alpha_{11} - E & \beta_{12} - ES \\ \beta_{21} - ES^* & \alpha_{22} - E \end{bmatrix} \begin{bmatrix} c_1 \\ c_2 \end{bmatrix} = 0 \tag{A.6}$$

where $S = S_{12}$, $\alpha_{11} = E_1 + \langle 1| V_2 \,|1\rangle$, $\alpha_{22} = E_2 + \langle 2| V_1 \,|2\rangle$, $\beta_{12} = E_2 S + \langle 1| V_1 \,|2\rangle$ and $\beta_{21} = E_1 S^* + \langle 2| V_2 \,|1\rangle$. The off-diagonal term $\beta_{12} = \langle 1| \frac{\hat{\mathbf{p}}^2}{2m_e^*} + V_f + V_1 + V_2 \,|2\rangle = \langle 2| \frac{\hat{\mathbf{p}}^2}{2m_e^*} + V_f + V_1 + V_2 \,|1\rangle^* = E_1 \langle 2|1\rangle^* + \langle 2| V_2 \,|1\rangle^* = \beta_{21}^*$ is known as the tunneling coefficient. By setting the secular determinant of Eq. A.6 to zero and solving for E, we obtain the following:

$$E_\pm = \frac{1}{2\left(1 - |S|^2\right)} \Bigg[\alpha_{11} + \alpha_{22} - \beta_{12} S^* - \beta_{21} S \\ \mp \sqrt{\left(\alpha_{11} - \alpha_{22}\right)^2 + \left(\beta_{12} S^* - \beta_{21} S\right)^2 + 2\left(\alpha_{11} S - \beta_{12}\right)\left(\alpha_{22} S^* - \beta_{21}\right) + 2\left(\alpha_{11} S^* - \beta_{21}\right)\left(\alpha_{22} S - \beta_{12}\right)} \Bigg] \tag{A.7}$$

In the analyses of the energy level structure of QDMs presented in other literatures, it is often assumed that the explicit overlap integral, S, in Eq. A.6 is independent of the applied sample bias. In this limit, one obtains a simplified Schrödinger equation for QDMs[35, 38, 40, 42, 10]:

$$\begin{bmatrix} \alpha_{11} & s_t \\ s_t^* & \alpha_{22} \end{bmatrix} \begin{bmatrix} c_1 \\ c_2 \end{bmatrix} \equiv \hat{H} \,|\Psi\rangle = E \,|\Psi\rangle \tag{A.8}$$

where $s_t = \beta_{12} - \bar{E} S$ and $\bar{E} = \frac{1}{2\left(1 - |S|^2\right)} \left(\alpha_{11} + \alpha_{22} - \beta_{12} S^* - \beta_{21} S\right)$, evaluated at the "tunneling resonance", i. e., when $E_1 = E_2$.

To see how well the result from the MOT approximates the energy levels of a

QDM, consider a simplified case of two identical QDs separated by a verticle distance d, and let $V_f = 0$. By symmetry, S is real and $E_1 = E_2$. Also, $\alpha_{11} = \alpha_{22} = \alpha$ and $\beta_{12} = \beta_{21} = \beta$. The eigen-energies then become:

$$E_{\pm} = \frac{\alpha \pm \beta}{1 \pm S}$$

The corresponding normalized wavefunctions are

$$|\Psi_+\rangle = \frac{1}{\sqrt{2\,(1+S)}}\,(|1\rangle + |2\rangle) \text{ for } E_+ = \frac{\alpha+\beta}{1+S} \text{ and}$$

$$|\Psi_-\rangle = \frac{1}{\sqrt{2\,(1-S)}}\,(|1\rangle - |2\rangle) \text{ for } E_- = \frac{\alpha-\beta}{1-S}$$

The approximation of QDM wavefunctions using linear combinations of single-QD states is justified by looking at the exact solutions shown in Fig. A.2. The ground state of the QDM shows nonzero electron probability density everywhere within the inter-QD region. From the point of view of the MOT, this is the result of constructive interference between states $|1\rangle$ and $|2\rangle$. Using the terminology in molecular physics, this is known as the *bonding* state. On the other hand, the first excited state of the QDM shows a node where the probability density vanishes on the plane midway between QDs. This arises from destructive interference between states $|1\rangle$ and $|2\rangle$, and is called the *anti-bonding* state.

The eigen-energies as a function of inter-QD separation, d, are shown in Fig. A.3(a). The energy separation between the ground state and the first excited state widens with decreasing d due to increasing tunneling coefficient, β. At large d, the MOT is in good agreement with the exact solution. However, for d below 6 nm, significant deviation from the exact solution is observed. In this region, the assumption of Eq. A.4 becomes invalid and contribution from excited states of individual QDs cannot be ignored. This also imposes a limit on when Eq. A.8 is applicable.

When a nonzero electric field, F, is present, or when the QDs are non-identical, $E_1 \neq E_2$ and single-QD wavefunctions of both QDs must be found separately before one can use the MOT. However, for the former case with d large enough such that Eq. A.7 applies, we can write $E_2 \approx E_1 + ed'F$, assuming that the electric field is zero at the position of QD 1. Here e denotes the magnitude of elementary charge and d' the center-to-center distance between QDs. The resulting eigen-energies as a function of F are shown in Fig. A.3(b) for $d = 9$ nm. The energy levels consist of a field-independent horizontal line corresponding to the probability density centered

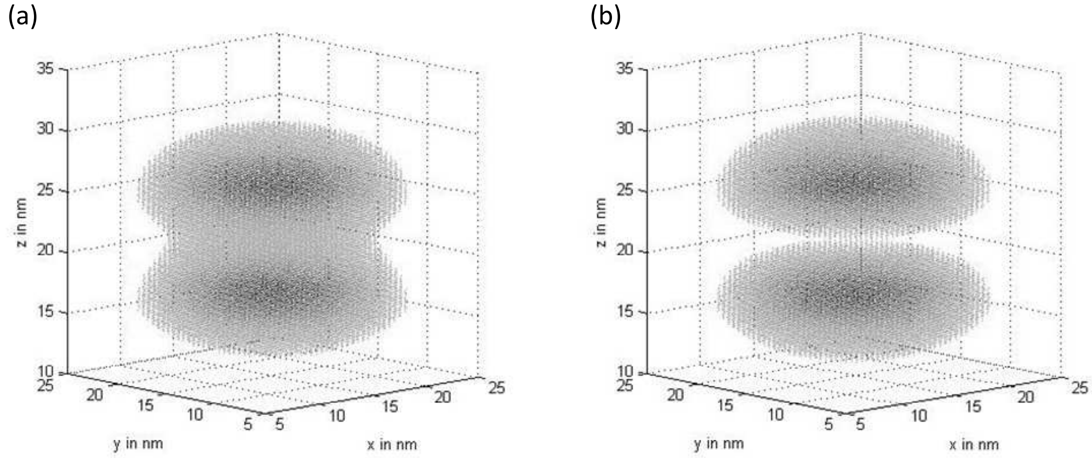

Figure A.2: Probability densities, $|\Psi|^2$, for (a) ground state and (b) first excited state of QDM. The QDs are in the shape of truncated cones with a 3 nm height and a 20 nm base diameter, with a 6 nm inter-QD separation. Wavefunctions are numerically calculated by solving the Schrödinger equation for the double-QD potential using Finite-Difference-Time-Domain(FDTD) method.

around QD 1, and a field-dependent line with a slope of ed' corresponding to the probability density centered around QD 2. An *anti-crossing* appears at the supposed intersection of these two lines at $F = 0$. This is where hybridization of individual QD wavefunctions occurs and is the tell-tale of molecular behavior. A simple model for this energy level structure is given by[38, 40, 42, 9, 10]:

$$\hat{H} = \begin{bmatrix} \alpha_{11} & s_t \\ s_t^* & \alpha_{22} + ed'F \end{bmatrix} \tag{A.9}$$

It is to be reminded that, as is discussed above, d must be sufficiently large to justify the use of this model, or, quantitatively, the condition $S \ll 1$ must be satisfied.

In summary, the MOT presents an alternative way of calculating envelop wavefunctions of QDM and is particularly useful for large inter-QD separation. However, when d is small, multiple single-QD wavefunctions need to be found beforehand. This is further complicated by the presence of asymmetry arises from the difference in QD sizes and the electric field. Nontheless, the choice of exact solution ("brute-force" method) or the MOT approximation is dependent on the calculation technique. For Finite-Difference-Time-Domain (FDTD) method (see Appendix B), the time needed to obtain the ground state solution is inversely proportional to the energy difference between the ground state and the first excited state. Therefore, for large d where

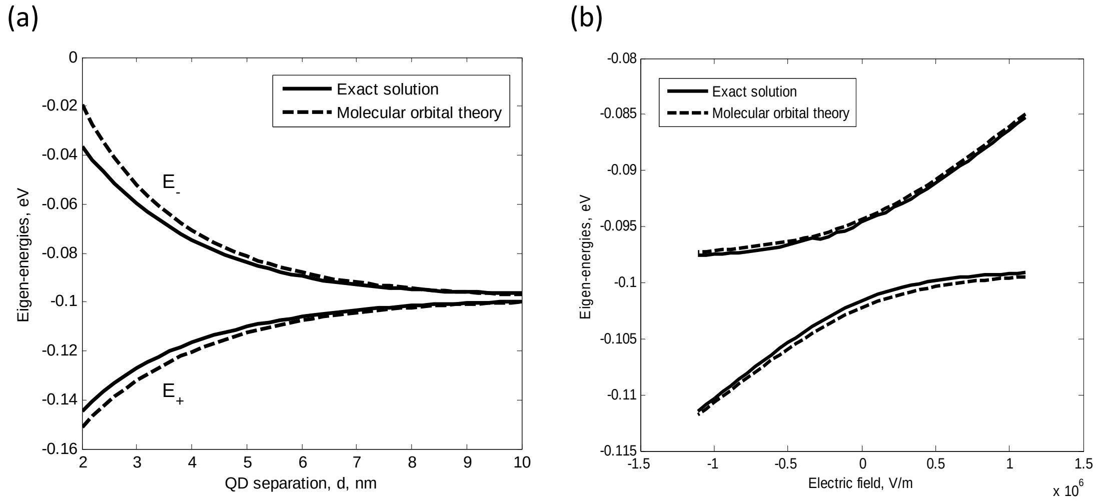

Figure A.3: Eigen-energies of the QDM from exact solutions (solid lines) and the MOT (dashed lines) as a function of (a) inter-QD separation, d, at $V_f = 0$ and (b) electric field, F, in z-direction at a fixed $d = 9$ nm

this energy difference is small, it is disadvantageous to use the “brute-force” method, since reasonable approximation can be obtained via the MOT. For small d, on the other hand, the brute-force method is straightforward, fast and accurate, making the MOT unfavorable in this regime.

APPENDIX B

Solving Schrödinger Equations With FDTD Method

This appendix reiterates the Finite-Difference-Time-Domain (FDTD) method of solving Schrödinger equations in coordinate representation as presented in Ref. [105]. A simple analysis of the rate of convergence towards the ground state solution is included at the end of this appendix.

We begin with the Schrödinger equation in coordinate representation:

$$i\hbar\frac{\partial}{\partial t}\Psi\left(\mathbf{r},t\right)=\left[-\frac{\hbar^2}{2m}\nabla^2+V\left(\mathbf{r}\right)\right]\Psi\left(\mathbf{r},t\right)$$

After making the substitution $it=\tau$ (Wick rotation), we have

$$\frac{\partial}{\partial\tau}\Psi\left(\mathbf{r},\tau\right)=\left[\frac{\hbar}{2m}\nabla^2-V_\hbar\left(\mathbf{r}\right)\right]\Psi\left(\mathbf{r},\tau\right),\text{ where }V_\hbar\left(\mathbf{r}\right)=\frac{V\left(\mathbf{r}\right)}{\hbar}\tag{B.1}$$

Note that this equation has the same form as the heat equation. Therefore, techniques developed for solving the heat equation can be directly applied to solve the Schrödinger equation. A common strategy is to begin by using a guess solution $\Psi'\left(\mathbf{r}\right)$. The functional form of $\Psi'\left(\mathbf{r}\right)$ is of little importance, but by completeness it can be represented as a linear combination of the basis states of corresponding time-independent Schrödinger equation, i. e.

$$\Psi'\left(\mathbf{r}\right)=\sum_{n=0}^{\infty}a_n\Phi_n\left(\mathbf{r}\right),\text{ where }\left[-\frac{\hbar^2}{2m}\nabla^2+V\left(\mathbf{r}\right)\right]\Phi_n\left(\mathbf{r}\right)=E_n\Phi_n\left(\mathbf{r}\right),\text{ and}$$

$$\Psi'(\mathbf{r},t) = \sum_{n=0}^{\infty} a_n \Phi_n(\mathbf{r})\, e^{-iE_n t/\hbar}$$

Applying the same Wick rotation to $\Psi'(\mathbf{r},t)$, we obtain

$$\Psi'(\mathbf{r},\tau) = \sum_{n=0}^{\infty} a_n \Phi_n(\mathbf{r})\, e^{-E_n \tau/\hbar} \tag{B.2}$$

If E_n is arranged such that $E_0 < E_1 < E_2 < \cdots$, for a sufficiently large τ, the expansion in Eq. B.2 is dominated by the $n = 0$ term, i. e.

$$\lim_{\text{large } \tau} \Psi'(\mathbf{r},\tau) \approx a_0 \Phi_0(\mathbf{r})\, e^{-E_0 \tau/\hbar}$$

$\Phi_0(\mathbf{r})$ is found by simply normalizing $\Psi'(\mathbf{r},\tau)$ at this τ. Eq. B.1 now provides an iterative method to arrive at $\Phi_0(\mathbf{r})$, starting with a guess solution $\Psi'(\mathbf{r})$. To obtain the wavefunction of the first excited state, $\Phi_1(\mathbf{r})$, one simply records the intermediate state $\Psi'(\mathbf{r},\tau-\Delta\tau)$ and estimates $\Phi_1(\mathbf{r})$ from the expression:

$$N\Phi_1(\mathbf{r}) \approx \Psi'(\mathbf{r},\tau-\Delta\tau) - \Phi_0(\mathbf{r}) \int d^3\mathbf{r}\; \Phi_0^*(\mathbf{r})\, \Psi'(\mathbf{r},\tau-\Delta\tau)$$

where N is a normalization constant. This bears resemblance to the Gram-Schmidt process and wavefunctions of higher excited states can be estimated in similar fashion.

To apply the idea discussed above using the numerical method, one needs to construct the potential function $V_\hbar(\mathbf{r})$ over a certain grid of points in space. The choice of grid pattern is a matter of convenience and here rectangular grid is used for its simplicity. The derivatives of the wavefunction in space can then be approximated by *finite differences*:

$$\frac{\partial}{\partial x_i}\Psi'(\mathbf{r},\tau) \approx \frac{\Psi'(\mathbf{r}+\Delta\vec{x}_i,\tau) - \Psi'(\mathbf{r},\tau)}{|\Delta\vec{x}_i|} \quad \text{and}$$

$$\frac{\partial^2}{\partial x_i^2}\Psi'(\mathbf{r},\tau) \approx \frac{\Psi'(\mathbf{r}+\Delta\vec{x}_i,\tau) - 2\Psi'(\mathbf{r},\tau) + \Psi'(\mathbf{r}-\Delta\vec{x}_i,\tau)}{|\Delta\vec{x}_i|^2}$$

These expressions are then substituted into Eq. B.1 to estimate the “time evolution” of $\Psi'(\mathbf{r},\tau)$ (hence the term *time domain*) iteratively. For better numerical stability, we take

$$V_\hbar(\mathbf{r})\, \Psi'(\mathbf{r},\tau) \approx \frac{1}{2} V_\hbar(\mathbf{r}) \left[\Psi'(\mathbf{r},\tau+\Delta\tau) + \Psi'(\mathbf{r},\tau)\right]$$

Using the following definitions:

$$\frac{\partial}{\partial \tau}\Psi'(\mathbf{r},\tau) \approx \frac{\Psi'(\mathbf{r},\tau+\Delta\tau)-\Psi'(\mathbf{r},\tau)}{\Delta\tau}$$

$$\hat{\mathbf{\Psi}} = \left[\begin{array}{ccc} \Psi'(x+\Delta x,y,z,\tau) & \Psi'(x,y,z,\tau) & \Psi'(x-\Delta x,y,z,\tau) \\ \Psi'(x,y+\Delta y,z,\tau) & \Psi'(x,y,z,\tau) & \Psi'(x,y-\Delta y,z,\tau) \\ \Psi'(x,y,z+\Delta z,\tau) & \Psi'(x,y,z,\tau) & \Psi'(x,y,z-\Delta z,\tau) \end{array}\right] \text{ and}$$

$$\mathbf{D}_1 = \frac{\hbar}{2m}\left[\begin{array}{c} 1 \\ -2 \\ 1 \end{array}\right], \text{ and } \mathbf{D}_2 = \left[\begin{array}{c} (\Delta x)^{-2} \\ (\Delta y)^{-2} \\ (\Delta z)^{-2} \end{array}\right],$$

we can rewrite Eq. B.1 as

$$\Psi'(x,y,z,\tau+\Delta\tau) = \frac{1}{A}\Delta\tau\left(\hat{\mathbf{\Psi}}\mathbf{D}_1\right)\cdot\mathbf{D}_2 + \frac{B}{A}\Psi'(x,y,z,\tau) \tag{B.3}$$

where $A = 1+\frac{\Delta\tau}{2}V_\hbar(x,y,z)$ and $B = 1-\frac{\Delta\tau}{2}V_\hbar(x,y,z)$. From Von Neumann numerical stability analysis, to ensure convergence to the ground state, $\Phi_0(\mathbf{r})$, the upper bound of $\Delta\tau$ is given by

$$\Delta\tau \leq \frac{1}{3}\frac{m}{\hbar}\min\left(\Delta x^2, \Delta y^2, \Delta z^2\right)$$

To find the minimum number of iterations needed, assume that $\Psi'(\mathbf{r},\tau=0) \approx a_0\Phi_0(\mathbf{r}) + a_1\Phi_1(\mathbf{r})$ and that $|a_0| \approx |a_1|$. From Eq. B.2, we have

$$\Psi'(\mathbf{r},\tau) \propto \left[\Phi_0(\mathbf{r}) + \Phi_1(\mathbf{r})e^{-\Delta E\tau/\hbar}\right]e^{-E_0\tau/\hbar} \text{ where } \Delta E = E_1 - E_0$$

The rate of convergence is then $e^{-\Delta E\Delta\tau/\hbar}$. Let $\Phi_0'(\mathbf{r}) = N\Psi'(\mathbf{r},\tau)$ where N is a normalization constant and define the error, ϵ, by

$$\epsilon = \sqrt{\int d\mathbf{r}\ \left|\Phi_0'(\mathbf{r}) - \Phi_0(\mathbf{r})\right|^2}$$

If we wish to achieve an error of less than one percent, then

$$\begin{aligned}
\epsilon &= \sqrt{\int d\mathbf{r}\ \left|\Phi_0'\left(\mathbf{r}\right)-\Phi_0\left(\mathbf{r}\right)\right|^2} \\
&= \sqrt{\int d\mathbf{r}\ \left|\frac{\Phi_0\left(\mathbf{r}\right)+e^{-\Delta E\tau/\hbar}\Phi_1\left(\mathbf{r}\right)}{\sqrt{1+e^{-2\Delta E\tau/\hbar}}}-\Phi_0\left(\mathbf{r}\right)\right|^2} \\
&\approx \sqrt{\int d\mathbf{r}\ \left|e^{-\Delta E\tau/\hbar}\Phi_1\left(\mathbf{r}\right)\right|^2} = e^{-\Delta E\tau/\hbar} < 0.01
\end{aligned}$$

Therefore, $\tau > 4.61\frac{\hbar}{\Delta E}$ and the minimum number of iterations required, n, is given by

$$n = \frac{\tau}{\Delta\tau} > 13.82\frac{\hbar^2}{m\Delta E}\frac{1}{\min\left(\Delta x^2, \Delta y^2, \Delta z^2\right)}$$

As mentioned in Appendix A, here it is shown that the time required to obtain the ground state wavefunction using the FTDT method is inversely proportional to the energy difference, ΔE. Other parameters affecting the calculation speed of this method include spatial step sizes (Δx_i) and the initial guess solution, $\Psi'\left(\mathbf{r}\right)$.

APPENDIX C

Basic Fermionic Algebra

This appendix reviews some basic algebraic manipulations involving fermionic operators. To begin, let us define the fermionic creation operator, $\hat{a}^\dagger$, as follows:

$$\hat{a}^\dagger(\alpha)\,|\varnothing\rangle = |\alpha\rangle\,; \qquad \hat{a}^\dagger(\beta)\,|\varnothing\rangle = |\beta\rangle$$

Here $|\varnothing\rangle \equiv |\mathrm{Vac}\rangle$ denotes the vacuum state while $|\alpha\rangle$ and $|\beta\rangle$ correspond to single particle quantum states for electron or hole. By a loose interpretation of the definition above, the creation operator with an argument of α generates a particle occupying state $|\alpha\rangle$ out of the vacuum state. The adjoint of the creation operator, given by $\left(\hat{a}^\dagger\right)^\dagger = \hat{a}$, is known as the annihilation operator. Fermionic operators obey the anti-commutation relations:

$$\left\{\hat{a}^\dagger(\alpha)\,,\hat{a}^\dagger(\beta)\right\} = \left\{\hat{a}(\alpha)\,,\hat{a}(\beta)\right\} = 0 \qquad \text{and} \qquad \left\{\hat{a}(\alpha)\,,\hat{a}^\dagger(\beta)\right\} = \delta_{\alpha,\beta} \tag{C.1}$$

where $\delta_{\alpha,\beta}$ is the Kronecker delta.

Setting $\alpha = \beta$, the anti-commutation relations above imply $\hat{a}^\dagger(\alpha)\,\hat{a}^\dagger(\alpha) = \hat{a}(\alpha)\,\hat{a}(\alpha) = 0$. Consequentially, the following is true for the number operator defined as $\hat{n}(\alpha) \equiv \hat{a}^\dagger(\alpha)\,\hat{a}(\alpha)$:

$$\hat{n}(\alpha)\left[1 - \hat{n}(\alpha)\right] = \hat{a}^\dagger(\alpha)\,\hat{a}(\alpha)\,\hat{a}(\alpha)\,\hat{a}^\dagger(\alpha) = 0$$

using $1 - \hat{n}(\alpha) = \hat{a}(\alpha)\,\hat{a}^\dagger(\alpha)$ from (C.1). This suggests that the only allowed eigenvalues of $\hat{n}$ are 0 or 1. Let us define the corresponding eigenstates as $|0\rangle_\alpha$ and $|1\rangle_\alpha$, i.

e., $\hat{n}(\alpha)|1\rangle_\alpha = |1\rangle_\alpha$ and $\hat{n}(\alpha)|0\rangle_\alpha = 0$ or $[1-\hat{n}(\alpha)]|0\rangle_\alpha = |0\rangle_\alpha$. We have

$$\hat{a}^\dagger(\alpha)|1\rangle_\alpha = \hat{a}^\dagger(\alpha)\hat{n}(\alpha)|1\rangle_\alpha = \hat{a}^\dagger(\alpha)\hat{a}^\dagger(\alpha)\hat{a}(\alpha) = 0 \tag{C.2}$$

$$\hat{a}(\alpha)|0\rangle_\alpha = \hat{a}(\alpha)[1-\hat{n}(\alpha)]|0\rangle_\alpha = \hat{a}(\alpha)\hat{a}(\alpha)\hat{a}^\dagger(\alpha) = 0 \tag{C.3}$$

Also,

$$[\hat{n}(\alpha)-0][\hat{a}(\alpha)|1\rangle_\alpha] = \hat{a}^\dagger(\alpha)\hat{a}(\alpha)\hat{a}(\alpha)|1\rangle_\alpha = 0, \text{ and}$$
$$[\hat{n}(\alpha)-1]\left[\hat{a}^\dagger(\alpha)|0\rangle_\alpha\right] = -\hat{a}(\alpha)\hat{a}^\dagger(\alpha)\hat{a}^\dagger(\alpha)|0\rangle_\alpha = 0$$

This implies

$$\hat{a}(\alpha)|1\rangle_\alpha = c|0\rangle_\alpha, \text{ and}$$
$$\hat{a}^\dagger(\alpha)|0\rangle_\alpha = c'|1\rangle_\alpha$$

where c and c' are some constants. After operating $\hat{a}^\dagger(\alpha)$ and $\hat{a}(\alpha)$ on both sides of the first and second equations above, respectively, we have

$$c\hat{a}^\dagger(\alpha)|0\rangle_\alpha = cc'|1\rangle_\alpha = \hat{a}^\dagger(\alpha)\hat{a}(\alpha)|1\rangle_\alpha = \hat{n}(\alpha)|1\rangle_\alpha = |1\rangle_\alpha \tag{C.4}$$

and

$$c'\hat{a}(\alpha)|1\rangle_\alpha = cc'|0\rangle_\alpha = \hat{a}(\alpha)\hat{a}^\dagger(\alpha)|0\rangle_\alpha = [1-\hat{n}(\alpha)]|0\rangle_\alpha = |0\rangle_\alpha \tag{C.5}$$

In both cases, we have $cc' = 1$ and for convenience, let $c = c' = 1$. This leads us to a closed, self-consistent algebraic structure for fermionic operators as shown below.

For a single particle state, take $|0\rangle_\alpha = |\varnothing\rangle$ and $|1\rangle_\alpha = |\alpha\rangle$. Combining Eq. (C.2), (C.3), (C.4) and (C.5), the operations of fermionic operators $\hat{a}^\dagger$ and $\hat{a}$ are summarized as follows:

$$\begin{array}{rcl} \hat{a}^\dagger(\alpha)|\varnothing\rangle &=& |\alpha\rangle \\ \hat{a}(\alpha)|\alpha\rangle &=& |\varnothing\rangle \\ \hat{a}^\dagger(\alpha)|\alpha\rangle &=& 0 \\ \hat{a}(\alpha)|\varnothing\rangle &=& 0 \end{array} \tag{C.6}$$

Note that the operations of $\hat{a}^\dagger(\alpha)$ and $\hat{a}(\alpha)$ are closed in the Hilbert space spanned by the vacuum state, $|\varnothing\rangle$, and the single "fermionic mode", $|\alpha\rangle$.

For two orthogonal wavefunctions, $\Psi_\alpha(\mathbf{r})$ and $\Psi_\beta(\mathbf{r})$, corresponding to fermionic modes $|\alpha\rangle$ and $|\beta\rangle$ respectively, we can define a two-particle state, $|\alpha,\beta\rangle$, as follows:

$$|\alpha,\beta\rangle = \hat{a}^\dagger(\beta)\hat{a}^\dagger(\alpha)|\varnothing\rangle = \hat{a}^\dagger(\beta)|\alpha\rangle \tag{C.7}$$

Equivalently, in coordinate representation, we write

$$\begin{aligned}
|\alpha,\beta\rangle \equiv \Psi_{\alpha,\beta}\left(\mathbf{r}_1,\mathbf{r}_2\right) &= \hat{\mathcal{A}}\Psi_\alpha\left(\mathbf{r}_1\right)\Psi_\beta\left(\mathbf{r}_2\right) \\
&= \tfrac{1}{\sqrt{2}}\begin{vmatrix} \Psi_\alpha\left(\mathbf{r}_1\right) & \Psi_\beta\left(\mathbf{r}_1\right) \\ \Psi_\alpha\left(\mathbf{r}_2\right) & \Psi_\beta\left(\mathbf{r}_2\right) \end{vmatrix} \\
&= \tfrac{1}{\sqrt{2}}\left[\Psi_\alpha\left(\mathbf{r}_1\right)\Psi_\beta\left(\mathbf{r}_2\right)-\Psi_\beta\left(\mathbf{r}_1\right)\Psi_\alpha\left(\mathbf{r}_2\right)\right] \\
&= \tfrac{1}{\sqrt{2}}\left(|\alpha\rangle_1\otimes|\beta\rangle_2-|\beta\rangle_1\otimes|\alpha\rangle_2\right)\equiv\tfrac{1}{\sqrt{2}}\left(|\alpha\rangle|\beta\rangle-|\beta\rangle|\alpha\rangle\right)
\end{aligned} \tag{C.8}$$

Here operator $\hat{\mathcal{A}}$ is known as the anti-symmetrizer. Eq. (C.8) shows multiple ways of representing the two-particle state of fermions, also called the "$\mathcal{H}_2$ block of the fermionic Fock space, $\mathcal{F}$". In the abbreviated notation of the last equation, the number indices are dropped since the identification of particles is understood from the ordering of the states. For an arbitrary number of electrons, n, the coordinate representation of the $\mathcal{H}_n$ block of fermionic Fock space is given by the Slater determinant:

$$\begin{aligned}
\Psi_{\alpha_1,\alpha_2,\cdots,\alpha_n}\left(\mathbf{r}_1,\mathbf{r}_2,\cdots,\mathbf{r}_n\right) &= \hat{\mathcal{A}}\Psi_{\alpha_1}\left(\mathbf{r}_1\right)\Psi_{\alpha_2}\left(\mathbf{r}_2\right)\cdots\Psi_{\alpha_n}\left(\mathbf{r}_n\right) \\
&= \tfrac{1}{\sqrt{n!}}\begin{vmatrix} \Psi_{\alpha_1}\left(\mathbf{r}_1\right) & \Psi_{\alpha_2}\left(\mathbf{r}_1\right) & \cdots & \Psi_{\alpha_n}\left(\mathbf{r}_1\right) \\ \Psi_{\alpha_1}\left(\mathbf{r}_2\right) & \Psi_{\alpha_2}\left(\mathbf{r}_2\right) & \cdots & \Psi_{\alpha_n}\left(\mathbf{r}_2\right) \\ \vdots & \vdots & \ddots & \vdots \\ \Psi_{\alpha_1}\left(\mathbf{r}_n\right) & \Psi_{\alpha_2}\left(\mathbf{r}_n\right) & \cdots & \Psi_{\alpha_n}\left(\mathbf{r}_n\right) \end{vmatrix}
\end{aligned}$$

Readers should take note of the order by which fermionic modes α and β appear in Eq. (C.7) and (C.8) due to the fact that interchanging α and β gives rise to a negative sign. Let us consider the following example: from the anti-commutation relations, Eq. (C.1), and Eq. (C.6), we have

$$\begin{aligned}
\hat{a}\left(\alpha\right)\hat{a}\left(\beta\right)|\alpha,\beta\rangle &= \hat{a}\left(\alpha\right)\hat{a}\left(\beta\right)\hat{a}^\dagger\left(\beta\right)\hat{a}^\dagger\left(\alpha\right)|\varnothing\rangle \\
&= -\hat{a}\left(\beta\right)\hat{a}\left(\alpha\right)\hat{a}^\dagger\left(\beta\right)\hat{a}^\dagger\left(\alpha\right)|\varnothing\rangle \\
&= \hat{a}\left(\beta\right)\hat{a}^\dagger\left(\beta\right)\hat{a}\left(\alpha\right)\hat{a}^\dagger\left(\alpha\right)|\varnothing\rangle = |\varnothing\rangle
\end{aligned}$$

However,

$$\begin{aligned}
\hat{a}\left(\beta\right)\hat{a}\left(\alpha\right)|\alpha,\beta\rangle &= \hat{a}\left(\beta\right)\hat{a}\left(\alpha\right)\hat{a}^\dagger\left(\beta\right)\hat{a}^\dagger\left(\alpha\right)|\varnothing\rangle \\
&= -\hat{a}\left(\beta\right)\hat{a}^\dagger\left(\beta\right)\hat{a}\left(\alpha\right)\hat{a}^\dagger\left(\alpha\right)|\varnothing\rangle = -|\varnothing\rangle
\end{aligned}$$

Consequentially,

$$\hat{a}\left(\alpha\right)\hat{a}\left(\beta\right)|\alpha,\beta\rangle = -\hat{a}\left(\beta\right)\hat{a}\left(\alpha\right)|\alpha,\beta\rangle = \hat{a}\left(\beta\right)\hat{a}\left(\alpha\right)|\beta,\alpha\rangle = |\varnothing\rangle$$

This implies $|\beta,\alpha\rangle = -|\alpha,\beta\rangle$, consistent with Eq. (C.8) and the anti-commutation relations.

For an n-particle state in general, we have $\left|\alpha_1^{'},\alpha_2^{'},\cdots,\alpha_n^{'}\right\rangle = (-1)^p\,|\alpha_1,\alpha_2,\cdots,\alpha_n\rangle$ where p is the order of permutation. This is easily seen using the definition

$$|\alpha_1,\alpha_2,\cdots,\alpha_n\rangle = \hat{a}^\dagger(\alpha_n)\cdots\hat{a}^\dagger(\alpha_2)\,\hat{a}^\dagger(\alpha_1)\,|\varnothing\rangle$$

and the commutation relations. For n =3 and 4, following identities can be derived easily:

$$\begin{aligned}
\hat{a}(\gamma)\,|\alpha,\beta,\gamma\rangle &= \;\;|\alpha,\beta\rangle\\
\hat{a}(\beta)\,|\alpha,\beta,\gamma\rangle &= -|\alpha,\gamma\rangle\\
\hat{a}(\alpha)\,|\alpha,\beta,\gamma\rangle &= \;\;|\beta,\gamma\rangle
\end{aligned}$$

$$\begin{aligned}
\hat{a}(\delta)\,|\alpha,\beta,\gamma,\delta\rangle &= \;\;|\alpha,\beta,\gamma\rangle\\
\hat{a}(\gamma)\,|\alpha,\beta,\gamma,\delta\rangle &= -|\alpha,\beta,\delta\rangle\\
\hat{a}(\beta)\,|\alpha,\beta,\gamma,\delta\rangle &= \;\;|\alpha,\gamma,\delta\rangle\\
\hat{a}(\alpha)\,|\alpha,\beta,\gamma,\delta\rangle &= -|\beta,\gamma,\delta\rangle
\end{aligned}$$

APPENDIX D

Schrieffer-Wolff Transformation in DNSP

Let us consider a Hamiltonian $H = H_0 + V$ consisting of the unperturbed term, H_0, and the perturbation term, V. The processs of Schrieffer-Wolff transformation begins with a unitary transformation $\tilde{H} = e^{\mathscr{S}} H e^{-\mathscr{S}}$ by a time-independent operator $\mathscr{S}$. A suitable choice of $\mathscr{S}$ then replaces V by the higher order terms of the perturbation, such that $\tilde{H} = H_0 + \tilde{V}^{(2)} + \tilde{V}^{(3)} + \cdots$ It is easy to show that in order to satisfy unitarity of $e^{\mathscr{S}}$, $\mathscr{S}$ must be an anti-Hermitian operator, i. e., $\mathscr{S}^\dagger = -\mathscr{S}$. To understand the relevance of Schrieffer-Wolff transformation in DNSP, let us consider an example using the Hamiltonian

$$\begin{aligned} H &= H_e^{\text{Zee}} + H_n^{\text{Zee}} + H_{e-n}^{\text{FC}} \\ &= \frac{g_e \mu_B}{\hbar} \widehat{\mathbf{S}} \cdot \mathbf{B} - \frac{\mu_N}{\hbar} \sum_i g_{n,i} \widehat{\mathbf{I}}_i \cdot \mathbf{B} + \sum_i A_{e,i} \widehat{\mathbf{S}} \cdot \widehat{\mathbf{I}}_i \end{aligned} \tag{D.1}$$

The first and second terms are the Zeeman interaction for electron and nuclei, respectively, while the third is known as the Fermi-contact hyperfine interaction, as given in Chapter 4. Taking the x-direction as the quantization axis, let us use the definition $\hat{S}_\pm = \hat{S}_z \mp i\hat{S}_y$, $\hat{I}_{i,\pm} = \hat{I}_{i,z} \mp i\hat{I}_{i,y}$ and $B_\pm = B_z \mp iB_y$ to rewrite Eq. (D.1) as

$$\begin{aligned} H &= \frac{g_e \mu_B}{\hbar} \left[\hat{S}_x B_x + \frac{1}{2} \left(\hat{S}_+ B_- + \hat{S}_- B_+ \right) \right] - \frac{\mu_N}{\hbar} \sum_i g_{n,i} \left[\hat{I}_{i,x} B_x + \frac{1}{2} \left(\hat{I}_{i,+} B_- + \hat{I}_{i,-} B_+ \right) \right] \\ &\quad + \sum_i A_{e,i} \left[\hat{S}_x \hat{I}_{i,x} + \frac{1}{2} \left(\hat{S}_+ \hat{I}_{i,-} + \hat{S}_- \hat{I}_{i,+} \right) \right] \\ &= H_0 + \frac{1}{2} \sum_i A_{e,i} \left(\hat{S}_+ \hat{I}_{i,-} + \hat{S}_- \hat{I}_{i,+} \right) \end{aligned} \tag{D.2}$$

where in the last equation, we let

$$H_0 = H_e^{\mathrm{Zee}} + H_n^{\mathrm{Zee}} + \sum_i A_{e,i}\hat{S}_x\hat{I}_{i,x}$$

Although it is not obvious in Eq. (D.2), the electron-nuclear spin flip-flop term given by $H' = \frac{1}{2}\sum_i A_{e,i}\left(\hat{S}_+\hat{I}_{i,-} + \hat{S}_-\hat{I}_{i,+}\right)$ gives rise to nuclear spin diffusion across the QD, when mediated by the electron spin. To see this, consider the product state $\left|\uparrow^e\right\rangle\cdots\left|\downarrow_i^n\right\rangle\left|\uparrow_j^n\right\rangle\cdots$ where the superscripts e and n indicate electron and nuclear spins, respectively. Successive operations of H' lead to the sequence

$$\left|\uparrow^e\right\rangle\cdots\left|\downarrow_i^n\right\rangle\left|\uparrow_j^n\right\rangle\cdots \quad \overset{H'}{-\!-\!-\!\rightarrow} \quad \left|\downarrow^e\right\rangle\cdots\left|\uparrow_i^n\right\rangle\left|\uparrow_j^n\right\rangle\cdots \quad \overset{H'}{-\!-\!-\!\rightarrow} \quad \left|\uparrow^e\right\rangle\cdots\left|\uparrow_i^n\right\rangle\left|\downarrow_j^n\right\rangle$$

implying that the spin states of i-th and j-th nucleus are swapped via an intermediate state $\left|\downarrow^e\right\rangle\cdots\left|\uparrow_i^n\right\rangle\left|\uparrow_j^n\right\rangle\cdots$ This electron mediated nuclear spin diffusion process can be cast in a more explicit algebraic form following Schrieffer-Wolff transformation.

To begin, note that $\tilde{H} = e^{\mathscr{S}}He^{-\mathscr{S}}$ can be expanded into a power series using the Baker-Campbell-Hausdorff formula:

$$\tilde{H} = e^{\mathscr{S}}He^{-\mathscr{S}} = H + [\mathscr{S}, H] + \frac{1}{2!}[\mathscr{S},[\mathscr{S},H]] + \frac{1}{3!}[\mathscr{S},[\mathscr{S},[\mathscr{S},H]]] + \cdots \tag{D.3}$$

If we let

$$\mathscr{S} = \frac{1}{B_x}\sum_i c_i\left(\hat{S}_+\hat{I}_{i,-} - \hat{S}_-\hat{I}_{i,+}\right),\ c_i = \frac{\hbar A_{e,i}}{2\left(\mu_B g_e + \mu_N g_{n,i}\right)}$$

then it can be shown that

$$\left[\mathscr{S}, H_e^{\mathrm{Zee}} + H_n^{\mathrm{Zee}}\right] = H_\perp^{\mathrm{FC}} - H'$$

where

$$H_\perp^{\mathrm{FC}} \ = \ \sum_i c_i\left[\mu_B g_e\hat{S}_x\left(\frac{B_-}{B_x}\hat{I}_{i,+} + \frac{B_+}{B_x}\hat{I}_{i,-}\right) + \mu_N g_{n,i}\left(\frac{B_-}{B_x}\hat{S}_+ + \frac{B_+}{B_x}\hat{S}_-\right)\hat{I}_{i,x}\right]$$

Substituting this into Eq. (D.3), we arrive at

$$\tilde{H} = H_0 + H_\perp^{\mathrm{FC}} + \left[\mathscr{S}, \sum_i A_{e,i}\hat{S}_x\hat{I}_{i,x}\right] + \frac{1}{2}\left[\mathscr{S}, H' + H_\perp^{\mathrm{FC}}\right] + \cdots \tag{D.4}$$

by keeping only terms upto second order in $A_{e,i}$. For an applied magnetic field in

x-direction, $H_{\perp}^{\mathrm{FC}} = 0$. After expanding the commutators in Eq. (D.4), we obtain

$$\begin{aligned}
\tilde{H} &= H_0 + \tilde{V}^{(2)} + \cdots \\
&= H_0 + \frac{1}{2}\sum_{i,j}\frac{A_{e,i}c_j}{B_x}\left[\hat{S}_x\left(\hat{I}_{i,-}\hat{I}_{j,+} + \hat{I}_{i,+}\hat{I}_{j,-}\right) + \frac{1}{2}\left(\hat{S}_-\hat{S}_+\hat{I}_{i,-}\hat{I}_{j,+} + \hat{S}_+\hat{S}_-\hat{I}_{i,+}\hat{I}_{j,-}\right)\right] \\
&\quad - \sum_{i,j}\frac{A_{e,i}c_j}{B_x}\left(\hat{S}_+\hat{I}_{i,-} + \hat{S}_-\hat{I}_{i,+}\right)\hat{I}_{j,x} - \sum_i \frac{A_{e,i}c_i}{B_x}\hat{S}_x\left(\hat{S}_+\hat{I}_{i,-} + \hat{S}_-\hat{I}_{i,+}\right) + \cdots
\end{aligned}$$

Evidently, the first term in $\tilde{V}^{(2)}$ describes the process of electron mediated nuclear spin diffusion. The other two terms involve the spin flip-flop between an electron and a nucleus. In large magnetic fields, these flip-flop terms can be ignored due to energy conservation[3].

As mentioned in Chapter 4, the addition of electric nuclear quadrupolar interaction gives rise to the non-collinear hyperfine term. The quadrupolar interaction is given by

$$H^{\mathrm{Q}} = -\frac{1}{2}\sum_{\alpha\beta}\hat{Q}_{\alpha\beta}\frac{\partial^2}{\partial\alpha\partial\beta}V_e(\mathbf{r}),\ \alpha,\beta = \{x,y,z\}$$

where $V^e(\mathbf{r})$ is the electrostatic potential and $\hat{Q}_{\alpha\beta}$ is defined as

$$\hat{Q}_{\alpha\beta} = \frac{|Q|}{I(2I-1)}\left[\frac{1}{2}\left(I_\alpha I_\beta + I_\beta I_\alpha\right) - \frac{\delta_{\alpha\beta}}{3}I(I+1)\right]$$

Here, $|Q| = 3\int d\mathbf{r}\left(x^2 - \frac{1}{3}r^2\right)\rho_n(\mathbf{r})$ and $\rho_n(\mathbf{r})$ is the nuclear charge density. Assuming that the electric field gradient $\frac{\partial^2}{\partial\alpha\partial\beta}V^e(\mathbf{r})$ is traceless, i. e., satisfying the Laplace's equation, which means that no other charge is present within the spatial extend of the nuclear wavefunction, H^{Q} can be written in spherical coordinates

$$H^{\mathrm{Q}} = -\frac{1}{3}\sum_k \hat{Q}_k^{(2)}V_k^{(2)}(\mathbf{r})$$

with $\hat{Q}_k^{(2)}$ and $V_k^{(2)}$ defined as

$$
\begin{aligned}
\hat{Q}_0^{(2)} &= \frac{|Q|}{2I\left(2I-1\right)}\left[3\hat{I}_x^2 - I(I+1)\right] \\
\hat{Q}_{\pm 1}^{(2)} &= \mp\frac{\sqrt{6}\,|Q|}{4I\left(2I-1\right)}\hat{I}_\pm\left(2\hat{I}_x \pm 1\right) \\
\hat{Q}_{\pm 2}^{(2)} &= \frac{\sqrt{6}\,|Q|}{4I\left(2I-1\right)}\hat{I}_\pm^2 \\
V_0^{(2)} &= \frac{3}{2}\frac{\partial^2}{\partial x^2}V^e\left(\mathbf{r}\right) \\
V_{\pm 1}^{(2)} &= \mp\frac{\sqrt{6}}{2}\frac{\partial}{\partial x}\left(\frac{\partial}{\partial z} \mp i\frac{\partial}{\partial y}\right)V^e\left(\mathbf{r}\right) \\
V_{\pm 2}^{(2)} &= \frac{\sqrt{6}}{4}\left(\frac{\partial^2}{\partial z^2} - \frac{\partial^2}{\partial y^2} \mp 2i\frac{\partial^2}{\partial y \partial z}\right)V^e\left(\mathbf{r}\right)
\end{aligned}
$$

Note that $V_k^{(2)}$ is related to the spherical harmonics by

$$V_k^{(2)} = r^2\mathcal{C}_k^{(2)}\left(\theta,\varphi\right)|_{x\to\frac{\partial}{\partial z},\,y\to-\frac{\partial}{\partial y},\,z\to\frac{\partial}{\partial x}}$$

where $\mathcal{C}_k^{(l)}\left(\theta,\varphi\right) = \sqrt{\frac{4\pi}{2l+1}}Y_k^{(l)}\left(\theta,\varphi\right)$. From above, we can see that if the electric field gradient has only a single component along the quantization axis, the eigenstates of the nuclear spin remain unchanged. However, when $V_{\pm 1,\pm 2}^{(2)} \neq 0$, the spin states are coupled and the nuclear spin is no longer quantized along the x-axis.

Without loss of generality, let us take

$$V_{i,1}^{(2)} = -V_{i,-1}^{(2)} = -\frac{\sqrt{6}}{2}V_{i,xy}^{(2)} \quad \text{and} \quad V_{i,0}^{(2)} = V_{i,\pm 2}^{(2)} = 0$$

Then

$$H^{\mathrm{Q}} = \sum_i A_i^{\mathrm{Q}}V_{i,xy}^{(2)}\left[2\left(\hat{I}_{i,+} + \hat{I}_{i,-}\right)\hat{I}_{i,x} + \hat{I}_{i,+} - \hat{I}_{i,-}\right], \quad A_i^{\mathrm{Q}} = \frac{3}{4}\frac{|Q_i|}{I_i\left(2I_i-1\right)}$$

For an applied magnetic field in x-direction, we have

$$
\begin{aligned}
H &= H_e^{\mathrm{Zee}} + H_n^{\mathrm{Zee}} + H_{e-n}^{\mathrm{FC}} + H^{\mathrm{Q}} \qquad \text{(D.5)} \\
&= \frac{g_e\mu_B}{\hbar}\widehat{S}_{e,x}B_x - \frac{\mu_N}{\hbar}\sum_i g_{n,i}\widehat{I}_{i,x}B_x + \sum_i A_{e,i}\left[\hat{S}_x\hat{I}_{i,x} + \frac{1}{2}\left(\hat{S}_+\hat{I}_{i,-} + \hat{S}_-\hat{I}_{i,+}\right)\right] + H^{\mathrm{Q}} \\
&= H_0 + H^{\mathrm{Q}}
\end{aligned}
$$

In the Schrieffer-Wolff transformation of Eq. (D.5) above:

$$\begin{aligned}\tilde{H} &= H_e^{\text{Zee}} + H_n^{\text{Zee}} + H_{e-n}^{\text{FC}} + H^{\text{Q}} \\ &\quad + \left[\mathscr{S}, H_e^{\text{Zee}}\right] + \left[\mathscr{S}, H_n^{\text{Zee}}\right] + \left[\mathscr{S}, H_{e-n}^{\text{FC}}\right] + \left[\mathscr{S}, H^{\text{Q}}\right] + \cdots\end{aligned}$$

if we let

$$\mathscr{S} = \frac{1}{B_x}\sum_i c_i^{'}\left[2\left(\hat{I}_{i,+}\hat{I}_{i,x} - \hat{I}_{i,x}\hat{I}_{i,-}\right) + \hat{I}_{i,+} - \hat{I}_{i,-}\right],\ c_i^{'} = \frac{\hbar A_i^{\text{Q}} V_{i,xy}^{(2)}}{\mu_N g_{n,i}}$$

then $\left[\mathscr{S}, H_e^{\text{Zee}}\right] = 0$ and $\left[\mathscr{S}, H_n^{\text{Zee}}\right] = -H^{\text{Q}}$. Neglecting terms higher than first order in $V_{i,xy}^{(2)}$, we obtain

$$\tilde{H} \approx H_0 + \left[\mathscr{S}, H_{e-n}^{\text{FC}}\right]$$

The commutator gives

$$\begin{aligned}\left[\mathscr{S}, H_{e-n}^{\text{FC}}\right] &= \sum_i \frac{\hbar A_{e,i} A_i^{\text{Q}} V_{i,xy}^{(2)}}{\mu_N g_{n,i} B_x}\Big[-2i\hat{S}_x\hat{I}_{i,y} - 4\hat{S}_x\hat{I}_{i,x}\hat{I}_{i,z} \\ &\quad + \left(\hat{S}_+ + \hat{S}_-\right)\left(2\hat{I}_{i,x}^2 + \hat{I}_{i,x} - \hat{I}_{i,+}\hat{I}_{i,-}\right) + \hat{S}_+\hat{I}_{i,-}^2 + \hat{S}_-\hat{I}_{i,+}^2\Big]\end{aligned}$$

in which the generic form of non-collinear hyperfine interaction, $\hat{S}_x\hat{I}_{i,y}$, can be found.

APPENDIX E

Modeling QDM-Field Interaction of the 8-Level System

In this appendix, the process for generating the fitting lineshapes for the data shown in Fig. 4.4, 4.5 and 4.6 in Chapter 4 is laid out using the example of the pump configuration shown in Fig. 4.4(a). For convenience, it is reproduced below.

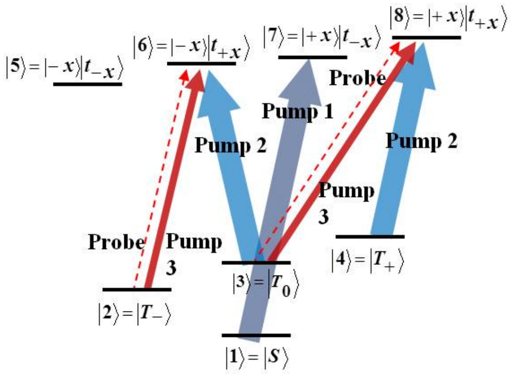

Figure E.1: Pump configuration for nuclear spin locking identical to that in Fig. 4.4(a). Reproduced here for convenience.

Using dipole and rotating-wave approximations, the Hamiltonian in Schrödinger picture for the QDM-field system shown in Fig. E.1 above is given by

$$H_S=\hbar\begin{bmatrix} \nu_1 & 0 & 0 & 0 & 0 & 0 & \frac{1}{\sqrt{2}}\tilde{\chi}_1(t) & 0 \\ 0 & \nu_2 & 0 & 0 & 0 & \tilde{\chi}_3(t)+\tilde{\chi}_p(t) & 0 & 0 \\ 0 & 0 & \nu_3 & 0 & 0 & \frac{1}{\sqrt{2}}\tilde{\chi}_2(t) & 0 & \frac{1}{\sqrt{2}}\tilde{\chi}_3(t)+\tilde{\chi}_p(t) \\ 0 & 0 & 0 & \nu_4 & 0 & 0 & 0 & \tilde{\chi}_2(t) \\ 0 & 0 & 0 & 0 & \nu_5 & 0 & 0 & 0 \\ 0 & \tilde{\chi}_3^*(t)+\tilde{\chi}_p^*(t) & \frac{1}{\sqrt{2}}\tilde{\chi}_2^*(t) & 0 & 0 & \nu_6 & 0 & 0 \\ \frac{1}{\sqrt{2}}\tilde{\chi}_1^*(t) & 0 & 0 & 0 & 0 & 0 & \nu_7 & 0 \\ 0 & 0 & \frac{1}{\sqrt{2}}\left(\tilde{\chi}_3^*(t)+\tilde{\chi}_p^*(t)\right) & \tilde{\chi}_2^*(t) & 0 & 0 & 0 & \nu_8 \end{bmatrix}$$

where the matrix elements are defined as

$$\begin{aligned}
\nu_1 &= -\frac{2}{\hbar}\left|J_{ex}\right| & \nu_5 &= \omega_0 - \frac{\mu_B}{2\hbar}\left(g_e - 3g_h\right)B_x \\
\nu_2 &= -\frac{\mu_B g_e B_x}{\hbar} & \nu_6 &= \omega_0 - \frac{\mu_B}{2\hbar}\left(g_e + 3g_h\right)B_x \\
\nu_3 &= 0 & \nu_7 &= \omega_0 + \frac{\mu_B}{2\hbar}\left(g_e + 3g_h\right)B_x \\
\nu_4 &= \frac{\mu_B g_e B_x}{\hbar} & \nu_8 &= \omega_0 + \frac{\mu_B}{2\hbar}\left(g_e - 3g_h\right)B_x
\end{aligned}$$

$$\begin{aligned}
\tilde{\chi}_1\left(t\right) &= \frac{\Omega_1}{2}e^{i\omega_1 t} & \tilde{\chi}_3\left(t\right) &= \frac{\Omega_3}{2}e^{i\omega_3 t} \\
\tilde{\chi}_2\left(t\right) &= \frac{\Omega_2}{2}e^{i\omega_2 t} & \tilde{\chi}_p\left(t\right) &= \frac{\Omega_p}{2}e^{i\omega_p t}
\end{aligned}$$

Here we assume that the energy separation between any two states is much larger than the natural linewidths of the optical transitions, so that each field drives only one transition except where a degeneracy occurs. ω_0 represents the resonance frequency for the triplet transitions at zero magnetic field. The Rabi frequencies for the optical fields are denoted by Ω_1, Ω_2, Ω_3 and Ω_p for Pump 1, Pump 2, Pump 3 and the probe, respectively, and their optical frequencies by ω_1, ω_2, ω_3 and ω_p. All other parameters are defined in § 3.3.

The presence of two fields, Pump 3 and the probe, driving the same transitions makes the calculation of steady-state solutions nontrivial. Following the approach outlined in Berman & Malinovsky[106], the first-order probe absorption is determined perturbatively from a steady-state solution in which all orders in the pump intensities are included. To reduce algebraic complexity, the Hamiltonian above is rotated into a different basis using a diagonal unitary matrix, $\hat{U}(t)$, with its elements given by $\{e^{-i\omega_1 t/2}$, $e^{i(\omega_2-\omega_3)t}$, 1, $e^{-i(\omega_2-\omega_3)t}$, 1, $e^{i\omega_2 t}$, $e^{i\omega_1 t/2}$, $e^{i\omega_3 t}\}$. The tranformed Hamiltonian,

H_f, is found using

$$H_f = i\hbar \left[\frac{d}{dt} \hat{U}\left(t\right) \right] \hat{U}^{\dagger}\left(t\right) + \hat{U}\left(t\right) H_S \hat{U}^{\dagger}\left(t\right) \tag{E.1}$$

$$= \hbar \begin{bmatrix} \nu_1 + \frac{\omega_1}{2} & 0 & 0 & 0 & 0 & 0 & \frac{\Omega_1^*}{2\sqrt{2}} & 0 \\ 0 & \nu_2 - \omega_2 + \omega_3 & 0 & 0 & 0 & \frac{\Omega_3 + \Omega_p e^{-i\Delta t}}{2} & 0 & 0 \\ 0 & 0 & \nu_3 & 0 & 0 & \frac{\Omega_2}{2\sqrt{2}} & 0 & \frac{\Omega_3 + \Omega_p e^{-i\Delta t}}{2\sqrt{2}} \\ 0 & 0 & 0 & \nu_4 + \omega_2 - \omega_3 & 0 & 0 & 0 & \frac{\Omega_2}{2} \\ 0 & 0 & 0 & 0 & \nu_5 & 0 & 0 & 0 \\ 0 & \frac{\Omega_3^* + \Omega_p^* e^{i\Delta t}}{2} & \frac{\Omega_2^*}{2\sqrt{2}} & 0 & 0 & \nu_6 - \omega_2 & 0 & 0 \\ \frac{\Omega_1^*}{2\sqrt{2}} & 0 & 0 & 0 & 0 & 0 & \nu_7 - \frac{\omega_1}{2} & 0 \\ 0 & 0 & \frac{\Omega_3^* + \Omega_p^* e^{i\Delta t}}{2\sqrt{2}} & \frac{\Omega_2^*}{2} & 0 & 0 & 0 & \nu_8 - \omega_3 \end{bmatrix}$$

where $\Delta = \omega_3 - \omega_4$. Let ρ be the 8×8 density matrix with its elements denoted by ρ_{ij}. The master equation for the time evolution of the system is given by

$$\frac{d}{dt}\rho = -\frac{i}{\hbar}\left[H_f, \rho\right] + \text{relaxation} \tag{E.2}$$

To determine the elements of the relaxation term, it is assumed that the ground state population relaxation is negligible so that the only experimental parameters in the relaxation term are the electron-hole recombination rate, Γ_r, and the electron spin decoherence rate, Γ_g, where $\Gamma_r \gg \Gamma_g$ is expected. Furthermore, the decoherence rates between any two spin ground states are assumed to have the same magnitude. With these simplifying assumptions, the relaxation term can be written explicitly as

$$\begin{bmatrix} \frac{\Gamma_r(\rho_{55}+\rho_{66}+\rho_{77}+\rho_{88})}{4} & -\Gamma_g\rho_{12} & -\Gamma_g\rho_{13} & -\Gamma_g\rho_{14} & -\frac{1}{2}\Gamma_r\rho_{15} & -\frac{1}{2}\Gamma_r\rho_{16} & -\frac{1}{2}\Gamma_r\rho_{17} & -\frac{1}{2}\Gamma_r\rho_{18} \\ -\Gamma_g\rho_{21} & \frac{\Gamma_r(\rho_{55}+\rho_{66})}{2} & -\Gamma_g\rho_{23} & -\Gamma_g\rho_{24} & -\frac{1}{2}\Gamma_r\rho_{25} & -\frac{1}{2}\Gamma_r\rho_{26} & -\frac{1}{2}\Gamma_r\rho_{27} & -\frac{1}{2}\Gamma_r\rho_{28} \\ -\Gamma_g\rho_{31} & -\Gamma_g\rho_{32} & \frac{\Gamma_r(\rho_{55}+\rho_{66}+\rho_{77}+\rho_{88})}{4} & -\Gamma_g\rho_{34} & -\frac{1}{2}\Gamma_r\rho_{35} & -\frac{1}{2}\Gamma_r\rho_{36} & -\frac{1}{2}\Gamma_r\rho_{37} & -\frac{1}{2}\Gamma_r\rho_{38} \\ -\Gamma_g\rho_{41} & -\Gamma_g\rho_{42} & -\Gamma_g\rho_{43} & \frac{\Gamma_r(\rho_{77}+\rho_{88})}{2} & -\frac{1}{2}\Gamma_r\rho_{45} & -\frac{1}{2}\Gamma_r\rho_{46} & -\frac{1}{2}\Gamma_r\rho_{47} & -\frac{1}{2}\Gamma_r\rho_{48} \\ -\frac{1}{2}\Gamma_r\rho_{51} & -\frac{1}{2}\Gamma_r\rho_{52} & -\frac{1}{2}\Gamma_r\rho_{53} & -\frac{1}{2}\Gamma_r\rho_{54} & -\Gamma_r\rho_{55} & -\Gamma_r\rho_{56} & -\Gamma_r\rho_{57} & -\Gamma_r\rho_{58} \\ -\frac{1}{2}\Gamma_r\rho_{61} & -\frac{1}{2}\Gamma_r\rho_{62} & -\frac{1}{2}\Gamma_r\rho_{63} & -\frac{1}{2}\Gamma_r\rho_{64} & -\Gamma_r\rho_{65} & -\Gamma_r\rho_{66} & -\Gamma_r\rho_{67} & -\Gamma_r\rho_{68} \\ -\frac{1}{2}\Gamma_r\rho_{71} & -\frac{1}{2}\Gamma_r\rho_{72} & -\frac{1}{2}\Gamma_r\rho_{73} & -\frac{1}{2}\Gamma_r\rho_{74} & -\Gamma_r\rho_{75} & -\Gamma_r\rho_{76} & -\Gamma_r\rho_{77} & -\Gamma_r\rho_{78} \\ -\frac{1}{2}\Gamma_r\rho_{81} & -\frac{1}{2}\Gamma_r\rho_{82} & -\frac{1}{2}\Gamma_r\rho_{83} & -\frac{1}{2}\Gamma_r\rho_{84} & -\Gamma_r\rho_{85} & -\Gamma_r\rho_{86} & -\Gamma_r\rho_{87} & -\Gamma_r\rho_{88} \end{bmatrix}$$

By treating the probe laser as the perturbation, an approximate solution would have the form

$$\rho_{ij} = \rho_{ij}^{(0)} + \rho_{ij}^{(1)} \tag{E.3}$$

where $\rho_{ij}^{(0)}$ is the steady-state solution of the master equation with the probe Rabi frequency, Ω_p, set to zero. Let us take

$$\rho_{ij}^{(1)} = a_{ij} + b_{ij}e^{i\Delta t} + c_{ij}e^{-i\Delta t} \tag{E.4}$$

as an ansatz. Once the solution for $\rho_{ij}^{(0)}$ is found, Eq. (E.3) and (E.4) are substituted into the master equation, i. e., Eq. (E.2). By equating the constants and the coefficients of $e^{\pm i\Delta t}$ on both sides of Eq. (E.2), a system of linear equations in terms of a_{ij}, b_{ij}, and c_{ij} is obtained. This is then solved numerically to determine the values of a_{ij}, b_{ij}, and c_{ij} for each probe frequency, ω_p. The absorption of the probe is given by the sum of the imaginary parts of c_{26} and c_{38}. To see this, one simply goes back to the Schrödinger picture to find that c_{26} and c_{38} are the coefficients of the probe field, $e^{i\omega_p t}$.

To fit the measured lineshapes, the fitting parameters that need to be considered are the Rabi frequencies and detunings of Pump 2 and Pump 3, Γ_r and Γ_g. The calculation outlined above is repeated while one of the six parameters is varied. The best-fit value corresponding to the least error-squares is then carried over to the next set of calculations where another parameter is sweeped. This is whole process is repeated until all six parameter values converge. For the two most important parameters, Γ_r and Γ_g, it is worth taking a look at how the error-squares change with the parameter values. Fig. E.2 below shows the error-squares of the resulting fit when Γ_r and Γ_g are varied. In Fig. E.2(a) which corresponds to the fit for the lineshape at ω_{26} as shown in Fig. 4.4(b) in Chapter 4, an enclosed region of least error-squares is found. Here, the best fitting values for Γ_r and Γ_g can be uniquely determined. However, in Fig. E.2(b) for the resonance profile at ω_{48} shown in Fig. 4.4(d), there is no such enclave for the parameter Γ_g. Nonetheless, an upper bound for the spin decoherence time is found to be 1.3 μs. Tables E.1 and E.2 summarize the physical parameters of the QDM used in this study and the best-fit values for the spectra shown in Fig. 4.4, respectively.

For the spectra shown in Fig. 4.5(b) and 4.6(b), the Rabi frequencies of the pump lasers can be estimated based on the incident powers and the best-fit parameters found above. Also, the detunings can be easily determined from the positions of the dark-state dips. Assuming that Γ_r remains the same, the only fitting parameters need to be considered here are Γ_g and the Overhauser field distribution. The distribution is constructed from three Gaussian curves with different widths, heights and offsets. The same procedure discussed above is used to find the best-fit value for Γ_g and the Overhauser field distribution. Only this time the lineshape is a weighted average of many spectra calculated from distinct magnetic fields.

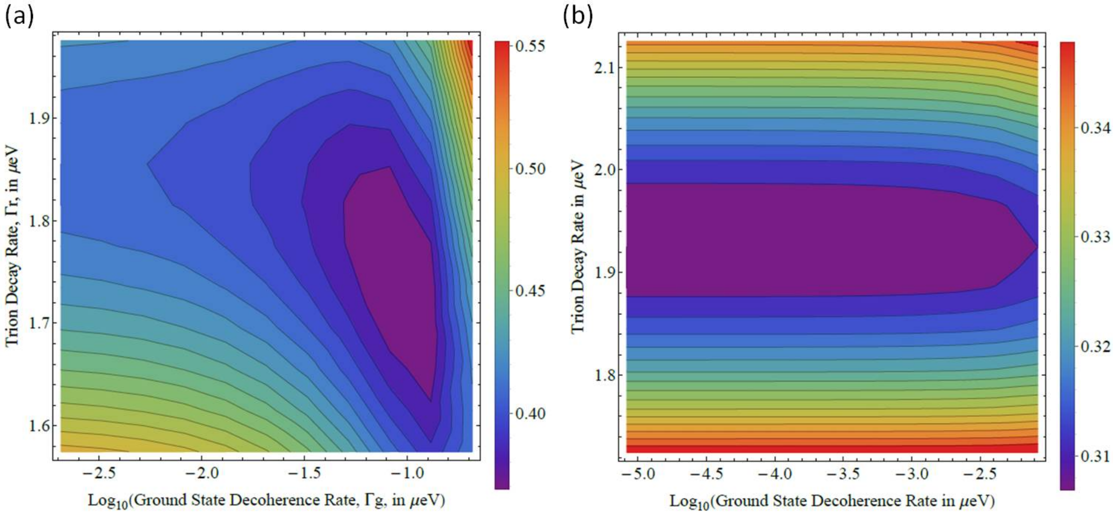

Figure E.2: (a) Contour plot showing error-squares from the $|T_{-}\rangle$ transition lineshape fits calculated by varying the values of Γ_r and Γ_g. The model for the corresponding pump configuration is discussed in this appendix. (b) Contour plot of the error-squares for the $|T_{+}\rangle$ case, showing the absence of a converging best-fit value for the parameter Γ_g.

Constants	$2\,|J_{ex}|$	ω_0	g_e	g_h
Values	116.6	1294.543	0.43	-0.084
Units	μeV	meV	-	-

Table E.1: Physical parameters of the QDM used in this study.

Parameters	Ω_1	δ_1	Ω_2	δ_2	Ω_3	δ_3	Ω_p	Γ_r	Γ_g
Fig. 4.4(b) :ω_{26}	1.96	0	1.82	-0.61	0.35	-1.55	0.19	1.78	0.050
Fig. 4.4(d): ω_{48}	1.86	0	1.86	-1.06	0.36	-1.41	0.19	1.93	0.0032

Table E.2: Parameters used to produce the fitting curves in Fig. 4.4(b) and (d). All values are in units of μeV. Here, δ_i denotes detuning from corresponding transition.

APPENDIX F

Estimate of the Intrinsic Overhauser Field Distribution

An order-of-magnitude estimate of the intrinsic Overhauser field distribution can be derived as follows: The field contributed by type-α nuclear isotope in a primitive unit cell at position $\mathbf{r}$ is given by

$$\delta B_{\alpha,\mathbf{r}} = \frac{a_0^3}{4 g_e \mu_B} \left| \Psi_e \left(\mathbf{r} \right) \right|^2 A_{e,\mathbf{r}} \hat{I}^x_{\alpha,\mathbf{r}}$$

where a_0 is the lattice constant, $\Psi_e \left(\mathbf{r} \right)$ the electron envelop wavefunction, $A_{e,\mathbf{r}}$ the electron nuclear hyperfine constant, and $\hat{I}^x_{\alpha,\mathbf{r}}$ the nuclear spin projection along the quantization axis. Since the spin projection of a nucleus can only assume discrete values, $\delta B_{\alpha,\mathbf{r}}$ can be treated as a random variable. The Overhauser field, B_{OH}, given by the sum of $\delta B_{\alpha,\mathbf{r}}$, then follows the multinomial distribution, which approaches the Gaussian distribution for a large number of nuclei. At the operating temperature of 6 K, $k_B T = 517$ μeV, which is much larger than the nuclear Zeeman splitting[107]. Hence $\bar{I}^x_\alpha \approx 0$ and the distribution of B_{OH} is given by

$$f \left(B_{OH} \right) = \frac{1}{\sqrt{2\pi}\sigma} e^{-\frac{B_{OH}^2}{2\sigma^2}}$$

where

$$\begin{aligned}\sigma &= \sqrt{\sum_{\mathbf{r},\alpha} \delta B_{\alpha,\mathbf{r}}^2} \\ &= \frac{a_0^3}{4 g_e \mu_B} \sqrt{\sum_{\mathbf{r},\alpha} \left|\Psi_e\left(\mathbf{r}\right)\right|^4 A_{e,\mathbf{r}}^2 \left(\bar{I}_\alpha^x\right)^2} \\ &\approx \frac{1}{g_e \mu_B} \sqrt{\frac{1}{3N} \sum_{\mathbf{r},\alpha} A_{e,\mathbf{r}}^2 I_\alpha \left(I_\alpha + 1\right)}\end{aligned}$$

Here, N is the number of unit cells in a single QD. In arriving at the last expression, the wavefunction is assumed to be uniform, i. e., $\left|\Psi_e\left(\mathbf{r}\right)\right|^2 = 4/Na_0^3$. Note that each primitive unit cell contains an In nucleus and an As nucleus. If we further assume that the wavefunction of the electron effectively occupies a cylindrical volume with a diameter of 10 nm and a height of 3 nm, then $N \approx 4250$ for $a_0 = 6.05$ Å. Using $A_{\mathrm{In}} = 56$ μeV and $A_{\mathrm{As}} = 47$ μeV for spin-$\frac{9}{2}$ In and spin-$\frac{3}{2}$ As nuclei[108], respectively, a standard deviation, given by σ, of 0.11 Tesla is obtained for the intrinsic Overhauser field distribution. This order-of-magnitude estimate is in agreement with the experimentally determined value of 0.15 Tesla given in Chapter 4.

BIBLIOGRAPHY

BIBLIOGRAPHY

[1] I. A. Merkulov, Al. L. Efros, and M. Rosen. Electron spin relaxation by nuclei in semiconductor quantum dots. *Phys. Rev. B*, 65:205309, Apr 2002.

[2] P.-F. Braun, X. Marie, L. Lombez, B. Urbaszek, T. Amand, P. Renucci, V. K. Kalevich, K. V. Kavokin, O. Krebs, P. Voisin, and Y. Masumoto. Direct observation of the electron spin relaxation induced by nuclei in quantum dots. *Phys. Rev. Lett.*, 94:116601, Mar 2005.

[3] Xiaodong Xu, Wang Yao, Bo Sun, Duncan G. Steel, Allan S. Bracker, Daniel Gammon, and L. J. Sham. Optically controlled locking of the nuclear field via coherent dark-state spectroscopy. *Nature*, 459:1105–1109, 2009.

[4] I. Vurgaftman, J. R. Meyer, and L. R. Ram-Mohan. Band parameters for iii-v compound semiconductors and their alloys. *Journal of Applied Physics*, 89(11):5815–5875, 2001.

[5] A. Baldereschi and Nunzio O. Lipari. Spherical model of shallow acceptor states in semiconductors. *Phys. Rev. B*, 8:2697–2709, Sep 1973.

[6] David P. DiVincenzo. The physical implementation of quantum computation. *Fortschritte der Physik*, 48(9-11):771–783, 2000.

[7] Danny Kim, Samuel G. Carter, Alex Greilich, Allan S. Bracker, and Daniel Gammon. Ultrafast optical control of entanglement between two quantum-dot spins. *Nat Phys*, 7(3):223–229, March 2011.

[8] K. M. Weiss, J. M. Elzerman, Y. L. Delley, J. Miguel-Sanchez, and A. Imamoğlu. Coherent two-electron spin qubits in an optically active pair of coupled ingaas quantum dots. *Phys. Rev. Lett.*, 109:107401, Sep 2012.

[9] M. F. Doty, M. Scheibner, A. S. Bracker, I. V. Ponomarev, T. L. Reinecke, and D. Gammon. Optical spectra of doubly charged quantum dot molecules in electric and magnetic fields. *Phys. Rev. B*, 78:115316, Sep 2008.

[10] Michael Scheibner, Allan S. Bracker, Danny Kim, and Daniel Gammon. Essential concepts in the optical properties of quantum dot molecules. *Solid State Communications*, 149:1427–1435, 2009.

[11] Xiaodong Xu, Wang Yao, Bo Sun, Duncan G Steel, Allan S Bracker, Daniel Gammon, and LJ Sham. Optically controlled locking of the nuclear field via coherent dark-state spectroscopy. *Nature*, 459(7250):1105–1109, 2009.

[12] Miro Kroutvar, Yann Ducommun, Dominik Heiss, Max Bichler, Dieter Schuh, Gerhard Abstreiter, and Jonathan J. Finley. Optically programmable electron spin memory using semiconductor quantum dots. *Nature*, 432(7013):81–84, November 2004.

[13] Mete Atatüre, Jan Dreiser, Antonio Badolato, Alexander Högele, Khaled Karrai, and Atac Imamoglu. Quantum-dot spin-state preparation with near-unity fidelity. *Science*, 312(5773):551–553, 2006.

[14] C. Emary, Xiaodong Xu, D. G. Steel, S. Saikin, and L. J. Sham. Fast initialization of the spin state of an electron in a quantum dot in the voigt configuration. *Phys. Rev. Lett.*, 98:047401, Jan 2007.

[15] Xiaodong Xu, Yanwen Wu, Bo Sun, Qiong Huang, Jun Cheng, D. G. Steel, A. S. Bracker, D. Gammon, C. Emary, and L. J. Sham. Fast spin state initialization in a singly charged inas-gaas quantum dot by optical cooling. *Phys. Rev. Lett.*, 99:097401, Aug 2007.

[16] J. Berezovsky, M. H. Mikkelsen, O. Gywat, N. G. Stoltz, L. A. Coldren, and D. D. Awschalom. Nondestructive optical measurements of a single electron spin in a quantum dot. *Science*, 314(5807):1916–1920, 2006.

[17] Xiaodong Xu, Bo Sun, Paul R. Berman, Duncan G. Steel, Allan S. Bracker, Dan Gammon, and L. J. Sham. Coherent optical spectroscopy of a strongly driven quantum dot. *Science*, 317(5840):929–932, 2007.

[18] J. Berezovsky, M. H. Mikkelsen, N. G. Stoltz, L. A. Coldren, and D. D. Awschalom. Picosecond coherent optical manipulation of a single electron spin in a quantum dot. *Science*, 320(5874):349–352, 2008.

[19] David Press, Thaddeus D. Ladd, Bingyang Zhang, and Yoshihisa Yamamoto. Complete quantum control of a single quantum dot spin using ultrafast optical pulses. *Nature*, 456(7219):218–221, November 2008.

[20] A. Greilich, Sophia E. Economou, S. Spatzek, D. R. Yakovlev, D. Reuter, A. D. Wieck, T. L. Reinecke, and M. Bayer. Ultrafast optical rotations of electron spins in quantum dots. *Nat Phys*, 5(4):262–266, April 2009.

[21] Erik D. Kim, Katherine Truex, Xiaodong Xu, Bo Sun, D. G. Steel, A. S. Bracker, D. Gammon, and L. J. Sham. Fast spin rotations by optically controlled geometric phases in a charge-tunable inas quantum dot. *Phys. Rev. Lett.*, 104:167401, Apr 2010.

[22] Bo Sun, Colin Ming Earn Chow, Duncan G. Steel, Allan S. Bracker, Daniel Gammon, and L. J. Sham. Persistent narrowing of nuclear-spin fluctuations in inas quantum dots using laser excitation. *Phys. Rev. Lett.*, 108:187401, May 2012.

[23] Kristiaan De Greve, Leo Yu, Peter L. McMahon, Jason S. Pelc, Chandra M. Natarajan, Na Young Kim, Eisuke Abe, Sebastian Maier, Christian Schneider, Martin Kamp, Sven Hofling, Robert H. Hadfield, Alfred Forchel, M. M. Fejer, and Yoshihisa Yamamoto. Quantum-dot spin-photon entanglement via frequency downconversion to telecom wavelength. *Nature*, 491(7424):421–425, November 2012.

[24] W. B. Gao, P. Fallahi, E. Togan, J. Miguel-Sanchez, and A. Imamoglu. Observation of entanglement between a quantum dot spin and a single photon. *Nature*, 491(7424):426–430, November 2012.

[25] J. R. Schaibley, A. P. Burgers, G. A. McCracken, L.-M. Duan, P. R. Berman, D. G. Steel, A. S. Bracker, D. Gammon, and L. J. Sham. Demonstration of quantum entanglement between a single electron spin confined to an inas quantum dot and a photon. *Phys. Rev. Lett.*, 110:167401, Apr 2013.

[26] T. D. Ladd and Y. Yamamoto. Simple quantum logic gate with quantum dot cavity qed systems. *Phys. Rev. B*, 84:235307, Dec 2011.

[27] Sophia E. Economou, Juan I. Climente, Antonio Badolato, Allan S. Bracker, Daniel Gammon, and Matthew F. Doty. Scalable qubit architecture based on holes in quantum dot molecules. *Phys. Rev. B*, 86:085319, Aug 2012.

[28] Shruti Puri, Na Young Kim, and Yoshihisa Yamamoto. Two-qubit geometric phase gate for quantum dot spins using cavity polariton resonance. *Phys. Rev. B*, 85:241403, Jun 2012.

[29] Dmitry Solenov, Sophia E. Economou, and T. L. Reinecke. Fast two-qubit gates for quantum computing in semiconductor quantum dots using a photonic microcavity. *Phys. Rev. B*, 87:035308, Jan 2013.

[30] Samuel G. Carter, Timothy M. Sweeney, Mijin Kim, Chul Soo Kim, Dmitry Solenov, Sophia E. Economou, Thomas L. Reinecke, Lily Yang, Allan S. Bracker, and Daniel Gammon. Quantum control of a spin qubit coupled to a photonic crystal cavity. *Nat Photon*, 7(4):329–334, April 2013.

[31] C. Piermarocchi, Pochung Chen, L. J. Sham, and D. G. Steel. Optical rkky interaction between charged semiconductor quantum dots. *Phys. Rev. Lett.*, 89:167402, Sep 2002.

[32] C. Emary and L. J. Sham. Optically controlled logic gates for two spin qubits in vertically coupled quantum dots. *Phys. Rev. B*, 75:125317, Mar 2007.

[33] Li-Bo Chen, L. J. Sham, and Edo Waks. Optically controlled phase gate for two spin qubits in coupled quantum dots. *Phys. Rev. B*, 85:115319, Mar 2012.

[34] N. Cody Jones, Rodney Van Meter, Austin G. Fowler, Peter L. McMahon, Jungsang Kim, Thaddeus D. Ladd, and Yoshihisa Yamamoto. Layered architecture for quantum computing. *Phys. Rev. X*, 2:031007, Jul 2012.

[35] M. Bayer, P. Hawrylak, K. Hinzer, S. Fafard, M. Korkusinski, Z. R. Wasilewski, O. Stern, and A. Forchel. Coupling and entangling of quantum states in quantum dot molecules. *Science*, 291(5503):451–453, 2001.

[36] E. A. Stinaff, M. Scheibner, A. S. Bracker, I. V. Ponomarev, V. L. Korenev, M. E. Ware, M. F. Doty, T. L. Reinecke, and D. Gammon. Optical signatures of coupled quantum dots. *Science*, 311(5761):636–639, 2006.

[37] A. S. Bracker, M. Scheibner, M. F. Doty, E. A. Stinaff, I. V. Ponomarev, J. C. Kim, L. J. Whitman, T. L. Reinecke, and D. Gammon. Engineering electron and hole tunneling with asymmetric inas quantum dot molecules. *Applied Physics Letters*, 89(23):233110 –233110–3, dec 2006.

[38] M. F. Doty, M. Scheibner, I. V. Ponomarev, E. A. Stinaff, A. S. Bracker, V. L. Korenev, T. L. Reinecke, and D. Gammon. Electrically tunable g factors in quantum dot molecular spin states. *Phys. Rev. Lett.*, 97:197202, Nov 2006.

[39] M. Scheibner, I. V. Ponomarev, E. A. Stinaff, M. F. Doty, A. S. Bracker, C. S. Hellberg, T. L. Reinecke, and D. Gammon. Photoluminescence spectroscopy of the molecular biexciton in vertically stacked inas-gaas quantum dot pairs. *Phys. Rev. Lett.*, 99:197402, Nov 2007.

[40] M. Scheibner, M. F. Doty, I. V. Ponomarev, A. S. Bracker, E. A. Stinaff, V. L. Korenev, T. L. Reinecke, and D. Gammon. Spin fine structure of optically excited quantum dot molecules. *Phys. Rev. B*, 75:245318, Jun 2007.

[41] M. Scheibner, M. Yakes, A. S. Bracker, I. V. Ponomarev, M. F. Doty, C. S. Hellberg, L. J. Whitman, T. L. Reinecke, and D. Gammon. Optically mapping the electronic structure of coupled quantum dots. *Nat Phys*, 4(4):291–295, April 2008.

[42] M. F. Doty, J. I. Climente, M. Korkusinski, M. Scheibner, A. S. Bracker, P. Hawrylak, and D. Gammon. Antibonding ground states in inas quantum-dot molecules. *Phys. Rev. Lett.*, 102:047401, Jan 2009.

[43] L. Goldstein, F. Glas, J. Y. Marzin, M. N. Charasse, and G. Le Roux. Growth by molecular beam epitaxy and characterization of inas/gaas strained-layer superlattices. *Applied Physics Letters*, 47(10):1099–1101, 1985.

[44] Gert Schedelbeck, Werner Wegscheider, Max Bichler, and Gerhard Abstreiter. Coupled quantum dots fabricated by cleaved edge overgrowth: From artificial atoms to molecules. *Science*, 278(5344):1792–1795, 1997.

[45] W. Dybalski and P. Hawrylak. Two electrons in a strongly coupled double quantum dot: From an artificial helium atom to a hydrogen molecule. *Phys. Rev. B*, 72:205432, Nov 2005.

[46] Guido Burkard, Georg Seelig, and Daniel Loss. Spin interactions and switching in vertically tunnel-coupled quantum dots. *Phys. Rev. B*, 62:2581–2592, Jul 2000.

[47] O. Gywat, H.J. Krenner, and J. Berezovsky. *Spins in Optically Active Quantum Dots*. Wiley, 2009.

[48] G. Ortner, M. Bayer, Y. Lyanda-Geller, T. L. Reinecke, A. Kress, J. P. Reithmaier, and A. Forchel. Control of vertically coupled InGaAs/GaAs quantum dots with electric fields. *Phys. Rev. Lett.*, 94:157401, Apr 2005.

[49] M. F. Doty, J. I. Climente, A. Greilich, M. Yakes, A. S. Bracker, and D. Gammon. Hole-spin mixing in inas quantum dot molecules. *Phys. Rev. B*, 81:035308, Jan 2010.

[50] Z.R. Wasilewski, S. Fafard, and J.P. McCaffrey. Size and shape engineering of vertically stacked self-assembled quantum dots. *Journal of Crystal Growth*, 201/202(0):1131 – 1135, 1999.

[51] P. Bhattacharya. *Semiconductor Optoelectronic Devices*. Prentice Hall, 1997.

[52] Donald Neamen. *Semiconductor Physics And Devices*. McGraw-Hill, Inc., New York, NY, USA, 3 edition, 2003.

[53] J. Singh. *Electronic and Optoelectronic Properties of Semiconductor Structures*. Cambridge University Press, 2007.

[54] W. B. Joyce and R. W. Dixon. Analytic approximations for the fermi energy of an ideal fermi gas. *Applied Physics Letters*, 31(5):354–356, 1977.

[55] G. Vincent, A. Chantre, and D. Bois. Electric field effect on the thermal emission of traps in semiconductor junctions. *Journal of Applied Physics*, 50(8):5484–5487, 1979.

[56] J. D. Mar, X. L. Xu, J. J. Baumberg, F. S. F. Brossard, A. C. Irvine, C. Stanley, and D. A. Williams. Bias-controlled single-electron charging of a self-assembled quantum dot in a two-dimensional-electron-gas-based $n-i$-schottky diode. *Phys. Rev. B*, 83:075306, Feb 2011.

[57] E. N. Korol. Ionization of impurity states in semiconductors by an electric field. *Soviet Physics - Solid State*, 19(8):1327–1330, 1977.

[58] C. M. A. Kapteyn, F. Heinrichsdorff, O. Stier, R. Heitz, M. Grundmann, N. D. Zakharov, D. Bimberg, and P. Werner. Electron escape from inas quantum dots. *Phys. Rev. B*, 60:14265–14268, Nov 1999.

[59] J. Ibanez, R. Leon, D. T. Vu, S. Chaparro, S. R. Johnson, C. Navarro, and Y. H. Zhang. Tunneling carrier escape from inas self-assembled quantum dots. *Applied Physics Letters*, 79(13):2013–2015, 2001.

[60] Hongtao Jiang and Jasprit Singh. Strain distribution and electronic spectra of inas/gaas self-assembled dots: An eight-band study. *Phys. Rev. B*, 56:4696–4701, Aug 1997.

[61] G.F. Koster. *Properties of the thirty-two point groups.* Massachusetts institute of technology press research monograph. M.I.T. Press, 1963.

[62] E. L. Ivchenko and Grigorii Ezekielevich Pikus. *Superlattices and Other Heterostructures: Symmetry and Optical Phenomena.* Springer, Berlin, 1997.

[63] Leon A Webster. *Precursor to spin-photon entanglement in a single InAs/GaAs quantum dot.* PhD thesis, University of Michigan, 2012.

[64] M. Bayer, G. Ortner, O. Stern, A. Kuther, A. A. Gorbunov, A. Forchel, P. Hawrylak, S. Fafard, K. Hinzer, T. L. Reinecke, S. N. Walck, J. P. Reithmaier, F. Klopf, and F. Schäfer. Fine structure of neutral and charged excitons in self-assembled in(ga)as/(al)gaas quantum dots. *Phys. Rev. B*, 65:195315, May 2002.

[65] Danny Kim, Sophia E. Economou, Ştefan C. Bădescu, Michael Scheibner, Allan S. Bracker, Mark Bashkansky, Thomas L. Reinecke, and Daniel Gammon. Optical spin initialization and nondestructive measurement in a quantum dot molecule. *Phys. Rev. Lett.*, 101:236804, Dec 2008.

[66] A. Shabaev, Al. L. Efros, D. Gammon, and I. A. Merkulov. Optical readout and initialization of an electron spin in a single quantum dot. *Phys. Rev. B*, 68:201305, Nov 2003.

[67] J. M. Elzerman, K. M. Weiss, J. Miguel-Sanchez, and A. Imamoğlu. Optical amplification using raman transitions between spin-singlet and spin-triplet states of a pair of coupled in-gaas quantum dots. *Phys. Rev. Lett.*, 107:017401, Jun 2011.

[68] A. Boyer de la Giroday, N. Sköld, R. M. Stevenson, I. Farrer, D. A. Ritchie, and A. J. Shields. Exciton-spin memory with a semiconductor quantum dot molecule. *Phys. Rev. Lett.*, 106:216802, May 2011.

[69] N. Sköld, A. Boyer de la Giroday, A. J. Bennett, I. Farrer, D. A. Ritchie, and A. J. Shields. Electrical control of the exciton fine structure of a quantum dot molecule. *Phys. Rev. Lett.*, 110:016804, Jan 2013.

[70] J. Kempe, D. Bacon, D. A. Lidar, and K. B. Whaley. Theory of decoherence-free fault-tolerant universal quantum computation. *Phys. Rev. A*, 63:042307, Mar 2001.

[71] J. R. Petta, A. C. Johnson, J. M. Taylor, E. A. Laird, A. Yacoby, M. D. Lukin, C. M. Marcus, M. P. Hanson, and A. C. Gossard. Coherent manipulation of coupled electron spins in semiconductor quantum dots. *Science*, 309(5744):2180–2184, 2005.

[72] P. Maletinsky, C. W. Lai, A. Badolato, and A. Imamoglu. Nonlinear dynamics of quantum dot nuclear spins. *Phys. Rev. B*, 75:035409, Jan 2007.

[73] Wen Yang and L. J. Sham. Collective nuclear stabilization in single quantum dots by noncollinear hyperfine interaction. *Phys. Rev. B*, 85:235319, Jun 2012.

[74] Bernhard Urbaszek, Xavier Marie, Thierry Amand, Olivier Krebs, Paul Voisin, Patrick Maletinsky, Alexander Högele, and Atac Imamoglu. Nuclear spin physics in quantum dots: An optical investigation. *Rev. Mod. Phys.*, 85:79–133, Jan 2013.

[75] Wen Yang and L. J. Sham. General theory of feedback control of a nuclear spin ensemble in quantum dots. *Phys. Rev. B*, 88:235304, Dec 2013.

[76] A. Högele, M. Kroner, C. Latta, M. Claassen, I. Carusotto, C. Bulutay, and A. Imamoglu. Dynamic nuclear spin polarization in the resonant laser excitation of an ingaas quantum dot. *Phys. Rev. Lett.*, 108:197403, May 2012.

[77] R. A. McFarlane. Frequency pushing and frequency pulling in a he-ne gas optical maser. *Phys. Rev.*, 135:A543–A550, Aug 1964.

[78] Willis E. Lamb. Theory of an optical maser. *Phys. Rev.*, 134:A1429–A1450, Jun 1964.

[79] Chia-Wei Huang and Xuedong Hu. Theoretical study of nuclear spin polarization and depolarization in self-assembled quantum dots. *Phys. Rev. B*, 81:205304, May 2010.

[80] Changxue Deng and Xuedong Hu. Nuclear spin diffusion in quantum dots: Effects of inhomogeneous hyperfine interaction. *Phys. Rev. B*, 72:165333, Oct 2005.

[81] Christian Latta, Ajit Srivastava, and Atac Imamoğlu. Hyperfine interaction-dominated dynamics of nuclear spins in self-assembled ingaas quantum dots. *Phys. Rev. Lett.*, 107:167401, Oct 2011.

[82] E. A. Chekhovich, K. V. Kavokin, J. Puebla, A. B. Krysa, M. Hopkinson, A. D. Andreev, A. M. Sanchez, R. Beanland, M. S. Skolnick, and A. I. Tartakovskii. Structural analysis of strained quantum dots using nuclear magnetic resonance. *Nat. Nano*, 7:646–650, 2012.

[83] Jan Fischer, W. A. Coish, D. V. Bulaev, and Daniel Loss. Spin decoherence of a heavy hole coupled to nuclear spins in a quantum dot. *Phys. Rev. B*, 78:155329, Oct 2008.

[84] B. Eble, C. Testelin, P. Desfonds, F. Bernardot, A. Balocchi, T. Amand, A. Miard, A. Lemaître, X. Marie, and M. Chamarro. Hole˘nuclear spin interaction in quantum dots. *Phys. Rev. Lett.*, 102:146601, Apr 2009.

[85] P. Fallahi, S. T. Y ılmaz, and A. Imamoğlu. Measurement of a heavy-hole hyperfine interaction in ingaas quantum dots using resonance fluorescence. *Phys. Rev. Lett.*, 105:257402, Dec 2010.

[86] Jan Fischer and Daniel Loss. Hybridization and spin decoherence in heavy-hole quantum dots. *Phys. Rev. Lett.*, 105:266603, Dec 2010.

[87] Alex Greilich, Samuel G. Carter, Danny Kim, Allan S. Bracker, and Daniel Gammon. Optical control of one and two hole spins in interacting quantum dots. *Nat Photon*, 5(11):702–708, November 2011.

[88] M. Issler, E. M. Kessler, G. Giedke, S. Yelin, I. Cirac, M. D. Lukin, and A. Imamoglu. Nuclear spin cooling using overhauser-field selective coherent population trapping. *Phys. Rev. Lett.*, 105:267202, Dec 2010.

[89] Hendrik Bluhm, Sandra Foletti, Diana Mahalu, Vladimir Umansky, and Amir Yacoby. Enhancing the coherence of a spin qubit by operating it as a feedback loop that controls its nuclear spin bath. *Phys. Rev. Lett.*, 105:216803, Nov 2010.

[90] M. J. A. Schuetz, E. M. Kessler, L. M. K. Vandersypen, J. I. Cirac, and G. Giedke. Nuclear spin dynamics in double quantum dots: Multistability, dynamical polarization, criticality, and entanglement. *Phys. Rev. B*, 89:195310, May 2014.

[91] Daniel Loss and David P. DiVincenzo. Quantum computation with quantum dots. *Phys. Rev. A*, 57:120–126, Jan 1998.

[92] R. Brunner, Y.-S. Shin, T. Obata, M. Pioro-Ladrière, T. Kubo, K. Yoshida, T. Taniyama, Y. Tokura, and S. Tarucha. Two-qubit gate of combined single-spin rotation and interdot spin exchange in a double quantum dot. *Phys. Rev. Lett.*, 107:146801, Sep 2011.

[93] L. M. K. Vandersypen and I. L. Chuang. Nmr techniques for quantum control and computation. *Rev. Mod. Phys.*, 76:1037–1069, Jan 2005.

[94] Zhexuan Gong. *Quantum Computation and Quantum Similation with Atomic and Solid State Systems*. PhD thesis, University of Michigan, 2013.

[95] Jun Zhang, Jiri Vala, Shankar Sastry, and K. Birgitta Whaley. Geometric theory of nonlocal two-qubit operations. *Phys. Rev. A*, 67:042313, Apr 2003.

[96] W. Dur, G. Vidal, and J. I. Cirac. Optimal conversion of nonlocal unitary operations. *Phys. Rev. Lett.*, 89:057901, Jul 2002.

[97] Paul Watts, Maurice O'Connor, and Jiri Vala. Metric structure of the space of two-qubit gates, perfect entanglers and quantum control. *Entropy*, 15(6):1963–1984, 2013.

[98] Navin Khaneja and Steffen J. Glaser. Cartan decomposition of su(2n) and control of spin systems. *Chemical Physics*, 267:11–23, 2001.

[99] Jun Zhang, Jiri Vala, Shankar Sastry, and K. Birgitta Whaley. Exact two-qubit universal quantum circuit. *Phys. Rev. Lett.*, 91:027903, Jul 2003.

[100] N. E. Bonesteel, D. Stepanenko, and D. P. DiVincenzo. Anisotropic spin exchange in pulsed quantum gates. *Phys. Rev. Lett.*, 87:207901, Oct 2001.

[101] W. W. Cheng and J.-M. Liu. Decoherence from spin environment: Role of the dzyaloshinsky-moriya interaction. *Phys. Rev. A*, 79:052320, May 2009.

[102] J. M. Taylor, C. M. Marcus, and M. D. Lukin. Long-lived memory for mesoscopic quantum bits. *Phys. Rev. Lett.*, 90:206803, May 2003.

[103] Patrick Vora, Samuel Carter, Mijin Kim, Timothy Sweeney, Lily Yang, Peter Brereton, Allan S. Bracker, and Daniel Gammon. Cavity qed in a quantum dot molecule coupled to a photonic crystal cavity. In *http://meetings.aps.org/link/BAPS.2014.MAR.A36.1*, 2015.

[104] P. W. Atkins and R. S. Friedman. *Molecular Quantum Mechanics*. OUP Oxford, 2011.

[105] Michael Strickland and David Yager-Elorriaga. A parallel algorithm for solving the 3d schrodinger equation. *Journal of Computational Physics*, 229(17):6015 – 6026, 2010.

[106] P.R. Berman and V.S. Malinovsky. *Principles of Laser Spectroscopy and Quantum Optics*. Princeton University Press, 2010.

[107] N.J. Stone. Table of nuclear magnetic dipole and electric quadrupole moments. *Atomic Data and Nuclear Data Tables*, 90(1):75 – 176, 2005.

[108] M. Yu. Petrov, I. V. Ignatiev, S. V. Poltavtsev, A. Greilich, A. Bauschulte, D. R. Yakovlev, and M. Bayer. Effect of thermal annealing on the hyperfine interaction in inas/gaas quantum dots. *Phys. Rev. B*, 78:045315, Jul 2008.